

Large scale structures around medium mass galaxy clusters at intermediate redshift

THÈSE N° 6649 (2015)

PRÉSENTÉE LE 10 JUILLET 2015
À LA FACULTÉ DES SCIENCES DE BASE
LABORATOIRE D'ASTROPHYSIQUE
PROGRAMME DOCTORAL EN PHYSIQUE

ÉCOLE POLYTECHNIQUE FÉDÉRALE DE LAUSANNE

POUR L'OBTENTION DU GRADE DE DOCTEUR ÈS SCIENCES

PAR

François Henri Ambroise RÉRAT

acceptée sur proposition du jury:

Prof. M. Q. Tran, président du jury
Prof. G. Meylan, Dr P. Jablonka, directeurs de thèse
Prof. D. Pfenniger, rapporteur
Prof. A. Aragon-Salamanca, rapporteur
Prof. O. Schneider, rapporteur



ÉCOLE POLYTECHNIQUE
FÉDÉRALE DE LAUSANNE

Suisse
2015

Abstract

Theory predicts that galaxies are not randomly distributed in the Universe. They form a complex network of filamentary structures, the Cosmic Web, divided in clusters, groups, filaments and walls. This picture has been confirmed by the large galaxy redshift surveys. Galaxy properties like morphology and star formation rates are strongly influenced by their environment. The most radical transformations are observed in galaxy clusters, located at the intersection of filaments. Nevertheless, the location where the environment starts to play a role and the main physical phenomenon responsible for these changes are still unknown. The aim of this thesis is to determine where and how galaxies are affected by the environment, at local and global scales.

We gathered high quality photometry in the 5 optical bands u , g , r , i and z with MegaCam on the Canada-France-Hawaii Telescope for 3 medium mass galaxy clusters at intermediate redshift, with a spatial extent on the sky plane reaching 8 to 13 times the cluster virial radii. These clusters were selected to represent as much as possible progenitors of clusters in the local Universe. The core of these clusters have rich ancillary data from the ESO Distant Cluster Survey. The redshift and mass ranges of these clusters, combined to the wide field of the observations make this study unique.

We computed photometric redshifts to map the galaxy distribution around the clusters. We were able to identify overdense regions forming groups and filaments, unveiling for the first time the large scale structures in such details for this type of clusters. We studied the fraction of galaxies in the red sequence in different environments, namely in the field, filaments and groups. We find that significant quenching processes are already at work in filaments, even at large cluster-centric distances. We also show that the local neighborhood of galaxies has a stronger impact on galaxy colors than the global environment.

An optical spectroscopic follow-up with the VISIBLE MultiObject Spectrograph on the Very Large Telescope confirms our photometric results. In particular, the fraction of galaxies with detected [OII] emission line is smaller with increasing density. We also find that the star formation rate, determined from [OII], is in average weaker in groups and clusters than in lower density environments.

This thesis opens new perspectives to study the way galaxies populate the Cosmic Web. Combined to weak-lensing analysis and cosmological simulations, it will allow a deeper understanding of the structure formation and their baryonic content. It is a first step before extending the results to much larger samples, with the help of the upcoming all-sky cosmological surveys such as Euclid or the Square Kilometer Array.

Key words: galaxy evolution, galaxy clusters, large scale structures, intermediate redshift, environment, photometric redshifts

Résumé

La théorie prédit que les galaxies ne sont pas distribuées aléatoirement dans l'Univers. Elles forment un réseau complexe de structures filamentaires, la Toile Cosmique, divisée en amas, groupes, filaments et murs. Cette idée est confirmée par les grandes campagnes d'observation du décalage vers le rouge des galaxies. Les propriétés des galaxies telles que la morphologie et le taux de formation d'étoiles sont fortement influencées par leur environnement. Les transformations les plus radicales sont observées dans les amas de galaxies, situés à l'intersection des filaments. Néanmoins, le lieu où l'environnement commence à jouer un rôle et le phénomène physique principale responsable de ces changements demeurent inconnus. Le but de cette thèse est de déterminer où et comment les galaxies sont affectées par l'environnement, à des échelles globales et locales.

Nous avons collecté de la photométrie de haute qualité dans les 5 bandes optiques u , g , r , i et z avec MegaCam sur le Télescope Canada-France-Hawaii pour 3 amas de galaxies de masse moyenne à décalage vers le rouge intermédiaire, avec une extension spatiale sur le plan du ciel qui atteint 8 à 13 fois le rayon du viriel des amas. Ces amas ont été sélectionnés pour représenter autant que possible des progéniteurs des amas de l'Univers local. Le coeur de ces amas contient de riches données provenant de l'ESO Distant Cluster Survey. Les intervalles de décalage vers le rouge et de masse de ces amas, combinés au grand champ des observations rendent cette étude unique.

Nous avons calculé des décalages vers le rouge photométriques pour cartographier la distribution des galaxies autour des amas. Nous avons pu identifier des régions de surdensité qui forment des groupes et des filaments, dévoilant pour la première fois les structures à grande échelle de façon si détaillée pour ce type d'amas. Nous avons étudié la fraction de galaxies dans la séquence rouge dans différents environnements : le champ, les filaments et les groupes. Nous trouvons que des processus significatifs d'extinction de la formation d'étoile sont déjà en action dans les filaments, même loin des amas. Nous montrons également que le voisinage proche des galaxies a un impact plus important sur la couleur des galaxies que leur environnement global.

Un suivi spectroscopique dans l'optique avec le Visible MultiObject Spectrograph sur le Very Large Telescope confirme nos résultats photométriques. En particulier, la fraction de galaxies dont la raie d'émission [OII] est détectée est plus basse quand la densité augmente. Nous trouvons également que le taux de formation d'étoiles, déterminé à partir de [OII], est en moyenne plus faible dans les groupes et les amas que dans des environnements de densité moins élevée.

Cette thèse ouvre de nouvelles perspectives pour étudier la façon dont les galaxies peuplent la Toile Cosmique. Combiné à des analyses de lentilles gravitationnelles faibles et de simulations cosmologiques, cela permettra une compréhension plus profonde de la formation des structures et de leur contenu baryonique. Il s'agit d'un premier pas avant d'étendre les résultats à des échantillons bien plus grands, grâce aux futures campagnes d'observations cosmologiques couvrant tout le ciel, telles que Euclid ou le Square Kilometer Array.

Mots clefs : évolution des galaxies, amas de galaxies, structures à grande échelle, redshift intermédiaire, environnement, décalage vers le rouge photométrique

Contents

Abstract (English/Français)	i
List of figures	vii
List of tables	xv
1 Introduction	1
1.1 Structure formation	1
1.2 Galaxy interactions with the environment	2
1.3 The era and location of galaxy quenching	2
1.4 Limitations of previous works	7
1.5 A decisive cluster sample	8
1.6 Objectives of this thesis	10
2 Observations	11
2.1 The cluster sample	11
2.2 Observational strategy	12
2.3 Instrumental setup	13
2.4 Exposure times	14
2.5 Completeness of the program	17
3 Analysis methods	19
3.1 Image characterization	19
3.1.1 Reduction	19
3.1.2 Internal astrometry	22
3.1.3 Seeing and distortions	22
3.1.4 Noise estimation	24
3.1.5 Extinction correction	29
3.1.6 Completeness	30
3.2 Photometric redshifts	32
3.2.1 Code	32
3.2.2 Calibration spectroscopic sample	35
3.2.3 Optimized photometry	35
3.2.4 Final <i>photo-z</i> sample	41

Contents

3.2.5	<i>Photo-z</i> selected large scale structure members	45
3.3	Stellar masses	49
3.3.1	Stellar mass accuracy	49
3.3.2	Stellar mass completeness	51
3.4	Environment measurement	53
4	Results	57
4.1	Large scale structures detection	57
4.2	Red sequence	62
4.3	Influence of the environment	63
4.3.1	Red sequence galaxies and their environment	63
4.3.2	The stellar mass contribution	63
4.3.3	The dominance of small scales	68
4.4	Discussion	71
5	Spectroscopy	73
5.1	Observational strategy	73
5.1.1	Choice of the instrument	73
5.1.2	Field selection	74
5.1.3	Observations	74
5.1.4	Target selection and mask design	76
5.2	Reduction	76
5.3	Extraction of physical measurements	77
5.3.1	Redshifts	77
5.3.2	Star formation rate	77
5.3.3	Equivalent width measurement	79
5.4	Efficiency of the <i>photo-z</i> selection	80
5.5	Results	83
5.5.1	Confirmation of the <i>photo-z</i> selected large scale structures	83
5.5.2	Fraction of [OII] detected galaxies	85
5.5.3	Star formation rates in the large scale structures	87
5.6	Summary and discussion	90
6	Conclusions	93
6.1	Future work	95
6.2	Outlook	96
	Bibliography	106
	Acronyms	107
	Curriculum Vitae	

List of Figures

1.1	The mass density field in the Millennium-XXL dark matter simulation, focusing on the most massive halo present in the simulation at redshift $z=0$. Each inset zooms by a factor of 8 from the previous one; the side-length varies from 4.1 Gpc down to 8.1 Mpc. All these images are projections of a thin slice through the simulation of thickness 8 Mpc. Credit: Millennium-XXL Project.	3
1.2	Distribution of galaxies as a function of redshift and right ascension. Earth is at the center, and each point represents a galaxy. The region between the wedges was not mapped by the SDSS because dust in our own Galaxy obscures the view of the distant universe in these directions. Both slices contain all galaxies within -1.25 and 1.25 degrees declination. Credit: M. Blanton and the Sloan Digital Sky Survey.	4
1.3	Illustration of the ram pressure stripping. This spiral galaxy is falling on a galaxy cluster, located in the top left direction outside the field of view of the image. The blue tails are viewed in the X-ray, they are made of hot gas heated and removed from the galaxy by its encounter with the hot gas trapped in the cluster center. Credit: NASA, ESA, CXC.	5
1.4	These two spiral galaxies, called "the Mice", are merging together. We can see their morphology is highly disturbed, the presence of the long tail at the right is particularly striking. Credit: ACS Science & Engineering Team, NASA.	6
1.5	Cluster velocity dispersions ν_{cl} as a function of lookback time (adapted from Milvang-Jensen et al. 2008). The histogram in gray on the left hand side of the plot shows the distribution at $z<0.1$ from the SDSS (von der Linden et al. 2007) and the dashed lines are the evolutionary tracks of the clusters (i.e. how the cluster mass evolve with time by accretion of smaller systems) from Poggianti et al. (2006). Triangles: EDisCS (Halliday et al. 2004; Milvang-Jensen et al. 2008); empty pentagons: MORPHS (Girardi and Mezzetti 2001); filled pentagons: CLASH (Postman et al. 2012); grey: independent programs on individual clusters (Kodama et al. 2001; Ebeling et al. 2007; Moran et al. 2007; Koyama et al. 2008; Patel et al. 2009; Tanaka et al. 2009; Lubin et al. 2009)). We see the EDisCS clusters are likely progenitors of the typical low- z clusters, contrarily to the majority of the other cluster survey. Among the 5 clusters initially requested for this thesis, 3 of them have been observed (blue triangles; see Section 2.5).	9

List of Figures

2.1	Filter curves of MegaCam. They are normalized to 1 at the peak of the curve. . .	14
2.2	The dome hosting the CFHT, atop Mauna Kea in Hawaii.	15
2.3	The Canada-France-Hawaii Telescope, inside the dome.	15
2.4	The 40 CCDs mosaics at the heart of MegaCam. The size of the square area is 25x25 cm. The two large gaps between the the 1st and 2nd row of CCDs, and the 3rd and 4th rows are well visible. A 2 cent euro coin is shown for scale.	16
3.1	Composite image of CL1301.7-1139, with u , g , r associated to blue, green and red pixel color, respectively. The red square is the FORS2 FoV. The green circles are the R_{200} of the clusters (small one: CL1301.7-1139a, large one: CL1301.7-1139). The mosaics of MegaCam CCDs (Fig. 2.4) is visible: there is no data in the two large horizontal gaps, while the smaller ones appear less dark due to the higher noise in these regions. Bright stars creates circular artifacts due to internal reflections in the telescope, as well as long vertical "spikes" coming from saturation effects. The original image is a square of approximately 20k x 20k pixels. Here we decreased the quality of the image to 2k x 2k pixels.	20
3.2	Similar to Fig. 3.1, for the CL1411.1-1148 field instead of CL1301.7-1139.	21
3.3	Normalized distribution of the difference in pixels between the coordinates of the sources detected in i -band and in the other bands (e.g., x_g is the x pixel coordinate in the g -band).	22
3.4	Magnitudes (in a 1" radius aperture) versus FWHM for each $ugriz$ band for CL1301.7-1139 (top) and CL1411.1-1148 (bottom). In cyan: objects considered as unresolved (see Section 3.1.3), in black: all the other objects in the catalog with $FWHM < 1.5''$ and $10 < mag < 22$. The knee at the bright end visible in g , i , z are due to saturation. The black vertical line is the median FWHM of the cyan objects, while the dashed line shows the FWHM cuts. To avoid overloading the figure, 70 % of the sources have been randomly removed.	24
3.5	Similar to Fig. 3.4. Magnitudes (in a 1" radius aperture) versus ellipticity for each $ugriz$ band for CL1301.7-1139 (top) and CL1411.1-1148 (bottom). In cyan: objects considered as unresolved (see Section 3.1.3), in black: all the other objects in the catalog with $FWHM < 1.5''$ and $10 < mag < 22$. The dashed lines show the ellipticity cuts. To avoid overloading the figure, 70 % of the sources have been randomly removed.	25
3.6	FWHM maps for CL1301.7-1139 (left column) and CL1411.1-1148 (right column), constructed by computing the median FWHM of the 10 nearest unresolved objects (black dots, see Section 3.1.3) from each point of a 30x30 grid. The color scale is the FWHM in arcsec (each band per row). α is the right ascension and δ the declination.	26

3.7	Histograms of empty aperture flux for the background estimation. Each columns corresponds to a field and each row to a band. The zeropoint of the fluxes is 30 for AB magnitudes. The color of each curve corresponds to a different aperture radius r_{aper} (in pixels). Dashed lines are the Gaussian fits. For the largest apertures, there is a tail at bright end. This is a contamination due to nearby sources, however the influence on the fitted Gaussian is weak.	28
3.8	Flux error as a function of linear size s . The units of the flux error are the same as the flux units in Fig. 3.7, i.e. they correspond to a zeropoint of 30 for AB magnitudes. The dots correspond to the width of the Gaussians in Fig. 3.7 and the lines are the fits from Eq. 3.1.	29
3.9	Extinction corrections maps for CL1301.7-1139 (left column) and CL1411.1-1148 (right column). Each row corresponds to a band. The color code is A_λ , in magnitude units.	31
3.10	Number counts for each band and field, keeping only sources with $\text{SNR} > 5$. The dotted line is the power law fit and the dashed line is the 90% completeness limit m_{90}	32
3.11	EAZY prior $P(z R)$ for magnitudes $16 < R < 24$ (the typical magnitude range of our data, see e.g. Fig. 3.10). They are normalized to 1 at the peak of the curve. .	34
3.12	Template library. The fluxes are normalized to 1 at 4000 \AA . To avoid overloading the figure, only one third of the templates are shown (the removed templates would be in between each curve).	36
3.13	Magnitudes (1" radius aperture) against FWHM for each seeing-matched images for CL1301.7-1139 (top) and CL1411.1-1148 (bottom). In cyan: objects considered as unresolved, in black: all the other objects in the catalog with $\text{FWHM} < 1.5''$ and $10 < \text{mag} < 22$. The knee at the bright end visible in g , i and z are due to saturation. The black vertical line is the median FWHM of the cyan objects. Similar to Fig. 3.4. To avoid overloading the figure, 70 % of the sources have been randomly removed.	37
3.14	FWHM maps for the convolved images of CL1301.7-1139 (left column) and CL1411.1-1148 (right column). Each row corresponds to a band. The black dots are the unresolved objects. Similar to Fig. 3.6, but with the convolved images instead of the original ones.	38
3.15	Photometric against spectroscopic redshifts for CL1301.7-1139 (left) and CL1411.1-1148 (right), before (top) and after (bottom) the zeropoint fitting. Spectroscopic redshifts come from FORS2 and LDP. The solid line shows the 1:1 relation, while the dashed lines correspond to $\pm(1 + z_{\text{spec}}) \cdot \sigma_{\text{NMAD}}$	40

List of Figures

- 3.16 This figure show the star/galaxy separation. It is based on a FWHM limit in the image with the best seeing. This limit (solid vertical line) is 0.75" in r -band for CL1301.7-1139, 0.65" in i for CL1411.1-1148. cyan: sources with FWHM below the FWHM cut , considered as stars; black: sources above the FWHM cut. The horizontal dashed lines show the magnitude limit m_{lim} . To avoid overloading the figure, we removed the sources with $\text{SNR} < 5$ and saturated objects with $z < 18$. Furthermore, 95 % of the objects have been randomly removed (it makes the sampling in the u -band a little too low, but it does not harm the purpose of the figure). 42
- 3.17 This figures illustrates how we choose the cut in $odds$. Fraction of outliers (top), σ_{NMAD} (middle), number of galaxies with spectroscopic redshift (bottom) as a function of $odds$ (in bins of width 0.1). The shaded area represents the area below the cut in $odds$ at 0.8. The black (cyan) line corresponds to the CL1411.1-1148 (CL1301.7-1139) field. 43
- 3.18 This figures shows how we removed saturated sources. Each column corresponds to a band and the rows to each field. The magnitude cut is shown by the dashed line. Cyan dots are objects with magnitude above the cut, while black dots are below it. In each panel, the knee is where the saturation occurs. To avoid overloading the figure, 70 % of the sources have been randomly removed. . . . 44
- 3.19 Fraction of outliers (left), σ_{NMAD} (middle), number of galaxies with spectroscopic redshift (right) as a function of i -band magnitude in a 1" radius aperture (in bins of width 0.5). The sample contains only unsaturated ($i > 18$), resolved galaxy, with $odds > 0.8$ 45
- 3.20 $photo$ - z versus i -band magnitude. Black: all the galaxies with $photo$ - z and satisfying the previous cuts ($i > 18$, $odds > 0.8$, FWHM cut), cyan: galaxies with spectroscopic redshifts, red: outliers. 46
- 3.21 z_{phot} against z_{spec} for both fields. Black: galaxies satisfying all the cuts of the final $photo$ - z sample, red: galaxies outside the cuts. The solid line shows the 1:1 relation, while the dashed lines correspond to $\pm(1 + z_{\text{spec}}) \cdot \sigma_{\text{NMAD}}$ 46
- 3.22 Number counts for each band and field, for the final $photo$ - z sample (to be compared with Fig. 3.10). 47
- 3.23 This figure shows the $photo$ - z selection of the cluster members. The shaded area are δz , the z_{phot} intervals used for the selection. Red: cluster members in δz , $N_{\text{cl}}^{\delta z}$, blue: field galaxies within δz , $N_{\text{field}}^{\delta z}$, green: cluster members outside of δz , $N_{\text{cl}}^{\text{not } \delta z}$, black: field galaxies outside δz . The solid line shows the 1:1 relation, while the dashed lines correspond to $\pm(1 + z_{\text{spec}}) \cdot \sigma_{\text{NMAD}}$ 48
- 3.24 Error in stellar mass as a function of stellar mass. The dashed line is the median of the error. 50
- 3.25 Stellar mass difference (in log) as a function of the difference in redshift. M_{*}^{phot} (M_{*}^{spec}) is the stellar mass, expressed in solar masses, when z_{phot} (z_{spec}) is used for the redshift estimation. 50

3.26	Illustration of the procedure to compute the stellar mass completeness. Black: distribution of the stellar masses at the cluster redshifts, red: galaxies with $22 < i < 23$, blue: scaled stellar masses. The dashed line represents the 95 % completeness stellar mass limit.	52
3.27	Stellar mass against i -band magnitude for the <i>photo-z</i> selected cluster members. The shaded area is the magnitude interval chosen for the scaling, the dashed vertical line is the magnitude completeness limit $m_{\text{lim}} = 22.4$ and the dashed horizontal line is the stellar mass completeness.	52
3.28	Distribution of the distance to N^{th} nearest neighbor, r_N , computed at each point of a 500x500 grid, for different values of N . The distribution are truncated at 3 MAD around the median. The black dashed lines are Gaussian fits, whose mean and width are reported in Fig. 3.29 as a function of N	54
3.29	Mean of the r_N distributions of Fig. 3.28, as a function of the the number of neighbors N . The shaded areas correspond to 1 and 3 σ of the Gaussian fit. . .	54
3.30	Distribution of the density Σ_N as a function of the number nearest neighbor N . The distribution are truncated at 3 median absolute deviation (MAD) around the median. The black dashed lines are Gaussian fits, whose mean and width are reported in Fig. 3.31 as a function of N . Similar to Fig. 3.28, with Σ_N instead of r_N	55
3.31	Mean of the Σ_N distributions of Fig. 3.30, as a function of the number of neighbors N . The shaded areas correspond to 1 and 3 σ of the Gaussian fit. Similar to Fig. 3.29, with Σ_N instead of r_N	55
4.1	Density maps of the <i>photo-z</i> selected large scale structures members around CL1301.7-1139a. The light black dots are the galaxies, while the color code represents $\log \Sigma_N$. The top row is for $N=10$ and the bottom one for $N=30$. The grey horizontal bands show the MegaCam large CCD gaps. In this map, the density is computed also near the gaps and the edge of the FoV (where it is underestimated), to give the reader a better insight of the global density field. The white regions are where $\log \Sigma_N < 0.2$. The thin black contours separate the density field between the field, filaments and groups/clusters. The blue solid circle is the cluster virial radius (R_{200}) and the dashed one is $5R_{200}$. The North is at the top of the figure and the East at the left.	58
4.2	Same as Fig. 4.1, but with CL1301.7-1139 instead of CL1301.7-1139a.	59
4.3	Same as Fig. 4.1, but with CL1411.1-1148 instead of CL1301.7-1139a.	60
4.4	Local density as a function of the cluster-centric distance, for each one of the LSS samples. The dotted lines are the thresholds separating the density field between the field, filaments and groups/clusters.	61
4.5	Color-magnitude diagram $g - i$ versus i (1" radius apertures). The solid black line is a fit to the cluster red sequence, with the 3σ scatter delimited by the dashed lines. The dotted lines show the magnitude limits in g and i . The cyan dots are the spectroscopic members (from LDP and FORS2).	62

List of Figures

4.6	Fraction of galaxies on the red sequence as a function of local density, for galaxies close to the cluster redshift. The bins are defined by steps of 0.1 dex and have a width of 0.4 dex (thus they partially overlap). The dotted lines are the thresholds separating the density field between the field, filaments and groups/clusters.	63
4.7	$g - i$ colors as a function of stellar mass, for each LSS sample. The vertical lines are the mass completeness limits. Red dots are the red sequence members.	64
4.8	$g - i$ colors as a function of the local density. The panels correspond to different clusters (columns) and stellar mass intervals (rows). The dotted lines are the thresholds separating the density field between the field, filaments and groups/clusters. M_* is expressed in solar mass units. Red dots are the red sequence members.	65
4.9	Fraction of galaxies in the red sequence as a function of density, for different stellar mass intervals. The binning in density is adaptive: the lower bound of each bin increases by steps of 0.1 and the upper bound is chosen such as each bin contains $1/5^{th}$ of the objects (in the given stellar mass interval). With this binning, the error bars are constant (since they depend only on the number of objects in the bin). The dotted lines are the thresholds separating the density field between the field, filaments and groups/clusters.	66
4.10	Fraction of galaxies in the red sequence as a function of stellar mass, for different local density intervals (corresponding to the field, filaments and groups/clusters). The binning in stellar mass is adaptive: the lower bound of each bin increases by steps of 0.1 and the upper bound is chosen such as each bin contains $1/5^{th}$ of the objects (in the given density interval).	66
4.11	$g - i$ colors as a function of stellar mass. The panels correspond to different clusters (columns) and local density intervals (rows). The density intervals select different environments, namely the field (bottom row), filaments (middle row) and groups/clusters (top row). M_* is expressed in solar mass units.	67
4.12	Local versus global density, for each galaxy close to the cluster redshift. The dotted lines show the density thresholds used in Fig. 4.1, 4.2, 4.3 and 4.9. The dotted lines are the thresholds separating the global and local density fields between the field, filaments and groups/clusters.	68
4.13	$g - i$ colors as a function of the local density. The panels correspond to different clusters (columns) and global density intervals (rows). The dotted lines are the thresholds separating the local density field between the field, filaments and groups/clusters.	69
4.14	Fraction of galaxies in the red sequence as a function of density, for different density intervals. The binning in density is adaptive: the lower bound of each bin increases by steps of 0.1 and the upper bound is chosen such as each bin contains $1/5^{th}$ of the objects (in the given stellar mass interval). The dotted lines are the thresholds separating the global density field between the field, filaments and groups/clusters.	70

4.15	Fraction of red sequence galaxies as a function of the global environment. In red (blue): galaxies whose local density is higher (lower) than the global one.	70
5.1	Density map used to choose the pointings (realized in the same way as Fig. 4.3). The light black dots are the <i>photo-z</i> selected large scale structures members of CL1411.1-1148, while the color code represents $\log \Sigma_{10}$. The 6 x 4 rectangles correspond to each chip of VIMOS for the 6 telescope pointings. The dashed rectangles are the observations which where not completed.	75
5.2	Galaxy templates used to extract redshifts with RVSAO. Dashed (dotted) lines are emission (absorption) lines. For clarity, the spiral template is offset by 1 on the y-axis.	77
5.3	Example of VIMOS spectra of galaxies with emission lines (top), without EM lines (middle) or inconclusive. The spectra are deredshifted. The red segments of the spectra highlight the O ₂ atmospheric absorption lines. For clarity, the spectra are offset from each other by 1 on the y-axis.	78
5.4	Errors on the VIMOS redshifts estimation, estimated from the width of highest peak in the cross-correlation function between the Fourier transforms of the template galaxy and the spectrum.	78
5.5	Photometric versus spectroscopic redshift. Left: last version of the <i>photo-z</i> , the shaded area is the <i>photo-z</i> interval used for the selection of the LSS. Right: <i>photo-z</i> at the time of the target selection, the shaded area is <i>photo-z</i> interval used for the target selection. Blue: galaxies with an LDP redshift at $z_{cl} \pm 0.02$. Red: galaxies which are by chance in a slit (they were not in the target selection). The solid line shows the 1:1 relation, while the dashed lines correspond to $\pm(1 + z_{spec}) \cdot \sigma_{NMAD}$. 80	80
5.6	Photometric versus spectroscopic redshift, for FORS2, LDP and VIMOS samples. The solid line shows the 1:1 relation, while the dashed lines correspond to $\pm(1 + z_{spec}) \cdot \sigma_{NMAD}$	81
5.7	Spectroscopic redshifts distributions. Top: in black, all the redshifts from any instrument for $0.3 < z < 0.7$, FORS2 redshifts in red, LDP in blue, VIMOS in green. Middle: zoom on the $0.48 < z < 0.56$ region, with the black bar showing the CL1411.1-1148 cluster membership area ($0.5195 \pm 4\nu_{cl}$). Bottom: zoom on the $0.45 < z < 0.53$ region, with the black bar showing the CL1411.1-1148a membership area (0.4875 ± 0.015). The dashed lines are the cluster redshifts: 0.5185 for CL1411.1-1148 and 0.4875 for CL1411.1-1148a (see text).	82

- 5.8 Similar to Fig. 5.1 (and the top panel of Fig. 4.3). The color codes the density $\log \Sigma_{10}$ in Mpc^{-2} . The parent distribution (black dots) is the *photo-z* selected LSS members, without the spectroscopic non-members. The red (blue) symbols are the CL1411.1-1148 (CL1411.1-1148a) members (defined in Fig. 5.7). Stars are from LDP redshifts, (large) dots from VIMOS and diamonds from FORS2. The black line and circles highlight regions of interest (see Section 5.5.1). The blue circle is the cluster R_{200} and the dashed one is $5R_{200}$. The 5×4 light dark rectangles correspond to each chip of VIMOS for the 5 telescope pointings. The thin black contours separate the density field between the field, filaments and groups/clusters. The thick black line and circles highlight regions of interest (see Section 5.5.1). 84
- 5.9 $g-i$ color as a function of the [OII] equivalent width, for the CL1411.1-1148 members with FORS2 or VIMOS spectroscopy. Red sequence members are in red. The dashed line is at $W_{[\text{OII}]} = -5 \text{ \AA}$, above which [OII] is considered undetected. . . 85
- 5.10 Fraction of [OII] detected galaxies as a function of the local density Σ_{10} . The dotted vertical lines are the bins edges ($\log \Sigma_{10} = 0.95, 1.4 [\text{Mpc}^{-2}]$), separating the density field between field galaxies, filaments and groups/clusters. 86
- 5.11 Fraction of [OII] detected galaxies as a function of the global density Σ_{30} . The dotted vertical lines are the bins edges ($\log \Sigma_{30} = 0.8, 1.1 [\text{Mpc}^{-2}]$), separating the density field between field galaxies, filaments and groups/clusters. 88
- 5.12 SFR a function of the local density. Red dots are the red sequence members, black dots are the red sequence non-members. The solid line is the median SFR of the star-forming galaxies ($W_{[\text{OII}]} < -5 \text{ \AA}$) and the grey envelopes encompass the 25^{th} and 75^{th} percentiles. The dotted vertical lines are the bins edges ($\log \Sigma_{10} = 0.95, 1.4 [\text{Mpc}^{-2}]$), separating the density field between field galaxies, filaments and groups/clusters. 89
- 5.13 Position of the FORS2 and VIMOS cluster members, with a color code for their SFR. The light black dots are the *photo-z* selected large scale structures members. The thin black lines are the density thresholds ($\log \Sigma_{10} = 0.95, 1.4 [\text{Mpc}^{-2}]$) separating the density field between field galaxies, filaments and groups/clusters. The thick black line and circles highlight regions of interest (see Section 5.5.1). The blue circles show 1 and 5 R_{200} , the black circles are the groups identified in Fig. 5.8 and the grey bands are the MegaCam large CCD gaps. 90

List of Tables

2.1	Main properties of the clusters. z_{cl} is the cluster redshift, v_{cl} the velocity dispersion, R_{200} the virial radius and field of view (FoV) / R_{200} the number of R_{200} included in the MegaCam FoV.	12
2.2	Journal of the observations. The total exposure time is provided as well as the completion rate. The magnitude limits m_{lim} is defined as the magnitude integrated in 1" radius apertures for a signal-to-noise of 10 (see Section 3.1.4) and m_{90} is the completeness limit measured in 1" radius apertures (see Section 3.1.6). 17	
3.1	Minimum, median and maximum extinction correction (A_{λ}) for each band and field.	30
3.2	Different statistics to evaluate the quality of the cluster member selection. . . .	48

1 Introduction

Astronomers can be considered as historians of the Universe. The ultimate goal is to understand its full evolution, starting from about 380000 years after the Big-Bang until what we see today. The scales concerned are extremely broad, they range from the size of dust up to cosmological distances, including planets, stars and galaxies.

In this introduction, we will describe in details the topic: the global theoretical context, the previous studies used as benchmarks and the unexplored aspects we focus on.

1.1 Structure formation

The modern point of view on galaxy formation relies on the lambda cold dark matter cosmological model. In this framework, the Universe is made of three major components. Dark energy, responsible for the accelerated expansion of the Universe, is the dominant one. Dark matter, which is only sensitive to gravity, follows. The visible matter, the only one detected directly through its electromagnetic emission, comes last. This model is the one matching the largest number of observations.

From this theory, a scenario explaining the evolution of the Universe and in particular the formation of structures occurs has emerged. Shortly after the Big Bang, while the Universe was a hot and dense plasma, its size expanded dramatically during a phase called the inflation. The initial quantum fluctuations were expanded to a cosmological scale and are still visible today as a relic radiation, the Cosmic Microwave Background (CMB). This expansion resulted in a strong cooling of these fluctuations, allowing them to collapse under their own gravity and form the first stars and galaxies. The galaxies further attracted each other to form a complex network of filamentary structures called the Cosmic Web.

This general picture has been confirmed in many ways. Two major successes of this theory are the explanations of the CMB and the large scale structures of the Universe. The latter is shown

in simulations in Fig. 1.1¹, showing successive zoom on the dark-matter mass distribution, and observationally in the local Universe on Fig. 1.2, where the distribution of galaxies as a function of redshift and right ascension is represented. We see qualitatively an excellent agreement between the two distributions, in the sense that the filamentary patterns are well reproduced.

1.2 Galaxy interactions with the environment

The evolution of galaxies is strongly influenced by their surroundings. A denser environment, in terms of number of galaxies and dark matter mass, implies more interactions, hence stronger changes in the galaxy properties. The densest structures in the Cosmic Web (CW), galaxy clusters, are where the strongest environmental effects occur. They are ideal laboratories to study the influence of the environment. One of the first example was highlighted by Dressler (1980), who showed that galaxy clusters contained more elliptical galaxies than in the field.

A significant fraction of the physical phenomena responsible for the changes of galaxy properties with environment have been identified. The most extreme case is the removal of the gas within a galaxy when it encounters the high temperature gas in the core of a cluster (ram pressure stripping; e.g., Gunn and Gott 1972; Vollmer et al. 2006; see Fig. 1.3), but more local effects like mergers (e.g., Renaud et al. 2015; Fig. 1.4) or high velocity encounters (harassment; e.g., Moore et al. 1996) between galaxies may also lead to dramatic changes in galaxy properties.

In the local Universe (redshift $z < 0.1$), relations between galaxy properties and their density have been already well explored, in galaxy clusters but also in the field. The local density of galaxies is correlated with galaxy colors (e.g., Hogg et al. 2004; Kauffmann et al. 2004; Baldry et al. 2006), morphology (Dressler 1980; van der Wel 2008), and star formation rate (Lewis et al. 2002; Gómez et al. 2003; Peng et al. 2010). Red, early-type galaxy (ETG) with a low star formation rate (SFR) tend to reside in denser environments. Galaxies which have ceased forming stars due to the environment are said to be quenched.

1.3 The era and location of galaxy quenching

Studies in the local Universe are useful to observe directly galaxies interacting with the environment, simply because these galaxies are relatively close from us and therefore more easily observed. However they only provide a snapshot of the current state of galaxies. Their history cannot be directly reached. When observing a quiescent galaxy, we do not know how, where and when the star formation ceased. For instance in clusters, we do not know whether the star formation stopped in quiescent galaxies due to the influence of the cluster, or if they were already quenched before reaching the cluster.

Moreover, in the past star formation was much more active than today. The global star

¹ 1 pc = 1 parsec ≈ 3.26 light-years $\approx 3.09 \cdot 10^{16}$ meters. 1 Gpc = 10^9 pc, 1 Mpc = 10^6 pc.

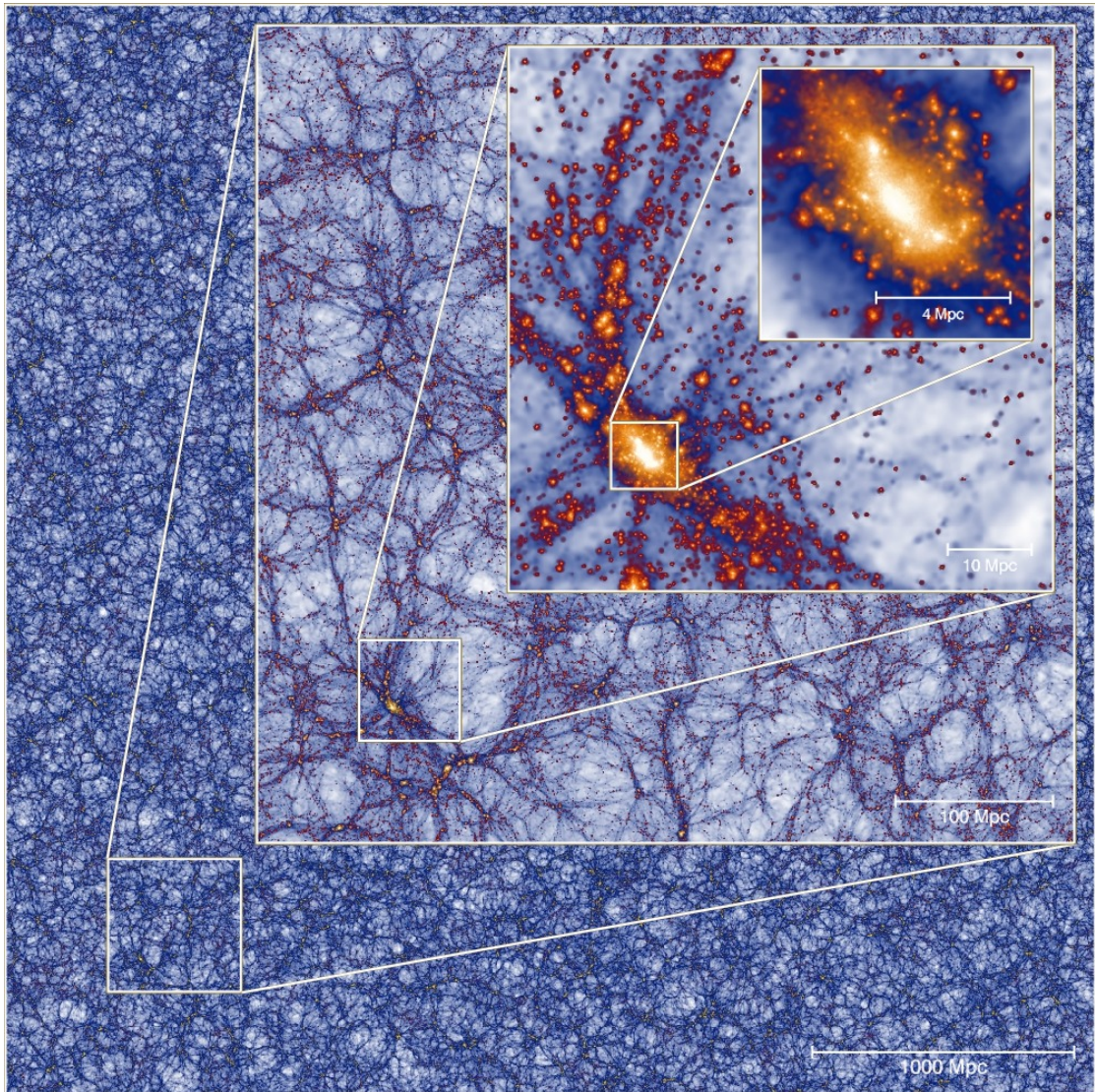


Figure 1.1 – The mass density field in the Millennium-XXL dark matter simulation, focusing on the most massive halo present in the simulation at redshift $z=0$. Each inset zooms by a factor of 8 from the previous one; the side-length varies from 4.1 Gpc down to 8.1 Mpc. All these images are projections of a thin slice through the simulation of thickness 8 Mpc. Credit: Millennium-XXL Project.

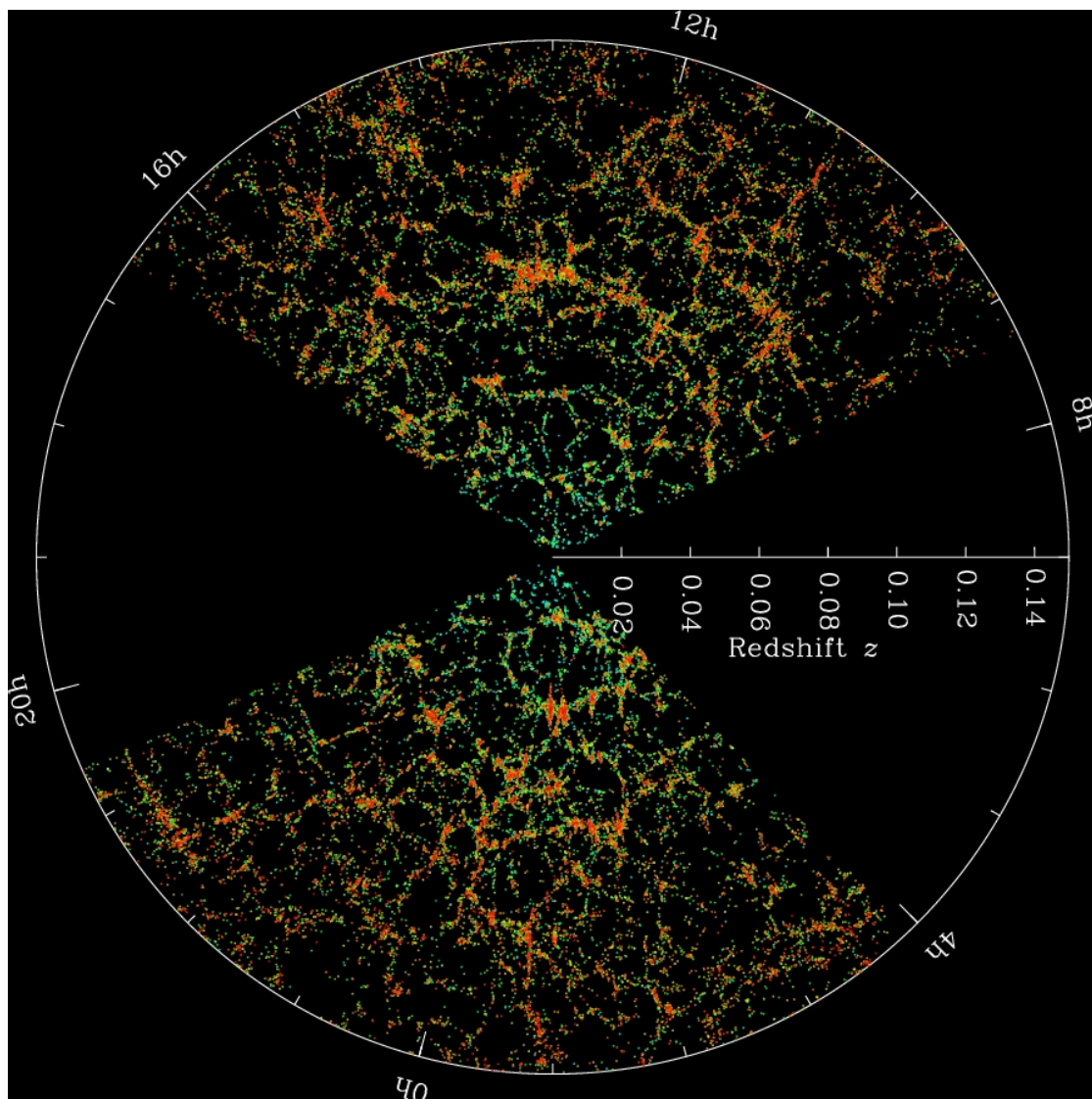


Figure 1.2 – Distribution of galaxies as a function of redshift and right ascension. Earth is at the center, and each point represents a galaxy. The region between the wedges was not mapped by the SDSS because dust in our own Galaxy obscures the view of the distant universe in these directions. Both slices contain all galaxies within -1.25 and 1.25 degrees declination. Credit: M. Blanton and the Sloan Digital Sky Survey.



Figure 1.3 – Illustration of the ram pressure stripping. This spiral galaxy is falling on a galaxy cluster, located in the top left direction outside the field of view of the image. The blue tails are viewed in the X-ray, they are made of hot gas heated and removed from the galaxy by its encounter with the hot gas trapped in the cluster center. Credit: NASA, ESA, CXC.



Figure 1.4 – These two spiral galaxies, called “the Mice”, are merging together. We can see their morphology is highly disturbed, the presence of the long tail at the right is particularly striking. Credit: ACS Science & Engineering Team, NASA.

formation rate of the Universe and the fraction of star forming galaxies increases with redshift up to at least $z=2$ (Santini 2011; Whitaker et al. 2012). At a given mass, the SFR has decreased by a factor of ~ 4 from $z \sim 0.5$ to $z = 0$. A simple evolution where galaxies have an initial gas reservoir which is gradually transformed into stars does not explain this abrupt decrease from $z = 2$ until today. It means that at this epoch, the environment plays a major role in shutting down the SFR. Another point confirming this view comes from the fact that the divergence in the fraction of star forming galaxies between field and cluster galaxy populations is rising with redshift (Finn et al. 2010). Ideally, we would therefore want to observe clusters between $z=0$ and 2. Unfortunately, this is technically very challenging. Only a few dozen galaxy clusters have been spectroscopically confirmed at $z > 1$ (Muzzin et al. 2012; Wagner et al. 2015). They were often observed with a low resolution or with few galaxy members, restricting the analysis of their stellar populations. At these redshifts, the morphology of galaxies is also difficult to obtain (their angular size is small and requires very high resolution), limiting our capacity to identify the quenching processes at play. A significant fraction of the clusters assembly took place since $z \lesssim 1$ (Wechsler et al. 2002; McGee et al. 2009), this is another important argument against a high- z study. For these reasons, the ideal epoch to study the influence of the environment of galaxies is at intermediate redshift ($0.3 \lesssim z \lesssim 0.9$).

As galaxies are accreted on clusters, the number of possible environmental effects increases (e.g., ram pressure stripping is absent in low density regions). Therefore, the properties of galaxies should be correlated to the cluster-centric distance². This has been observed by several studies at different redshifts. More importantly, it was shown that the fraction of SF galaxies is below the field value as far as $5R_{200}$ (Lewis et al. 2002; Chung et al. 2011), where

²The radial distance to the cluster center.

R_{200} is the radius inside which the density is 200 times the critical density of the Universe and approximates well the cluster virial radius. The environment seems influential even far away from the cluster core. Identifying what it is the dominant quenching process and where it occurs requires therefore to observe a wide area around the clusters.

1.4 Limitations of previous works

As they are not focused on clusters, field survey such as SDSS (e.g., Baldry et al. 2006) and zCOSMOS (e.g., Knobel et al. 2012; Kovač et al. 2014) tend to spectroscopically undersample the highest density regions and photometry alone is not sufficient to characterize accurately the clusters candidates. Independent programs on individual clusters (e.g., Kodama et al. 2004; Moran et al. 2007; Patel et al. 2009; Tanaka et al. 2009) are difficult to compare, because of the heterogeneity between the datasets (filters used, redshift range, cosmic variance, depth, completeness, etc.), the different estimation of the galaxy properties (e.g. rest-frame $u - g$ or $g - r$ colors, different assumptions to compute stellar masses, SFR derived from the optical or the infrared, etc.) and the methods used to measure the environments (projected or three-dimensional density, galaxy number counts in fixed or adaptive aperture, local or global scales, etc.). Moreover, most of the intermediate redshift, wide-field cluster surveys are focused on too massive clusters (e.g., MORPHS (Girardi and Mezzetti 2001), MACS, Ebeling et al. 2007; ORELSE, Lubin et al. 2009; ICBS, Oemler et al. 2013; CLASH-VLT, Rosati et al. 2014). They are at the very high end of the cluster mass function in the local Universe and hence are not representative of the typical cluster population (see Fig. 1.5).

Another crucial limitation of previous works is that they analyze the environment in terms of cluster-centric distance or local density, while both quantities should be studied together. Indeed, the clusters do not accrete matter in a spherically symmetric way, they are fed by filaments and groups along privileged directions (Bahé and McCarthy 2015). Radial studies completely miss this unsymmetrical aspect, while the local density fails to reconstruct the global patterns. For instance, at a given local density, it is still unknown if galaxy properties are different within filaments or in the field.

An ideal survey to study the influence of the LSS on galaxy evolution should combine the following characteristics:

1. Probe the intermediate redshift range (or higher), a crucial epoch to study quenching phenomenons.
2. Focus on galaxy clusters, as they form the knots of the cosmic web and are expected to be at the center of complex structures where a wide range of physical processes are at play.
3. Target clusters which are typical progenitors of the low- z clusters (with a velocity dis-

persion³ below 900 km/s), to avoid being biased towards massive, evolved structures in which most of the environmental effects already happened.

4. Extend over a wide field, at least $\sim 5R_{200}$, as environmental effects have been observed even at those large cluster-centric distances.
5. Map the distribution of galaxies with a high spatial sampling, to trace accurately the structures surrounding and feeding the main cluster.
6. Detect galaxies up to relatively low mass (at least below $5 \cdot 10^{10}$ solar masses), as massive galaxies have generally ceased the star formation.

So far none of the existing survey combines all these features.

1.5 A decisive cluster sample

In the local Universe, galaxy groups and clusters have typical velocity dispersions v_{cl} between 300 and 500 km/s (von der Linden et al. 2007). The best clusters to study should be typical progenitors of low- z clusters, to be representative of the general population. Until now, the ESO Distant Cluster Survey (EDisCS, White et al. 2005) is the only cluster focused survey satisfying this condition over a significant sample. We illustrate this aspect on Fig. 1.5 (adapted from Milvang-Jensen et al. 2008), showing the distribution of cluster velocity dispersion v_{cl} against lookback time (the time the light traveled before reaching the observer; $z \sim 0.5$ corresponds to a lookback time of ~ 5 Gyr). The histogram on the left shows the distribution at $z < 0.1$ from the SDSS and the dashed lines are the evolutionary tracks of the clusters (i.e. how the cluster mass evolve with time by accretion of smaller systems). We see that the EDisCS clusters (triangles) are progenitors of the typical low- z clusters, contrary to the majority of the other cluster survey (in green and grey).

EDisCS is an ESO large program targeting 26 galaxy clusters spanning velocity dispersions from $v_{cl} = 166$ to 1080 km/s at intermediate redshift ($z = 0.40 - 0.96$). This sample was selected from 1073 clusters detected by the Las Campanas Distant Cluster Survey (LCDCS; Gonzalez et al. 2001). The LCDCS region is a strip (90 degrees long and 1.5 degrees wide) observed with a very wide filter (~ 4500 to ~ 7700 Å). Clusters are detected by convolving the images with an exponential kernel matched to the expected core size of galaxy clusters at $z \sim 0.8$. The EDisCS program selected the highest surface brightness clusters in the LCDCS.

³The positions of galaxies in galaxy clusters relatively to the cluster center are not fixed. Due to the high mass of the cluster (dominated by its dark matter halo), they move around (and across) the cluster center at typical velocities of a few hundreds kilometers per second. In well formed clusters, the velocity distribution is approximately a Gaussian with a zero average and a width v_{cl} , related to the total mass of the cluster.

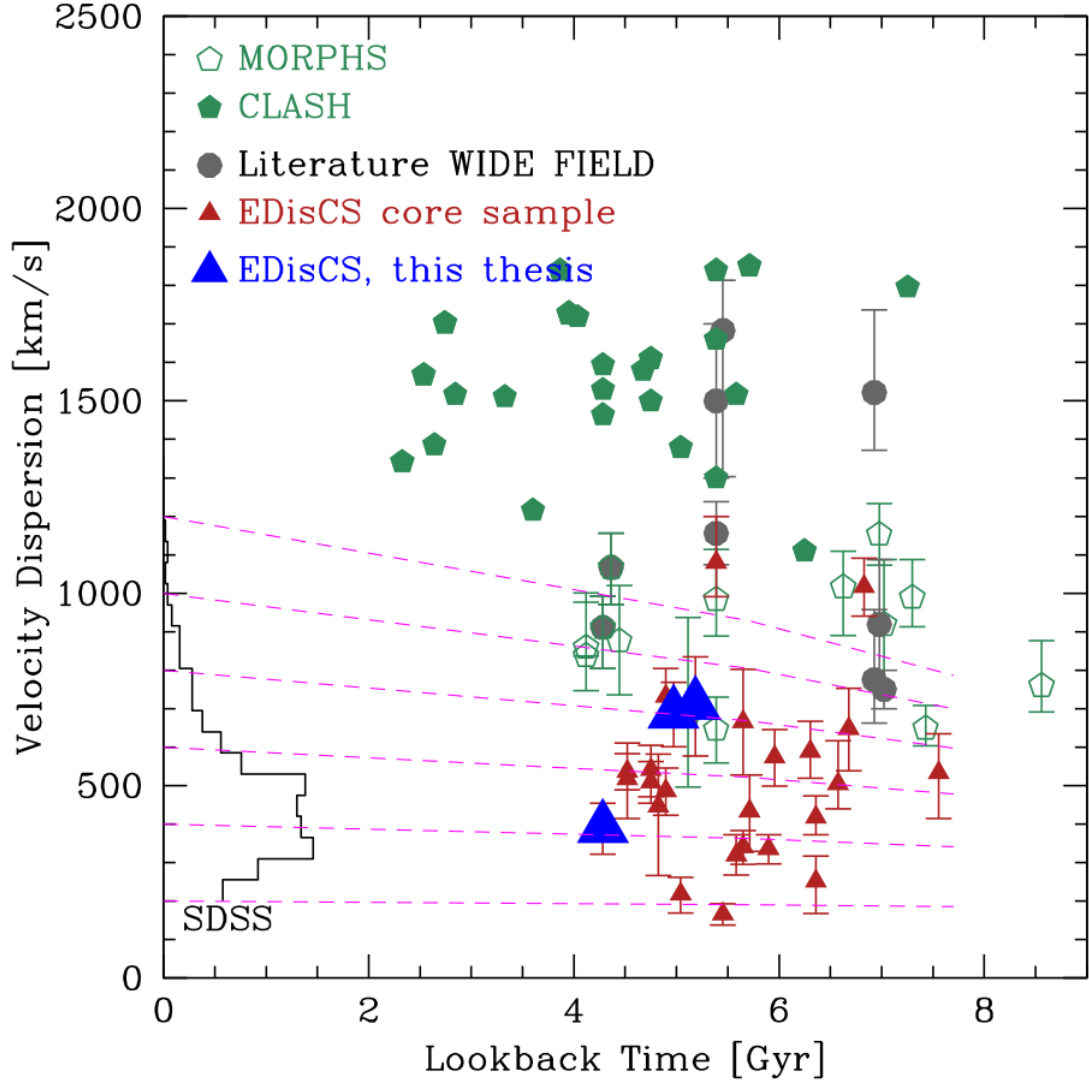


Figure 1.5 – Cluster velocity dispersions v_{cl} as a function of lookback time (adapted from Milvang-Jensen et al. 2008). The histogram in gray on the left hand side of the plot shows the distribution at $z < 0.1$ from the SDSS (von der Linden et al. 2007) and the dashed lines are the evolutionary tracks of the clusters (i.e. how the cluster mass evolve with time by accretion of smaller systems) from Poggianti et al. (2006). Triangles: EDisCS (Halliday et al. 2004; Milvang-Jensen et al. 2008); empty pentagons: MORPHS (Girardi and Mezzetti 2001); filled pentagons: CLASH (Postman et al. 2012); grey: independent programs on individual clusters (Kodama et al. 2001; Ebeling et al. 2007; Moran et al. 2007; Koyama et al. 2008; Patel et al. 2009; Tanaka et al. 2009; Lubin et al. 2009)). We see the EDisCS clusters are likely progenitors of the typical low- z clusters, contrarily to the majority of the other cluster survey. Among the 5 clusters initially requested for this thesis, 3 of them have been observed (blue triangles; see Section 2.5).

1.6 Objectives of this thesis

The goal of my thesis is to use the full spatial distribution of galaxies around clusters to measure where and how the environment triggers modifications of galaxy properties. We want to understand how they depend on the position in the CW, following the changes along the filamentary patterns predicted by the simulations (not only as a function of the cluster-centric distance or local density). We will also study whether galaxies within filaments are different compared to the field and clusters, and if substructures within the filaments are responsible for significant quenching effects before reaching the cluster.

The following procedure was employed to meet these aims:

1. Gather wide-field, high quality and homogeneous u , g , r , i and z optical data around 5 medium mass galaxy clusters at intermediate redshift.
2. Compute photometric redshifts to map the distribution of galaxies.
3. Identify overdense regions of galaxies around the clusters.
4. Compare galaxy colors and stellar masses in the different density ranges.
5. Confirm the photometric results with spectroscopy.
6. Analyze an emission line, as a tracer of the SFR, in the different environments.

This thesis explains how the observations were planned and outstand from previous studies (Chapter 2), the methods used for their reduction and analysis (Chapter 3) and the results obtained (Chapter 4). The spectroscopic follow-up and its implications are presented in Chapter 5. Finally, the conclusions and the future work are summarized in Chapter 6.

2 Observations

This chapter describes the cluster sample, the observational strategy and the completeness of our program.

All the magnitudes quoted in this thesis are in the AB system¹. The cosmological parameters are taken from Planck Collaboration et al. (2013): $H_0=67.3$ km/s/Mpc, $\Omega_m=0.315$, $\Omega_\Lambda=0.685$ and $k=0$.

2.1 The cluster sample

Our cluster sample is drawn from the ESO Distant Cluster Survey (EDisCS, White et al. 2005). The clusters cores are covered with deep photometry (over a $\sim 7 \times 7$ arcmin² field of view): in the *B*, *V*, *R* and *I* optical filters with the FOcal Reducer and low dispersion Spectrograph 2 (FORS2) on the Very Large Telescope (VLT) (White et al. 2005), in the *J* and *K* near-infrared (NIR) filters with the Son OF Infrared Spectrometer And Array Camera (SOFI) on the New Technology Telescope (NTT), in the F814W optical filter with the Advanced Camera for Surveys (ACS) on the Hubble Space Telescope (HST) (Desai et al. 2007). Medium resolution optical spectroscopy was obtained with VLT/FORS2 (Halliday et al. 2004; Milvang-Jensen et al. 2008) and at low resolution with the low dispersion prism (LDP) grism of the Inamori-Magellan Areal Camera & Spectrograph (IMACS) on the Magellan telescope. The richness of the EDisCS dataset for these clusters and their mass and redshift range made them ideal candidates for our campaign.

The studies based on EDisCS (e.g., Desai et al. 2007; Poggianti et al. 2008; Pelló et al. 2009) are focused on the core of the clusters (up to $\sim 2R_{200}$), while our study requires to reach at least $5R_{200}$. A wide-field campaign on all the 26 EDisCS would require a large amount of telescope time. We chose to start with 5 clusters with a relatively low redshift. Their main properties are presented in Table 2.1. The velocity dispersion and redshifts are taken from Milvang-Jensen

¹In the AB magnitude system, a flux (f_ν) of 3631 Jansky (in any filter) corresponds to a magnitude of zero (see Oke 1974). Stated otherwise, in this system the zeropoint is 3631 Jansky ($1 \text{ Jansky} = 1 \text{ Jy} = 10^{-26} \text{ W Hz}^{-1} \text{ m}^{-2}$). For a flux measured in Jansky, the corresponding magnitude is $m = -2.5 \log_{10}(f_\nu/3631)$.

cluster name	z_{cl}	ν_{cl} [km/s]	R_{200} [arcmin]	R_{200} [Mpc]	M_{cl} [$10^{15} M_{\odot}$]	FoV / R_{200}
CL1018.8-1211	0.4734	486^{+59}_{-63}	2.62	0.91	0.149	11.44
CL1054.4-1146	0.6972	589^{+78}_{-70}	2.31	0.96	0.231	12.99
CL1301.7-1139	0.4828	687^{+81}_{-86}	3.65	1.29	0.417	8.23
CL1301.7-1139a	0.3969	391^{+63}_{-69}	2.44	0.76	0.081	12.27
CL1411.1-1148	0.5195	710^{+125}_{-133}	3.55	1.27	0.451	8.46

Table 2.1 – Main properties of the clusters. z_{cl} is the cluster redshift, ν_{cl} the velocity dispersion, R_{200} the virial radius and FoV / R_{200} the number of R_{200} included in the MegaCam FoV.

et al. (2008). R_{200} and the cluster mass M_{cl} are computed as in Finn et al. (2005):

$$R_{200} = 1.73 \frac{\nu_{\text{cl}}}{1000 \text{ km/s}} \frac{1}{\sqrt{1 + \Omega_{\lambda} + \Omega_m(1+z)^3}} h^{-1} \text{Mpc}, \quad (2.1)$$

$$M_{\text{cl}} = 1.2 \cdot 10^{15} \left(\frac{\nu_{\text{cl}}}{1000 \text{ km/s}} \right)^3 \frac{1}{\sqrt{1 + \Omega_{\lambda} + \Omega_m(1+z)^3}} h^{-1} M_{\odot}, \quad (2.2)$$

with the normalized Hubble constant $h = H_0 / (100 \text{ km s}^{-1} \text{ Mpc}^{-1}) = 0.673$ and the solar mass $M_{\odot} = 1.99 \cdot 10^{30} \text{ kg}$.

2.2 Observational strategy

We want to identify the large scale structures (LSS) around the clusters. It requires to know the position of each galaxy in the field and estimate whether they are close enough from the cluster to belong to the same superstructure. The position of a galaxy on the sky is straightforward to obtain from an image. It is simply defined by its right ascension α and declination δ . The distance along the line-of-sight is much less trivial to measure. We need a method that *i*) can be applied to any type of galaxy (not only e.g. AGN), *ii*) does not rely on short-lived or rare events (like supernovae or gamma ray bursts) and *iii*) works at cosmological scales (unlike parallax or Cepheid-based methods). The only two remaining possibilities for our case are photometric and spectroscopic redshifts. As indicated in the name, they both measure redshifts, which can be converted to physical distances under the assumption of a specific cosmological model. Spectroscopic redshifts rely on the detection of known features (like absorption and emission lines) in galaxy spectra (see Section 5.3.1). The principle of photometric redshifts is to observe galaxies in broad band filters and fit the shape of their spectral energy distribution (SED) (see Section 3.2). The choice of photometric versus spectroscopic redshifts is a trade-off between accuracy and statistics. For a fixed amount of telescope time with a wide-field instrument which can operate as a spectrograph or an imager, spectroscopic redshifts are typically two orders of magnitude more accurate than photometric redshifts, but the number of targets observed is usually only a few percent of the objects detected in the images.

Our strategy combines the two approaches. We chose to achieve a first mapping of the LSS using photometric redshifts (*photo-z*; Section 3.2 and 4.1), which were followed by spectroscopy on specific regions determined with the help of the *photo-z* (Chapter 5). Once we have a good enough description of the cluster environment, the second step is to further characterize the galaxy populations composing it, based on properties such as stellar masses (Section 3.3 and 4.3.2), colors (Section 4.2, 4.3) and star formation rates (Section 5.3.2 and 5.5.3).

2.3 Instrumental setup

MegaCam (Boulade et al. 2003) on the Canada-France-Hawaii Telescope (CFHT) was an optimal choice for our program. It is an optical imager with a field of view (FoV) of $1 \times 1 \text{ deg}^2$ and a resolution of 0.187 arcseconds (arcsec or ") per pixel. It is one of the largest CCD mosaics which is not only used for surveys. The large area suits well our need to probe the entire dynamical range of density in the regions that feed our clusters.

The *u*, *g*, *r*, *i* and *z* filters² (centered on 374, 487, 625, 770, 890 nm, respectively; the filter curves are presented on Fig. 2.1) of MegaCam cover well the spectral energy distribution of the galaxies at $z \sim 0.4\text{--}0.5$ around the Balmer break, which is a crucial element to obtain accurate *photo-z*.

The CFHT is a 3.6 meters diameter telescope operational since 1979, located on Hawaii's Big Island near the summit of Mauna Kea mountain at an altitude of 4204 meters (see Fig. 2.2). The telescope has an equatorial mount (in orange in Fig. 2.3). Our target clusters are all located at declinations δ between -11° and -13° , just below the celestial equator. The 20° latitude of the CFHT is therefore well adapted to observe them.

The MegaCam instrument (Fig. 2.4), commissioned in 2003, is made of 40 charge-coupled devices (CCDs) of 2048×4612 pixels (~ 380 megapixels in total) and is positioned at the prime focus of the telescope. Before 2015, the 4 outer CCDs were not used due to vignetting by filters. The camera is cooled by a cryostat to a temperature of -120°C , to reduce the amount of thermal noise. Each CCD is separated by 13 arcsec gaps, but there are two larger gaps of 80 arcsec between the 1st and 2nd row of the CCDs, and the 3rd and 4th rows. On a 1 deg^2 field of view there is a high chance to observe a bright star, which can degrade the quality of the images by creating some bright halos around the star due to internal reflections in the telescope optics. The two large gaps are useful to hide these bright stars and minimize their influence on the exposures.

²http://www.cfht.hawaii.edu/Instruments/Imaging/Megacam/data.MegaPrime/MegaCam_Filters_data.txt

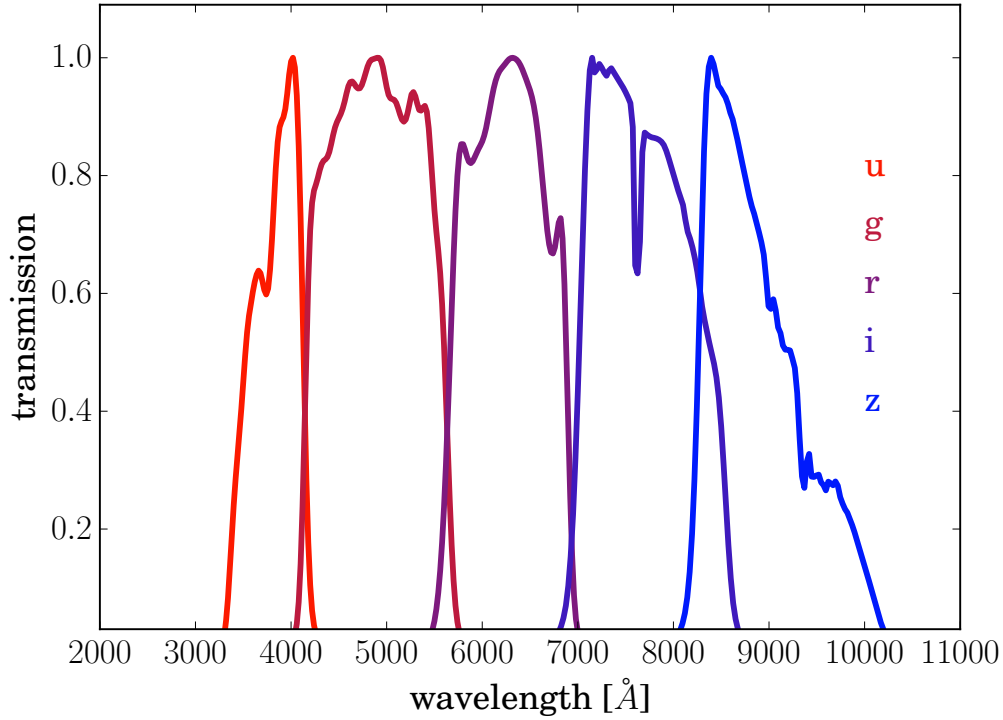


Figure 2.1 – Filter curves of MegaCam. They are normalized to 1 at the peak of the curve.

2.4 Exposure times

In order to securely define the cluster red sequence at $z = 0.5$ (see Section 4.2), we need to reach a signal-to-noise ratio $\text{SNR}=10$ at $r = 23.2$ mag (the magnitude limit³ for the wide-field low dispersion spectroscopic observations). We estimated conservative limits in the other bands using the galaxy colors from Fukugita et al. (1995). For the g -band, the most conservative limit is for an Elliptical template, which yields $g = 25$. For i and z , we use the Im template and find $i = 23.0$ and $z = 22.9$. Using the MegaCam direct exposure time calculator⁴, an airmass of 1.5, $0.8''$ seeing, we required the following exposure times: 25152 seconds in the u -band, 4320 seconds in g , 500 in r , 1440 in i and 6800 in z . We requested dark conditions for the u , g and r -band exposures and grey conditions for the i and z -band exposures.

³In what follows, we use the convention that a filter name, e.g. u , can be used either to mention the filter itself or the magnitude in that filter. Unless stated explicitly otherwise, all the magnitudes are measured in $1''$ radius apertures.

⁴<http://www.cfht.hawaii.edu/Instruments/Imaging/Megacam/dietMegaCam.html>



Figure 2.2 – The dome hosting the CFHT, atop Mauna Kea in Hawaii.



Figure 2.3 – The Canada-France-Hawaii Telescope, inside the dome.



Figure 2.4 – The 40 CCDs mosaics at the heart of MegaCam. The size of the square area is 25x25 cm. The two large gaps between the the 1st and 2nd row of CCDs, and the 3rd and 4th rows are well visible. A 2 cent euro coin is shown for scale.

2.5. Completeness of the program

field	filter	program ID	exp. time [s]	completion [%]	seeing ["]	m_{lim} [mag]	m_{90} [mag]
CL1301.7-1139							
	u	13AF22	2621	10	0.92	23.04	23.87
	g	13AF11	15120	350	0.75	24.73	24.38
	r	12AF07	500	100	0.66	23.07	23.78
	i	12AF07	1620	113	0.88	23.13	23.64
	z	13AF11	7480	110	0.68	22.22	22.88
CL1411.1-1148							
	u	13AF22	14675	58	1.13	24.68	25.13
	g	11AF13	7720	179	0.82	24.61	24.50
	r	11AF13	500	100	0.74	22.58	23.30
	i	11AF13	1440	100	0.55	22.75	23.33
	z	11AF13	6800	100	0.70	22.42	22.96

Table 2.2 – Journal of the observations. The total exposure time is provided as well as the completion rate. The magnitude limits m_{lim} is defined as the magnitude integrated in 1" radius apertures for a signal-to-noise of 10 (see Section 3.1.4) and m_{90} is the completeness limit measured in 1" radius apertures (see Section 3.1.6).

2.5 Completeness of the program

Observations were gathered over 4 years (2011-2014). However, the program is still incomplete, due to bad weather and a dome shutter failure in 2012. We obtained a complete *ugriz* photometric dataset for CL1301.7-1139 and CL1411.1-1148. CL1054.4-1146 has only partial *g* and *r*, which is not enough to achieve our analysis. CL1018.8-1211 has *griz*, which could be used to compute *photo-z*. However, the lack of the *u*-band strongly decreases the accuracy of the *photo-z* for galaxies at redshifts <0.4 , yielding a large pollution at the cluster redshift. For these reasons, only the fields targeting CL1301.7-1139 and CL1411.1-1148 are analyzed in this work.

The journal of the observations is presented in Table 2.2, along with basic characteristics of the images which will be described in details in Section 3.1. The completion rate, the ratio between the observed and requested exposure times, is globally excellent. For CL1301.7-1139 in *u*, the observations were only partially completed and the majority of the sub-exposures had a very high seeing (above 1"), we preferred not to use them, as it degraded the quality of the photometric redshifts (see Section 3.2.3). The same issue occurred for CL1411.1-1148 in *u*, but in this case the number of good exposure was too low to apply a cut in seeing, we kept them all. For CL1411.1-1148 in *g*, some exposures were taken twice by mistake. The completion rate is above 100 % in *g*, *i* and *z* for CL1301.7-1139, because some exposures were observed under non-photometric conditions and therefore repeated (up to 4 times in *g*).

3 Analysis methods

This chapter explains the technical procedures to extract physical measurements from the observations. The images are characterized (seeing, extinction, depths, etc.) in Section 3.1. The photometric redshifts are described in Section 3.2 and the stellar masses in Section 3.3. The density measure employed to probe the environment is presented in Section 3.4

3.1 Image characterization

3.1.1 Reduction

The MegaCam raw images are calibrated, aligned and coadded by the TERAPIX pipeline (Bertin et al. 2002) in a standard way. All the images are calibrated to have a photometric zeropoint of 30 in AB magnitudes¹.

Two colored images were created from the *ugr* images (Fig. 3.1 and 3.2). The red square is the FORS2 FoV. The green circles are the R_{200} of the clusters. The mosaics of MegaCam CCDs (Fig. 2.4) is visible: there is no data in the two large horizontal gaps, while the smaller ones appear less dark due to the higher noise in these regions. Bright stars creates circular artifacts due to internal reflections in the telescope, as well as long vertical “spikes” coming from saturation effects. These images illustrate the large FoV of MegaCam, compared to the FORS2 FoV and R_{200} . Bright, extended galaxies are visible (e.g., just below the FORS FoV in Fig. 3.1). It also qualitatively shows the difficulty to determine the nature and distance of the hundreds of thousands of the sources visible. By simple eye inspection of these images, we can only guess a few cases. The saturated objects are likely nearby stars in the Milky Way ($\lesssim 100$ pc) and the most extended galaxies are probably located within 100 Mpc. Red objects are expected to be more distant than blue ones. Still, the distance of almost all the sources are essentially impossible to guess.

¹For a measured flux f_v in an image, the corresponding AB magnitude is $m = -2.5 \log_{10} f_v + 30$.

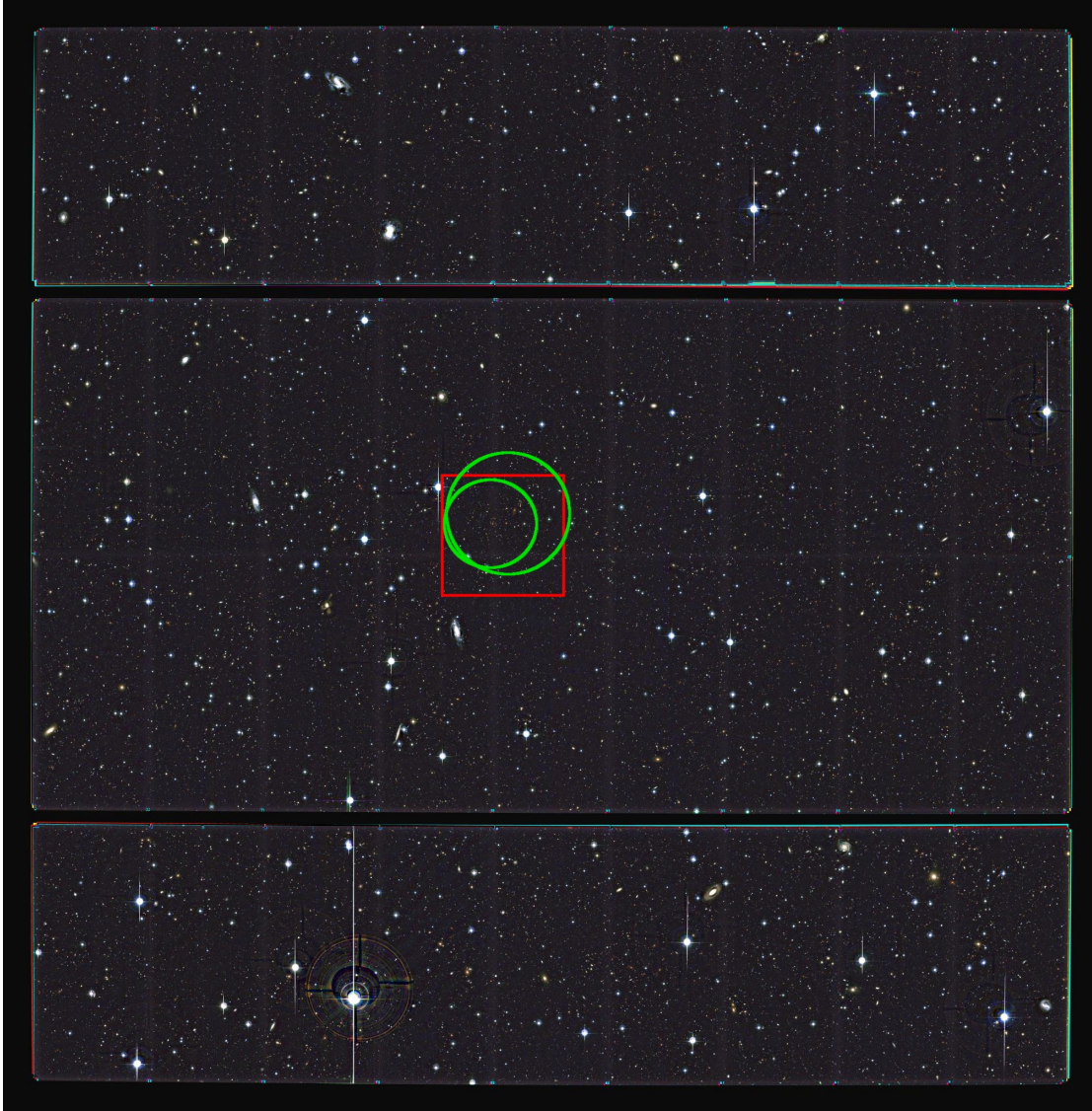


Figure 3.1 – Composite image of CL1301.7-1139, with u , g , r associated to blue, green and red pixel color, respectively. The red square is the FORS2 FoV. The green circles are the R_{200} of the clusters (small one: CL1301.7-1139a, large one: CL1301.7-1139). The mosaics of MegaCam CCDs (Fig. 2.4) is visible: there is no data in the two large horizontal gaps, while the smaller ones appear less dark due to the higher noise in these regions. Bright stars creates circular artifacts due to internal reflections in the telescope, as well as long vertical “spikes” coming from saturation effects. The original image is a square of approximately 20k x 20k pixels. Here we decreased the quality of the image to 2k x 2k pixels.



Figure 3.2 – Similar to Fig. 3.1, for the CL1411.1-1148 field instead of CL1301.7-1139.

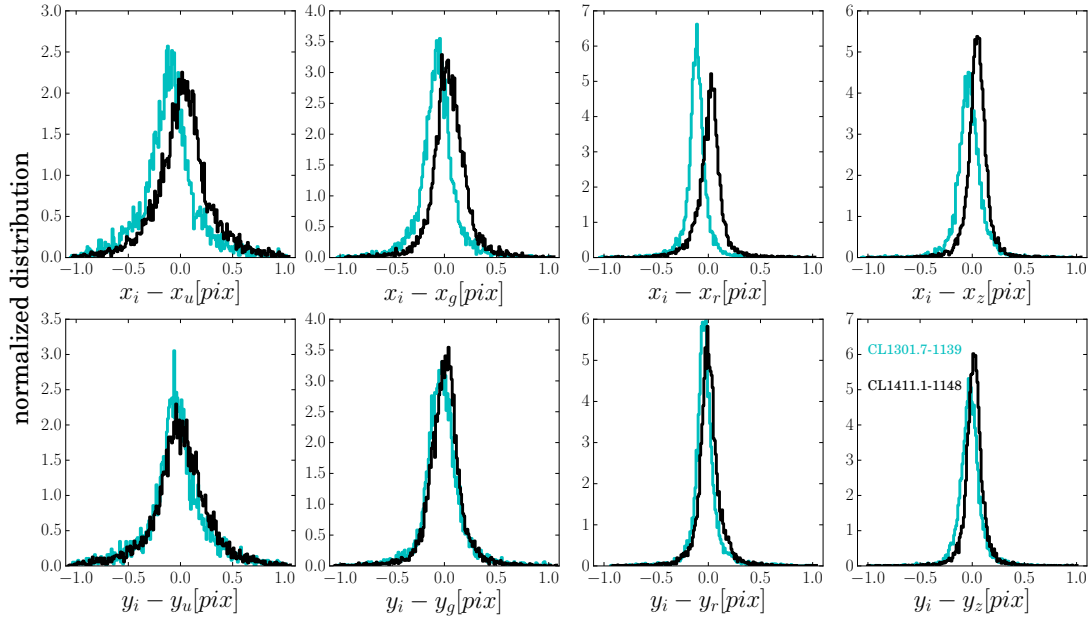


Figure 3.3 – Normalized distribution of the difference in pixels between the coordinates of the sources detected in i -band and in the other bands (e.g., x_g is the x pixel coordinate in the g -band).

3.1.2 Internal astrometry

The first check concerns the internal astrometry of the imaging. We need to make sure the images are well aligned, to avoid issues with the cross-matching of the detected sources. We run SExtractor (Bertin and Arnouts 1996) on each image and compute the difference between the pixel coordinates in the i band and the other bands for all the detected objects (Fig. 3.3). We focus on bright objects ($18 < i < 21$), since for faint objects the coordinates are less accurate and to ensure that the objects are detected in each band. The distribution of the difference in position is close to Gaussian, with mean and standard deviation σ smaller than $1/10$ of the pixel size, corresponding to 0.02 arcsec. The likelihood to have two distinct galaxies with such a small separation is very small. This high accuracy means that the cross-matching between the sources detected in each band (of the same field²) is straightforward.

3.1.3 Seeing and distortions

One of the most simple parameter giving the quality of an image is its seeing (its “sharpness”), which is a measure of the blurring of the images due to the atmospheric turbulences (e.g.,

²Here we use the term “field” to express the area on the sky observed by MegaCam. It is not related to the “field” in the context of galaxy environments. We will often write for instance “the CL1301.7-1139 field”, meaning the area on the sky observed by MegaCam around the CL1301.7-1139 cluster.

Tokovinin and Kornilov 2007). In principle, we could measure it by taking the Full Width at Half Maximum (FWHM) of the light profile of any unresolved object in the image. However, in general the profile of unresolved sources depends on their position on the charge-coupled device (CCD): optical distortions can increase locally their ellipticity (which should be zero) and stretch them. For this reason, we estimate the seeing statistically as the median FWHM of the bright, unsaturated³, small and low ellipticity objects. To ensure a consistent measure between each band, the selected objects are the same in every band. The sample is defined by the following cuts:

- $u < 21$, $18 < z$ (in 1" radius apertures): we need to select bright and unsaturated objects. Indeed the faint object could be unresolved galaxies, whose light distribution is not Gaussian and therefore their FWHM is not a good measure of the seeing. On the other hand, saturated objects can become artificially large. We also need to keep in mind that a star with a given magnitude in u -band will be (in general) brighter in the redder bands. Conversely, a star with a given magnitude in z will be fainter in bluer bands. For these reasons, we chose the faint magnitude cut in u and the bright one in z .
- FWHM: stars form a narrow locus in the magnitude-FWHM plane (Fig. 3.4). This yields the following cuts for u , g , r , i , z (in arcsec): 0.95, 0.85, 0.75, 0.95, 0.75 for CL1301.7-1139 and 1.17, 0.87, 0.8, 0.62, 0.8 for CL1411.1-1148.
- Ellipticity in all bands < 0.06 for CL1301.7-1139 and < 0.1 for CL1411.1-1148: the threshold has been chosen in a similar way as the fwhm, but in the magnitude-ellipticity diagram (Fig. 3.5). The selection is not as tuned as for the FWHM (the limits is the same in all bands), but we can see that the locus of unresolved objects (in cyan) is still well identified.

Fig. 3.4 shows the magnitudes as a function of FWHM for CL1301.7-1139 and CL1411.1-1148. The cyan dots represent the objects satisfying the above cuts and the black ones were selected with looser cuts ($10 < \text{mag} < 22$ and $\text{FWHM} < 1.5''$ in all bands) for comparison. Fig. 3.5 is the same with ellipticity instead of FWHM (the cuts stay exactly the same). In both cases, we see that our cuts select well the star sequence⁴. Fig. 3.6 shows the coordinates of the selected objects (in black). The field is also split in a 30x30 grid. At each point of the grid, the median FWHM of the 10 nearest objects is computed. The color code maps these medians. First, we see that the corners are empty. The optical distortions are the largest in these regions. It means that our cuts are slightly too strong, but since it concerns only a small area we do not

³A pixel in the CCD illuminated by a bright source will saturate if the exposure time is too long (for MegaCam, the maximum value is 65536 ADU). Above this limit, the remaining electrons will fill the neighboring pixels, thus enlarging artificially the size of the sources. This is why we see a knee in the magnitude-FWHM plane (Fig. 3.4): below the saturation threshold, the size of all the detected sources increases as magnitude decreases. The seeing measure would be biased by these saturated sources, therefore they are rejected.

⁴This sequence must actually contain unresolved galaxies, which we cannot remove without using informations on colors. However, for the seeing measure, we only care about selecting objects which are unresolved in all bands, whether they are galaxies or not.

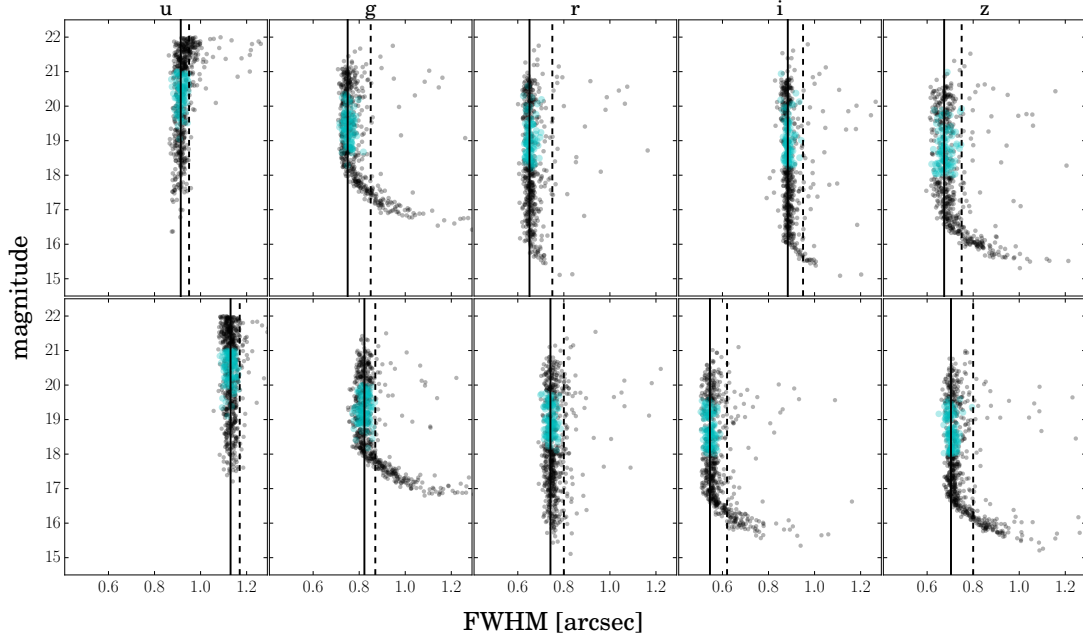


Figure 3.4 – Magnitudes (in a 1" radius aperture) versus FWHM for each *ugriz* band for CL1301.7-1139 (top) and CL1411.1-1148 (bottom). In cyan: objects considered as unresolved (see Section 3.1.3), in black: all the other objects in the catalog with $\text{FWHM} < 1.5''$ and $10 < \text{mag} < 22$. The knee at the bright end visible in g, i, z are due to saturation. The black vertical line is the median FWHM of the cyan objects, while the dashed line shows the FWHM cuts. To avoid overloading the figure, 70 % of the sources have been randomly removed.

change them (setting looser constraints would also increase the pollution by extended objects in the more central area). Second, we notice that these FWHM maps are non-homogeneous: there are non-negligible, non-linear local variations which are not the same in every band. Third, the FWHM range of the map is quite large (even after the median smoothing with the 10 nearest neighbors), reaching up to 10 % of the average seeing. To sum up, we cannot assign a “global” value for the seeing in each image. We choose to estimate the seeing as the median FWHM of the unresolved objects we selected (the black lines in Fig. 3.4). Table 2.2 contains the seeing measured for each cluster and band. For CL1301.7-1139 (CL1411.1-1148), the best seeing is in *i* (*r*) and the worst in *u* (*u*).

3.1.4 Noise estimation

In combined images, it is known that SExtractor underestimates the photometric errors, because the correlations between pixels resulting from the final stacking of the sub-exposure images is not taken into account. A formal estimation is challenging to obtain, since the noise is influenced by all the steps involved in the stacking (sky subtraction, calibration, alignment, coaddition, etc.). We prefer to adopt an empirical approach, where the errors are estimated

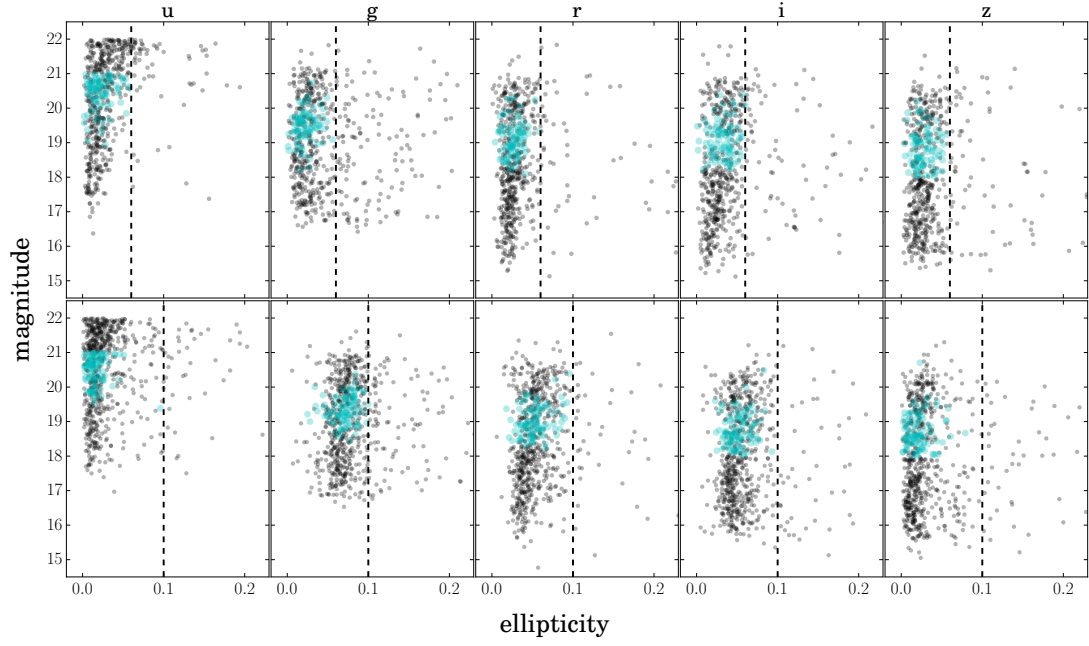


Figure 3.5 – Similar to Fig. 3.4. Magnitudes (in a 1" radius aperture) versus ellipticity for each *ugriz* band for CL1301.7-1139 (top) and CL1411.1-1148 (bottom). In cyan: objects considered as unresolved (see Section 3.1.3), in black: all the other objects in the catalog with $\text{FWHM} < 1.5''$ and $10 < \text{mag} < 22$. The dashed lines show the ellipticity cuts. To avoid overloading the figure, 70 % of the sources have been randomly removed.

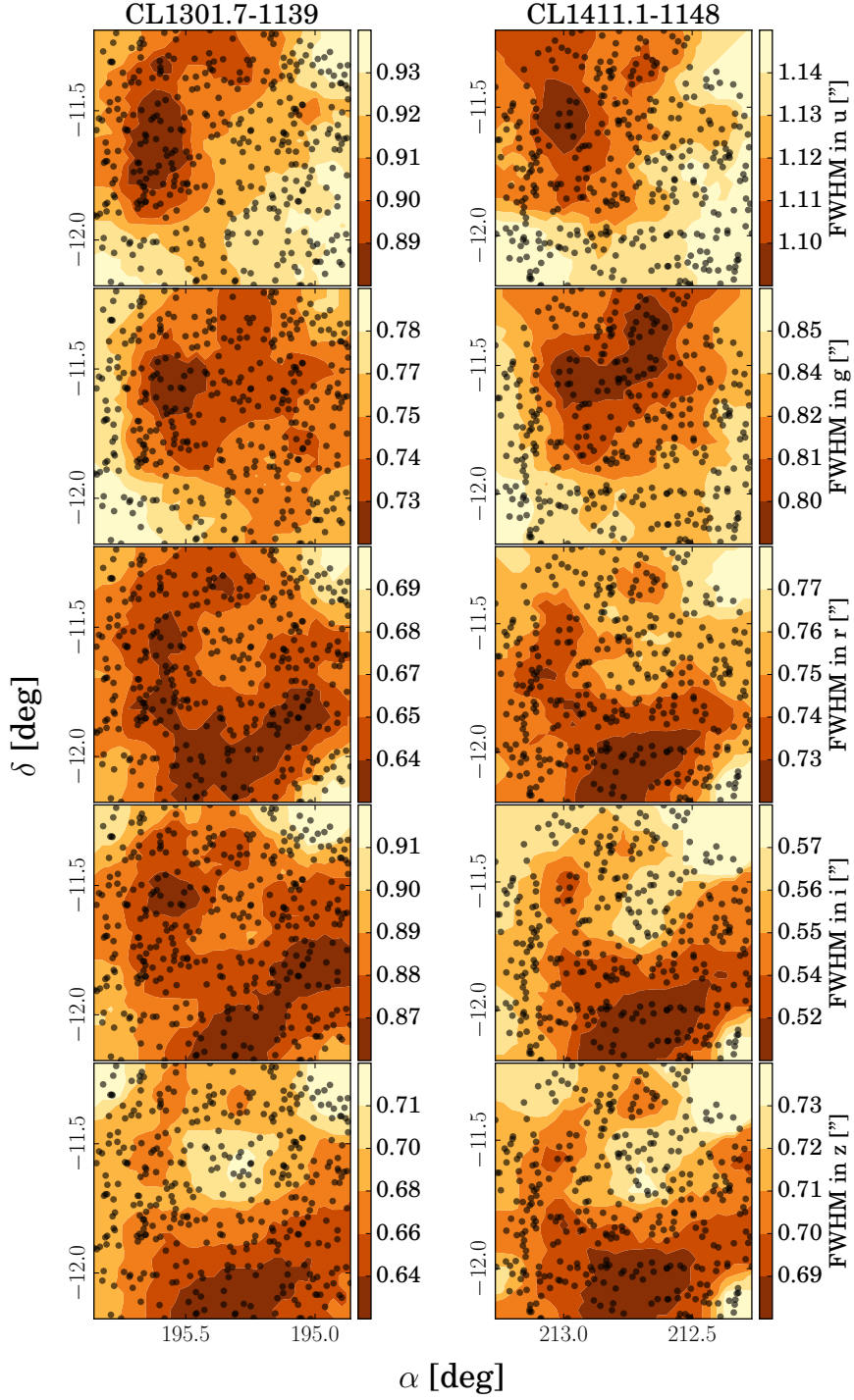


Figure 3.6 – FWHM maps for CL1301.7-1139 (left column) and CL1411.1-1148 (right column), constructed by computing the median FWHM of the 10 nearest unresolved objects (black dots, see Section 3.1.3) from each point of a 30x30 grid. The color scale is the FWHM in arcsec (each band per row). α is the right ascension and δ the declination.

directly from the stacked images. The method is inspired from Labbé et al. (2003). The idea is to compute the background error as a function of the aperture radius in which the flux is integrated. More precisely, in a given image, the procedure is:

1. Choose an aperture radius r_{aper} in pixels in which the flux will be measured.
2. Generate 10^5 random (pixel) coordinates x_i in the field area, keeping only the x_i which are at least at a distance $2r_{aper}$ from any detected source.
3. For each remaining x_i , measure the flux f_i within the aperture (it is just the sum of the pixels within a circle).
4. Compute the median m of the fluxes f_i and a rough estimate of the width of the distribution $w = \sqrt{\text{median}((f_i - m)^2)}$. Then, fit a Gaussian function on the distribution clipped such as the fluxes satisfy $|f_i - m| < 2w$. This clipping is useful to suppress the influence on the fit by extreme values, especially at the bright end where there might be a contamination of the fluxes by bright nearby objects. The standard deviation σ computed from the fit of the Gaussian is registered.
5. Repeat the steps 2 - 5 a few times. We chose $r_{aper} = 2, 3, 4, 5, 7, 10$ pixels (~ 0.4 -19 arc-sec). The histograms resulting from this step are shown in Fig. 3.7. Each histogram corresponds to one aperture. We see that the distributions are all close to Gaussian (the black dashed lines). The center is not exactly 0, but the offset is always smaller than the width of the distribution. It means that the background is not perfectly subtracted, but is below background noise.
6. Finally, we plot the dispersion σ for each aperture size as a function of the linear size $s = \sqrt{A}$, where A is the aperture area. We expect the curve to follow a relation of the type:

$$\sigma(s) = s(a + bs), \quad (3.1)$$

with a and b two parameters to be fit, related to the correlations between pixels and/or large scale fluctuations of the background.

This procedure allows to compute the flux error associated to any object. The only parameter needed is the surface A of the object, which in our case is given by the SExtractor ISO_AREA parameter (the area of the pixels detected above the analysis threshold ANALYSIS_THRESH). We show the error $\sigma(s)$ as a function of the linear size s on Fig. 3.8. There are significant variations between the bands and the fields. This is expected, since the exposure times are different and the fields were not observed in the same conditions.

The limit magnitude, m_{lim} , of the images is estimated as the median magnitude (in 1 arcsec radius apertures) of the objects with SNR within 10 ± 0.1 . It is given in Table 2.2.

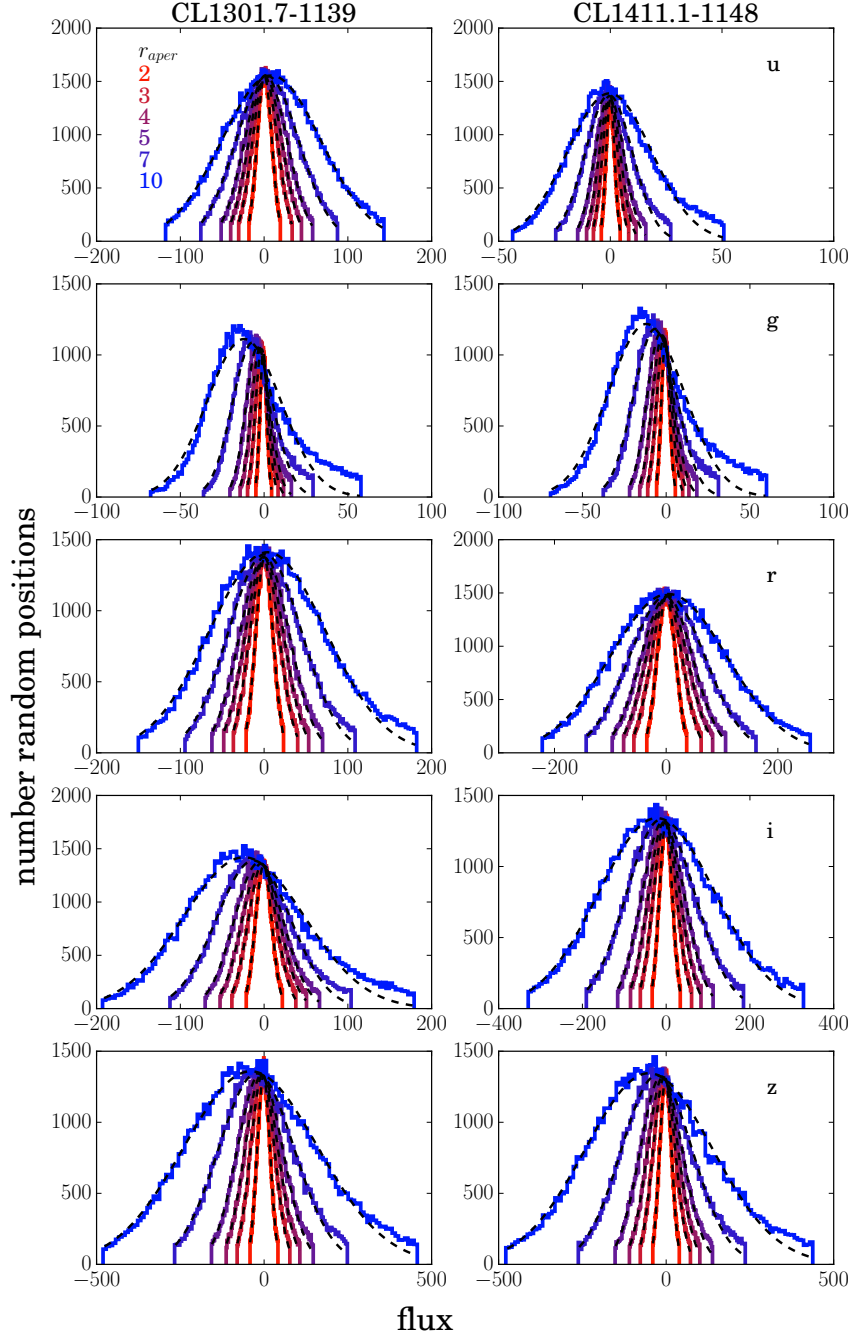


Figure 3.7 – Histograms of empty aperture flux for the background estimation. Each columns corresponds to a field and each row to a band. The zeropoint of the fluxes is 30 for AB magnitudes. The color of each curve corresponds to a different aperture radius r_{aper} (in pixels). Dashed lines are the Gaussian fits. For the largest apertures, there is a tail at bright end. This is a contamination due to nearby sources, however the influence on the fitted Gaussian is weak.

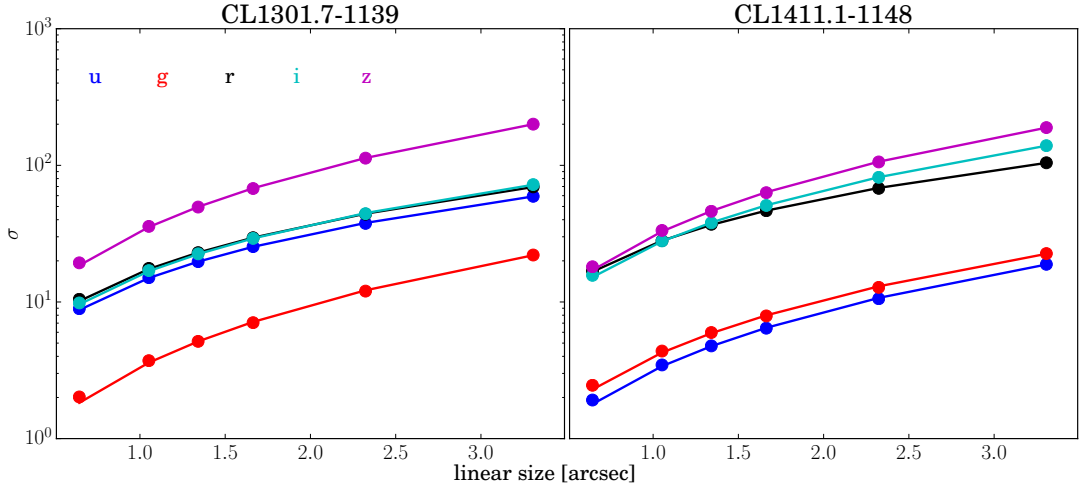


Figure 3.8 – Flux error as a function of linear size s . The units of the flux error are the same as the flux units in Fig. 3.7, i.e. they correspond to a zeropoint of 30 for AB magnitudes. The dots correspond to the width of the Gaussians in Fig. 3.7 and the lines are the fits from Eq. 3.1.

3.1.5 Extinction correction

The interstellar medium in the Milky Way absorbs the light emitted by extragalactic sources. This effect depends both on the area of the sky observed and on wavelength. We need to correct it to have access to the true flux emitted by the galaxies. We use the extinction curves from Cardelli et al. (1989) with the Schlegel et al. (1998) dust maps. For a given galaxy, the extinction is:

$$A_\lambda = (a(x)R_V + b(x)) \cdot E(B - V), \quad (3.2)$$

where $E(B - V)$ is the extinction in the B-V color⁵ (the only factor depending on the galaxy coordinates), $R_V = A(V)/E(B - V) = 3.1$, $a(x)$ and $b(x)$ are two polynomials defined as:

$$a(x) = 1 + 0.17699y - 0.50447y^2 - 0.02427y^3 + 0.72085y^4 + 0.01979y^5 - 0.7753y^6 + 0.32999y^7 \quad (3.3)$$

$$b(x) = 1.41338y + 2.28305y^2 + 1.07233y^3 - 5.38434y^4 - 0.62251y^5 + 5.3026y^6 - 2.09002y^7 \quad (3.4)$$

where $y = x - 1.82$, $x = 1/\lambda_{\text{eff}}$. The values of λ_{eff} , the effective wavelength of a given filter, are

⁵B and V are the magnitudes in the corresponding standard Johnson filters (Johnson and Morgan 1953). By convention, the name “color”, unless it is employed to describe the color codes in figures, means the difference of the magnitude in two different filters. In general, the first term of a color is the bluest filter, e.g. we prefer to use “B-V color” instead of “V-B color”. In this case, we say that a source with a higher value of color than another source is more red.

field	filter	min	median	max
CL1301.7-1139				
	<i>u</i>	0.18	0.22	0.27
	<i>g</i>	0.14	0.17	0.21
	<i>r</i>	0.10	0.13	0.15
	<i>i</i>	0.08	0.09	0.11
	<i>z</i>	0.06	0.07	0.09
CL1411.1-1148				
	<i>u</i>	0.25	0.28	0.39
	<i>g</i>	0.19	0.21	0.29
	<i>r</i>	0.14	0.16	0.22
	<i>i</i>	0.10	0.12	0.16
	<i>z</i>	0.08	0.09	0.12

Table 3.1 – Minimum, median and maximum extinction correction (A_λ) for each band and field.

0.374, 0.487, 0.625, 0.77, 0.89 μm for *u*, *g*, *r*, *i*, and *z* respectively⁶.

Maps of the extinction A_λ are represented on Fig. 3.9 for CL1301.7-1139 (top row) and CL1411.1-1148 (bottom row). For a given field, the shape of the map is the same in each band, but the value of the maps depends on the band. It varies significantly locally: this justifies an extinction correction computed for each object separately. The strongest extinction is in the *u*-band. Table 3.1 gives the minimum, maximum and median extinction for each band and field.

3.1.6 Completeness

The completeness of an image is an estimation of the faintest magnitude at which all the sources are detected. They are calculated from the number counts of the systems detected with $SNR > 5$ (Fig. 3.10). We fit a power law and a polynomial in the regions where the number counts start to decrease (e.g. for $i=22-24$ for the *i*-band in Fig. 3.10). The 90% completeness limit m_{90} is taken as the magnitude for which the ratio between the polynomial and the power law fit is 0.9. These completeness magnitudes are reported in Table 2.2. The real shape of the number counts in each band is not known, so the power law shape is not necessarily justified (especially in *u* and *g*). Nevertheless, there is no physical reason for the sudden drop at faint magnitudes, therefore the comparison between the polynomial and the power law is good enough for the estimation of the completeness.

It is possible to estimate more accurately the completeness by adding artificial sources and compute the fraction recovered after the SExtractor run. However, for us the completeness is just an indicative number of the observations depth. It does not intervene directly in any

⁶For instance, the extinction corrected magnitude in *u* is $u_{ecor} = u - A_u$ (for a given source).

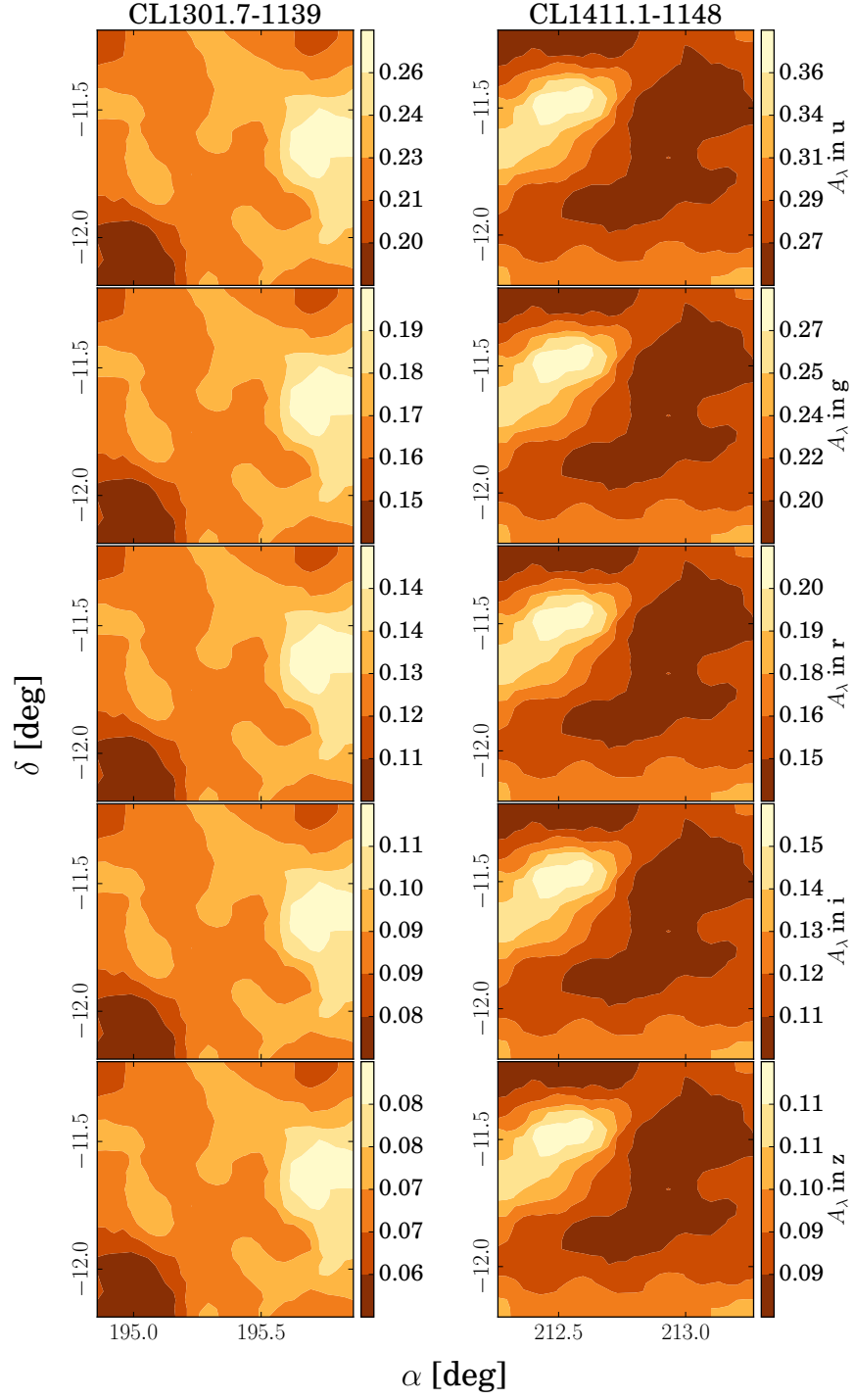


Figure 3.9 – Extinction corrections maps for CL1301.7-1139 (left column) and CL1411.1-1148 (right column). Each row corresponds to a band. The color code is A_λ , in magnitude units.

computation, so we will not attempt to improve our method.

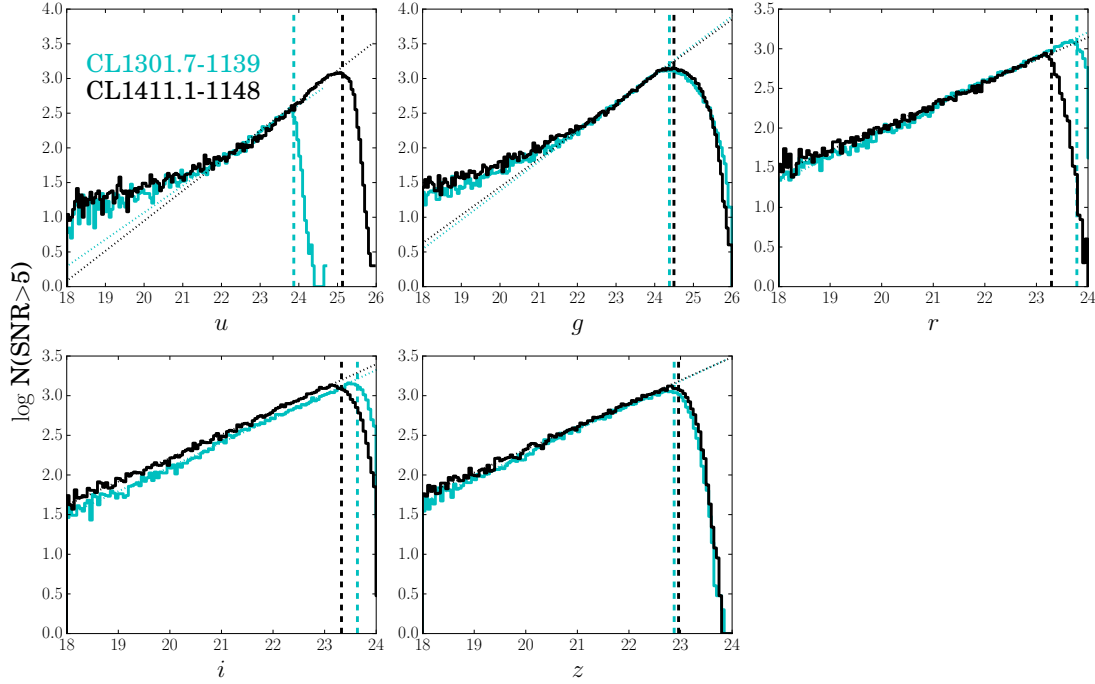


Figure 3.10 – Number counts for each band and field, keeping only sources with $\text{SNR} > 5$. The dotted line is the power law fit and the dashed line is the 90% completeness limit m_{90} .

3.2 Photometric redshifts

Photometric redshifts have been extensively used in a broad range of contexts (e.g., Pelló et al. 2009; Hildebrandt et al. 2012). They provide a rather cheap way to analyze statistically basic galaxy properties (rest-frame colors, stellar masses, star formation rates, etc.) over large samples. While obtaining redshifts from spectra is rather straightforward (you “only” need to match emission or absorption lines and the best reachable accuracy is almost completely determined by the spectral resolution), *photo-z* can always be fine-tuned and improved. In this section, I will explain our procedure to obtain accurate *photo-z*, what is the accuracy we are able to reach and the different cuts which are applied to remove outliers and increase the precision.

3.2.1 Code

Photometric redshifts are usually classified into two categories: the model-based and empirical methods.

The first category uses galaxy templates (e.g., Fig. 3.12) to fit the photometry (e.g., EAZY, Brammer et al. 2008; BPZ, Benítez 2000; Hyperz, Bolzonella et al. 2000; LePhare, Arnouts et al.

1999, Ilbert et al. 2006). For a given observed galaxy, the idea is to convolve the templates with the different filters used in the observations to obtain synthetic photometry, repeat this over a redshift grid and then find the template and redshift for which the synthetic photometry matches best the observed photometry. This method has the advantages of giving automatically information on the galaxy type (since we know which template is used) and to be easy to test: a sample of galaxies with spectroscopic redshifts can be compared directly to the *photo-z* to assess their accuracy and the χ^2 between synthetic and observed photometry gives a goodness-of-fit information. There is also no dependence on the amount of data at hand (spectroscopy is useful to check the accuracy, but does not influence directly the method). On the practical point view it is usually fast to execute and relatively easy to implement. The disadvantages are that there are several inputs to supply, each of them implying potential errors: the filter curves (usually given as a combination of atmospheric extinction, CCD quantum efficiency and filter response; all these measures have errors and can vary over time), the templates library (which must represent correctly the true galaxy population of the sample) and the photometry (which must be measured consistently across all bands to match the templates).

The second category is based on machine-learning algorithms (e.g., TPZ, Carrasco Kind and Brunner 2013; AnnZ, Collister and Lahav 2004). They use a catalog with high-accuracy redshifts to train the test photometric sample and predict redshifts according to the photometric properties of the galaxies. The main advantage of these methods is that the only inputs required are the photometry of the two samples and the high accuracy redshifts of the training sample (there is no need for templates or filter curves). One of their disadvantage is that their accuracy is difficult to test. In template based *photo-z* estimates, one can use a set of data with spectroscopic redshift to test the accuracy of the *photo-z*. In machine-learning based methods, since a training sample must be provided to train the data, testing the algorithm on the same sample will bring too accurate results. One solution could be to use half the spectroscopic sample to train the algorithm and the other half to test the accuracy. Unfortunately, since the training is sample would be smaller in this case, the algorithm would be less effectively trained and the accuracy would be underestimated. Another negative point is the “black box” aspect of these codes: the algorithms are usually rather complicated (and require an important computing power), involve randomness and it is difficult to analyze all the steps involved for the redshifts estimation.

We choose to use EAZY (revision 54; Brammer et al. 2008), a recent template based algorithm. It possesses several advanced features, like taking into account the template errors and including magnitude priors.

Parameters

EAZY uses an apparent magnitude prior based on synthetic lightcones from semi-analytical models in the *R*-band, to help breaking degeneracies between low and high redshift. It is shown for different magnitudes in Fig. 3.11. We see that it essentially shuts down the likelihood

to have high redshift galaxies. The closest CFHT band from R is r (central wavelengths of 658 and 625 nm, respectively). We computed the photometric transformations between R and r (Jester et al. 2005), considering the extreme case of $r - i = 1.5$, and obtained $r - R \sim 0.4$. Taking into account the photometric errors and the fact that the prior is only sampled in 0.5 mag bins, the difference between R and r can be neglected. We apply the R prior to the r band, without any further correction.

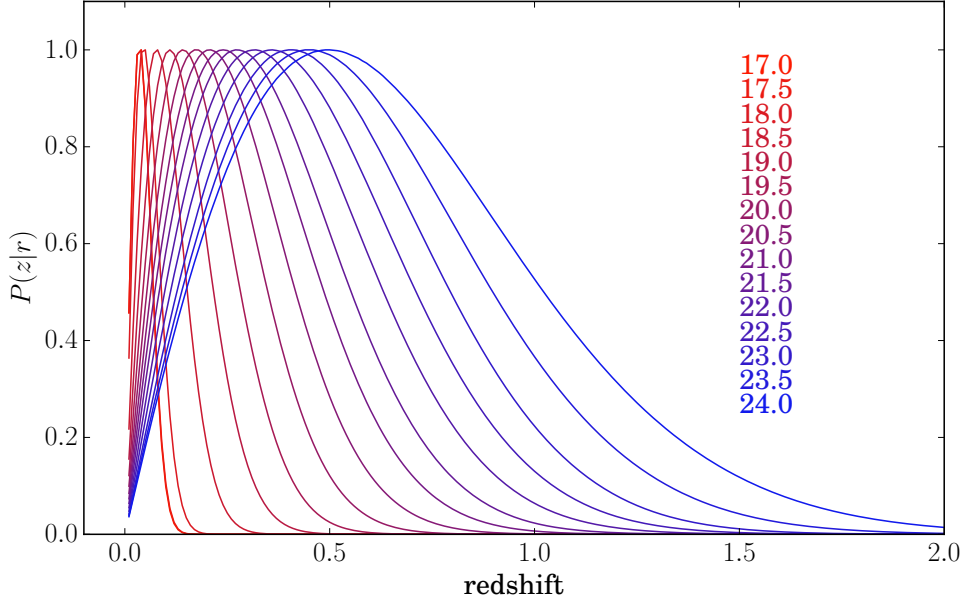


Figure 3.11 – EAZY prior $P(z|R)$ for magnitudes $16 < R < 24$ (the typical magnitude range of our data, see e.g. Fig. 3.10). They are normalized to 1 at the peak of the curve.

For the redshift estimation, we use the redshift marginalized over the posterior probability distribution function:

$$z_{\text{phot}} = \int z \cdot p(z|\text{data}, R) dz, \quad (3.5)$$

with $p(z|\text{data}, R) = p(z|\text{data}) \cdot p(z|R)$, the prior $p(z|R)$ and the likelihood computed from the template fits $p(z|\text{data}) = \exp[-\chi^2(z)/2]$, where

$$\chi^2_{z,i} = \sum_{j=1}^{N_{\text{filt}}} \frac{(T_{z,i,j} - F_j)^2}{(\delta F_j)^2}, \quad (3.6)$$

with N_{filt} the number of filters, $T_{z,i,j}$ the synthetic flux of template i in filter j for redshift z , F_j the observed flux in filter j , and δF_j the uncertainty in F_j .

The filter curves for MegaCam are already included in EAZY (numbers 88-92; Fig. 2.1). They represent the combination of the atmospheric extinction, CCD quantum efficiency and filter response.

We choose a redshift grid ranging from 0.01 to 2, with steps of 0.01. The exact value of these bounds is not crucial, since *i)* the number of very low redshift galaxies expected is low and they would be saturated in the images, *ii)* our observations are designed for galaxies at intermediate redshifts, the likelihood to detect galaxies at $z \geq 1$ in all bands is low and *iii)* the prior (realistically) tends to forbid $z=0$ and $z \geq 1.5$ galaxies for our magnitude range. Steps of 0.01 are also small enough: we do not expect to reach a better accuracy for the *photo-z* (see Section 3.2.4) and the final redshift estimation (Eq. 3.5) is given with a resolution of 0.001 anyway.

The values of all the other parameters are the default ones.

Template library

The choice of the galaxy templates is a challenging task. They should be sufficiently numerous and diverse to reflect the real SED of all the galaxies in our sample. However, adding more templates increases degeneracies. The library used actually depends on the filter set: the more filters you have, the more template you can use. In our case, we choose a library optimized for the CFHT Legacy Survey (Ilbert et al. 2006), since the filter set is the same as ours and the survey depths are not too different. Fig. 3.12 shows the SEDs of the galaxies in the library.

EAZY can compute linear combinations of the templates to fit the photometry. It improves the results when a small set of template is provided (like the default one). In our case, the template library is already rich and allowing this feature increases largely the degeneracies. For this reason, we chose not to use it.

3.2.2 Calibration spectroscopic sample

Our *photo-z* strategy was checked against a set of spectra in the field of our two targets: 146 medium resolution redshifts from FORS2 (Halliday et al. 2004; Milvang-Jensen et al. 2008) within $\sim R_{200}$ of our target clusters and 2025 low resolution spectra from Magellan/LDP with a 0.02 redshift accuracy (3σ).

3.2.3 Optimized photometry

Accurate *photo-z* require a very carefully constructed photometric catalog. Instrumental effects and observing conditions are not directly considered by *photo-z* algorithms and can result in systematic errors. These effects cannot always be suppressed, but their influence can be decreased if they are taken into account when creating the photometric catalog.

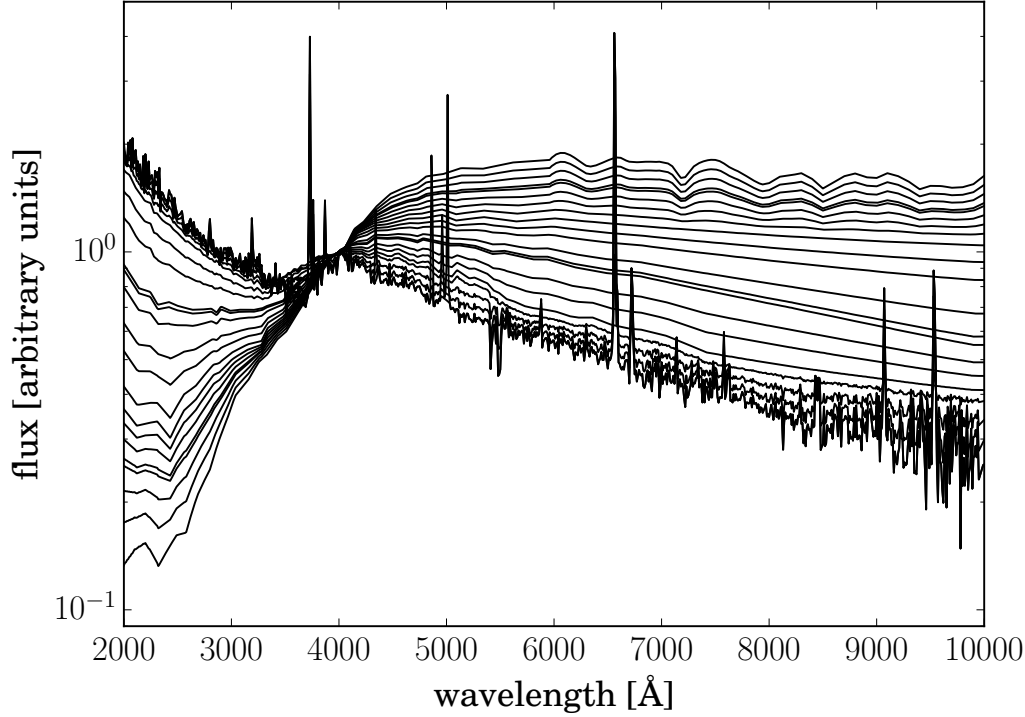


Figure 3.12 – Template library. The fluxes are normalized to 1 at 4000 Å. To avoid overloading the figure, only one third of the templates are shown (the removed templates would be in between each curve).

Seeing-matching

The first issue comes from the fact that the images were taken under different photometric conditions. In particular, the seeing can vary significantly. The effect of the seeing is to blur the images, with the consequence of diluting the flux of the observed galaxies over a larger area than the true light distribution of the galaxy. For low SNR galaxies, a large fraction of the flux can fall below the sky level and will not be measured. In the worst case scenario, this effect can even prevent some galaxies to be detected at all. To allow a consistent flux measure across all the images, one solution is to degrade the quality of the best quality images to match the seeing of the worst one. This ensures that the effect of the seeing is the same in each band. It can be achieved by convolving the best seeing images with a Gaussian kernel⁷.

For each image, the kernel width was determined iteratively until the measured seeing in the convolved images was within 0.02 arcsec of the worst seeing image. Fig. 3.13 shows

⁷In a first approximation, the light profile of stars follow a Gaussian distribution. Hence for two images with seeing s_1 and s_2 , $s_1 < s_2$, if the first image is convolved with a gaussian of width σ_{conv} such as $s_1^2 + \sigma_{\text{conv}}^2 = s_2^2$, we obtain a new image whose seeing is approximately equal to s_2 .

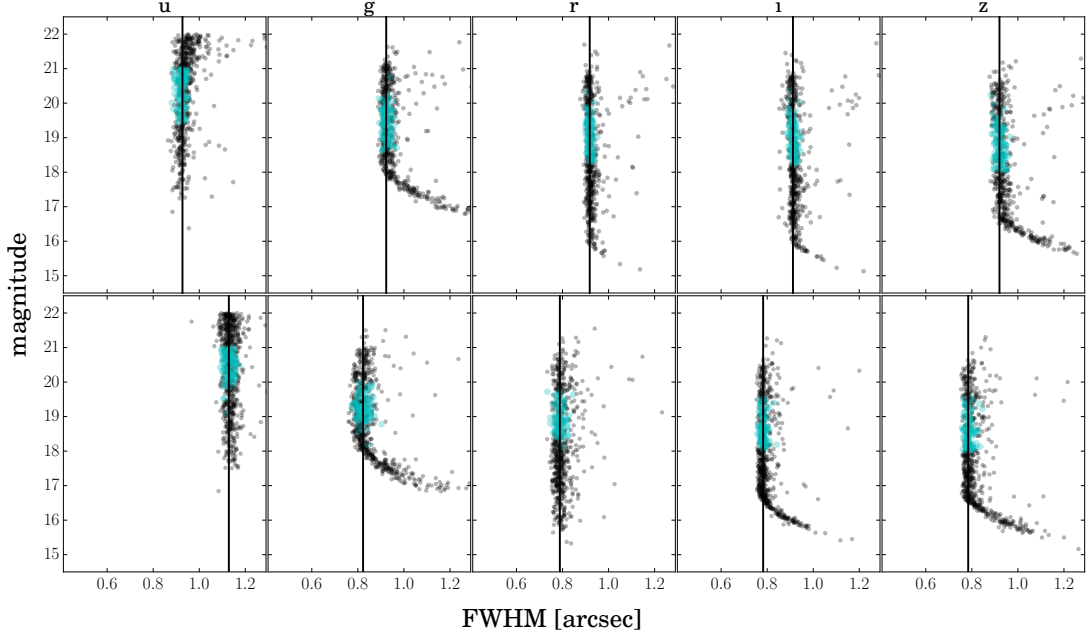


Figure 3.13 – Magnitudes (1" radius aperture) against FWHM for each seeing-matched images for CL1301.7-1139 (top) and CL1411.1-1148 (bottom). In cyan: objects considered as unresolved, in black: all the other objects in the catalog with $\text{FWHM} < 1.5''$ and $10 < \text{mag} < 22$. The knee at the bright end visible in g , i and z are due to saturation. The black vertical line is the median FWHM of the cyan objects. Similar to Fig. 3.4. To avoid overloading the figure, 70 % of the sources have been randomly removed.

the magnitude-FWHM plane for sources detected in the convolved images. The unresolved sources used for the seeing measure (black line) are in cyan. The cuts selecting them are determined by the procedure described in Section 3.1.3. We also checked that all the FWHM maps spanned a similar range after the convolution (Fig. 3.14). For CL1301.7-1139, we used the u -band as reference (0.92" seeing), while for CL1411.1-1148, since the seeing in the u -band (1.13") is really too different from the other bands, we convolved the images in order to match the seeing in the g -band (0.82"). The u image was not modified. This implies a systematic loss of flux in u compared to the other bands. However, the difference will partially be absorbed when we fit the zeropoint of each image (Section 3.2.3). We checked that the *photo-z* accuracy was improved with this choice not to degrade the CL1411.1-1148 images to the u -band seeing.

The two-image mode

The second problem is related to the multiwavelength aspect of the images. In general, the observed shape of a galaxy will depend on the filter used. E.g., a galaxy can have an old and massive bulge surrounded by an extended and elongated star-forming disk, which will make it look small and round in a red band (e.g. z), but larger and more elliptical in a blue

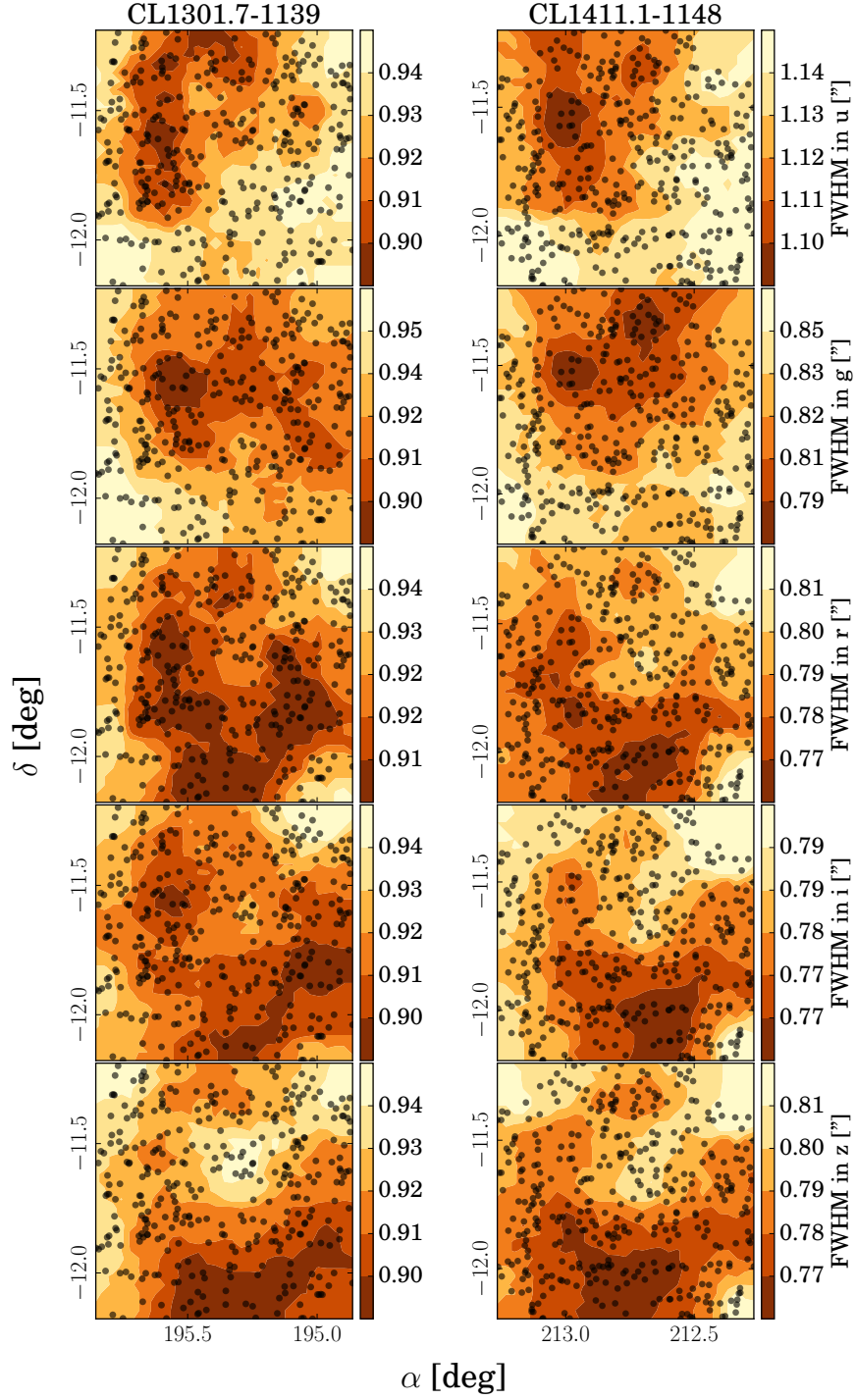


Figure 3.14 – FWHM maps for the convolved images of CL1301.7-1139 (left column) and CL1411.1-1148 (right column). Each row corresponds to a band. The black dots are the unresolved objects. Similar to Fig. 3.6, but with the convolved images instead of the original ones.

band (e.g. u). In this case, a naive algorithm may only measure the flux of the bulge of the galaxy in the red band, while integrating the whole galaxy in the blue, yielding inconsistent colors (thus erroneous *photo-z*). One way to circumvent this issue for a given galaxy is to use a fixed aperture across all the bands. The two-image mode of SExtractor is designed for this: an image is chosen for the source detection and the definition of the aperture for the flux integration, while the flux itself is measured in the other image. Another advantage of this mode is that it allows to define the aperture in the best seeing image, meaning that the aperture will be closer to the true light distribution of the object detected.

It is tempting to choose the bluest band, u , for the detection, since this is generally where the galaxies look larger. However, a detection in u will be biased towards star-forming galaxies. A redder band is more appropriate, it will be in general closer to a stellar mass selection. We choose the i -band instead of z (the reddest band), because the seeing in z is worse than in i .

Flux measure type

The apertures used for the magnitudes measurement is crucial. If a large aperture is chosen, the measured flux far from the galaxy center will be dominated by the sky (and consequently overestimated), while if a small aperture is employed, there is a risk to miss a significant fraction of the galaxy flux. The shape of the aperture should also follow as much as possible the light distribution of the galaxy. E.g., if it is seen from the edge, a circular aperture will both contain a lot of noise (along the rotation axis) and likely miss some flux (along the disk plane). To sum up, the ideal aperture should be *i*) small enough to keep a good signal to noise ratio (and avoid contamination by nearby objects), *ii*) large enough to contain most of the total flux and *iii*) follow the light distribution. Our best choice is to use the isophotal magnitudes, where the flux aperture is determined from all the pixels above the detection threshold (which we chose to be two σ above the background, DETECT_THRESH=2 in SExtractor).

Zeropoint fitting

Even with careful photometric measurements and a thorough choice of SED library, the agreement between data and templates may not be perfect and result in systematic errors in the *photo-z*. Therefore, we applied a procedure to fit the photometric zeropoint in each band. The first part is made of 3 steps:

1. Compute synthetic photometry with EAZY, fixing the redshift to the spectroscopic redshift z_{spec} (when available).
2. For each galaxy and each band, compute the difference between synthetic and observed magnitude.
3. Computed the median of the difference for all galaxies and for each band. This provides the systematic shift between the model SEDs and our observations to be corrected.

4. Repeat steps 1-3 until the shift in each band is smaller than a given threshold (e.g., 0.01 mag).

We repeated the above three steps until the shifts between the synthetic and observed magnitudes in each band was smaller than 0.01 mag. We stress that this zeropoint correction is not necessarily related to systematic errors in the image calibration, it should be understood as an optimization of the compatibility between our specific dataset and the templates.

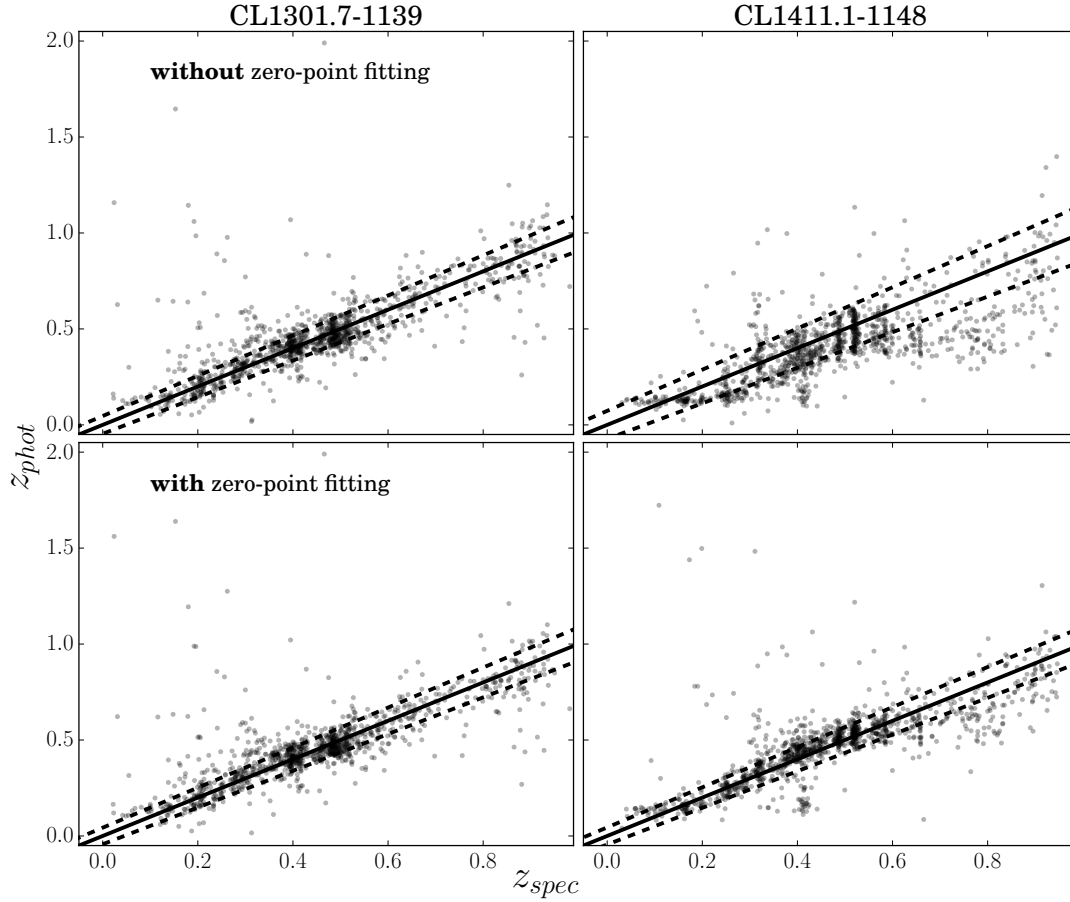


Figure 3.15 – Photometric against spectroscopic redshifts for CL1301.7-1139 (left) and CL1411.1-1148 (right), before (top) and after (bottom) the zeropoint fitting. Spectroscopic redshifts come from FORS2 and LDP. The solid line shows the 1:1 relation, while the dashed lines correspond to $\pm(1 + z_{\text{spec}}) \cdot \sigma_{\text{NMAD}}$.

A second correction was then applied using the medium resolution FORS2 spectroscopic redshifts and the low resolution IMACS ones in hand:

1. EAZY was run on our spectroscopic sample with the zeropoints determined above, however this time leaving free the photometric redshift of the galaxies.

2. Galaxies with $|\Delta z| = |z_{\text{spec}} - z_{\text{phot}}| > 0.15$ are rejected from the analysis.
3. The zeropoint shifts were modified with a least-square algorithm to minimize the χ^2 between the z_{spec} and z_{phot} .

The result of this procedure is illustrated in Fig. 3.15, showing the photometric against the spectroscopic redshifts before (top) and after (bottom) the zeropoint fitting. We see a decrease of the scatter (dashed lines) after the zeropoint fitting. For CL1301.7-1139 (left), the result of this procedure improves only slightly the accuracy of the *photo-z*, but for CL1411.1-1148 (right), the improvement is striking. This is due to the seeing matching which was not done for CL1411.1-1148, making the *u* magnitudes inconsistent with the others without the zeropoint correction.

3.2.4 Final *photo-z* sample

In order to select a galaxy sample as robust and unbiased as possible from which the large scale structures around our three targets clusters could be identified, we applied a few selection criteria to the full sample of systems detected by SExtractor.

FWHM

Stars are a strong source of contamination in the *photo-z*. In an image, a faint star may have the same characteristics as a distant unresolved galaxy (e.g., similar shape, FWHM and magnitude). Even with 5-band photometry, it remains surprisingly difficult to robustly identify stars. The most simple technique to remove them is based on geometry: stars are not resolved in our images⁸. In principle we could apply the criteria we used to determine the seeing (Section 3.1.3), i.e. consider stars as small ellipticity and low FWHM objects in all bands. Unfortunately, this works only for bright stars. Indeed, for low SNR objects, the FWHM measure is increased by the influence of the sky background. For this reason, we consider stars as low FWHM objects in the band with the lowest seeing. Fig. 3.16 illustrates our choice in the magnitude-FWHM plane. The FWHM cut is represented by the black vertical line (0.75" in *r*-band for CL1301.7-1139, 0.65" in *i* for CL1411.1-1148). Sources above (below) this cut are in black (cyan). We see that above the magnitude limit (m_{lim} , dashed horizontal line), the FWHM of unresolved objects increases. Some unresolved galaxies may be included in this selection, but in most cases these galaxies are faint and their SNR is too low anyway to yield an accurate photometric redshift.

Another possibility is to identify stars with SED fitting. We could use EAZY with fixed $z=0$ and a star template library instead of galaxy templates and compare the χ^2 to infer if the object is more likely to be a star or a galaxy. This method is however difficult to calibrate. The number of degrees of freedom of each fit is not the same (fixed z or not, different size of library), thus

⁸The apparent size of a star is much smaller than the seeing value.

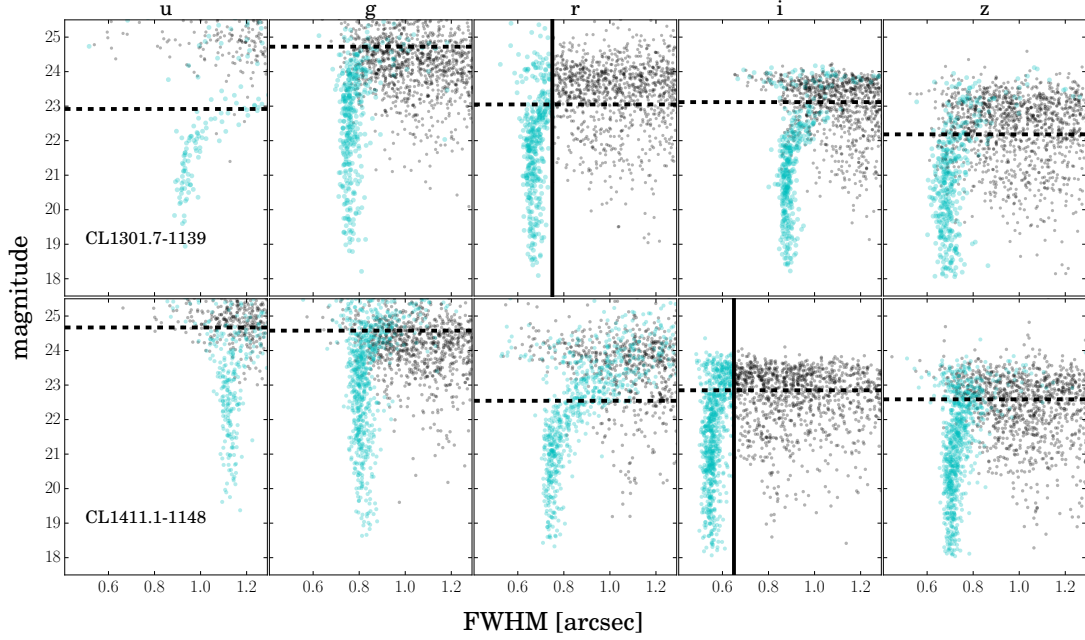


Figure 3.16 – This figure show the star/galaxy separation. It is based on a FWHM limit in the image with the best seeing. This limit (solid vertical line) is 0.75" in r -band for CL1301.7-1139, 0.65" in i for CL1411.1-1148. cyan: sources with FWHM below the FWHM cut, considered as stars; black: sources above the FWHM cut. The horizontal dashed lines show the magnitude limit m_{lim} . To avoid overloading the figure, we removed the sources with $\text{SNR} < 5$ and saturated objects with $z < 18$. Furthermore, 95 % of the objects have been randomly removed (it makes the sampling in the u -band a little too low, but it does not harm the purpose of the figure).

the comparison of the χ^2 is not straightforward. Moreover, it can induce color biases in the galaxy sample, which could strongly harm the later stages of our analysis.

Odds parameter

EAZY provides a parameter, *odds*, assessing the quality of the *photo-z*. It quantifies the probability that the redshift lies within ± 0.1 of the redshift estimate⁹ (given by Eq. 3.5):

$$\text{odds} = \int_{z_{\text{phot}} - 0.1}^{z_{\text{phot}} + 0.1} P(z|\text{data}, R) dz. \quad (3.7)$$

We computed the fraction of outliers f_{outliers} , defined as the fraction of galaxies with $|\Delta z| > 0.15$, and the accuracy of the *photo-z*, estimated with the normalized median absolute deviation $\sigma_{\text{NMAD}} = 1.48 \cdot \text{median}(|\Delta z - \text{median}|\Delta z|)$, as a function of *odds* (Fig. 3.17). As expected, f_{outliers} and σ_{NMAD} increase when *odds* decreases. Based on this figure, we chose to reject

⁹In the original code, the probability is computed around ± 0.2 . I have modified the code to make the *odds* parameter more sensitive.

galaxies with $odds < 0.8$. It is a good trade-off to minimize the outliers without removing too many galaxies (on the bottom panel of Fig. 3.17, we see that the majority of the galaxies are above $odds=0.8$).

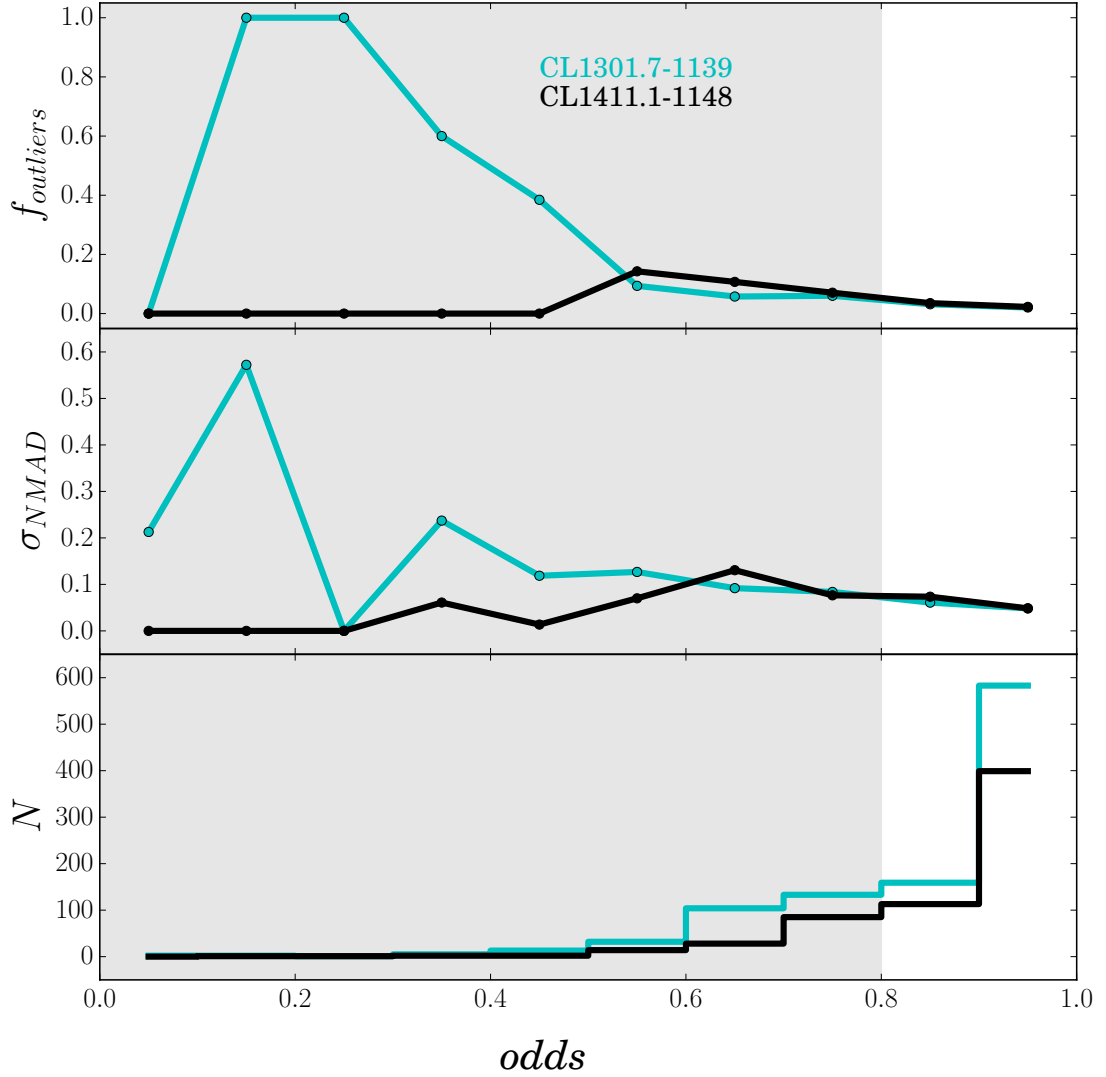


Figure 3.17 – This figures illustrates how we choose the cut in $odds$. Fraction of outliers (top), σ_{NMAD} (middle), number of galaxies with spectroscopic redshift (bottom) as a function of $odds$ (in bins of width 0.1). The shaded area represents the area below the cut in $odds$ at 0.8. The black (cyan) line corresponds to the CL1411.1-1148 (CL1301.7-1139) field.

Magnitude

On the bright end, we remove saturated sources by applying a cut at $i < 18$. We chose the i -band because it was used for the detection. We prefer to apply magnitude cuts always in the same band, to avoid color selection effects. The value of the limit is driven by the g -band,

where the saturation occurs at the faintest magnitude. Fig. 3.18 shows the magnitude-FWHM plane, with sources fainter (brighter) than $i = 18$ (dashed line) in cyan (black). With see that none of the cyan objects are in the saturation knee.

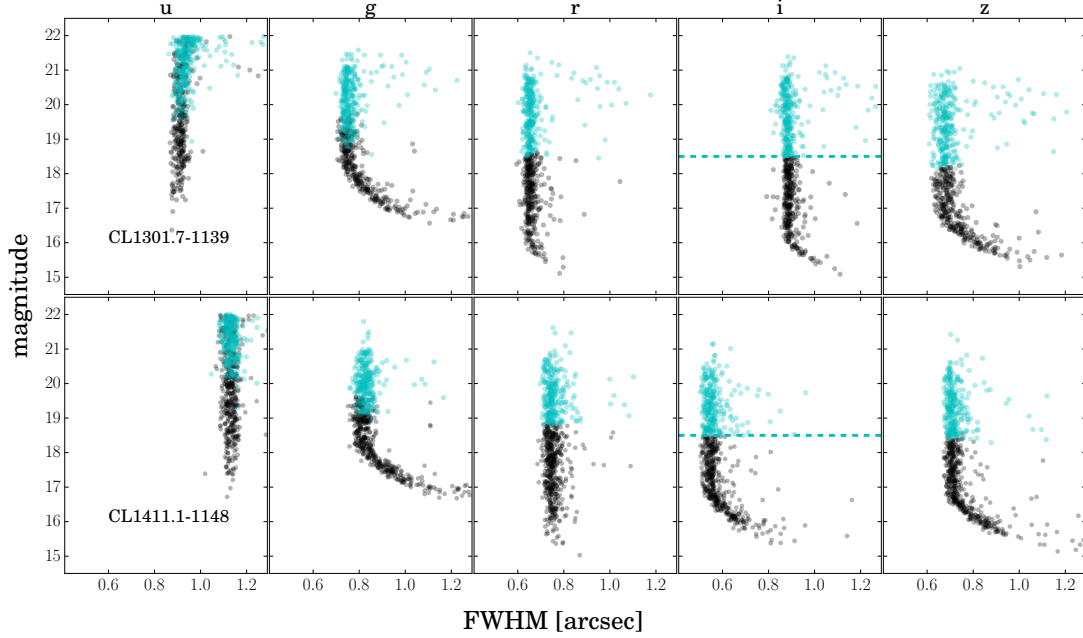


Figure 3.18 – This figures shows how we removed saturated sources. Each column corresponds to a band and the rows to each field. The magnitude cut is shown by the dashed line. Cyan dots are objects with magnitude above the cut, while black dots are below it. In each panel, the knee is where the saturation occurs. To avoid overloading the figure, 70 % of the sources have been randomly removed.

On the faint end, the *photo-z* quality decreases, as illustrated in Fig. 3.19. The outlier fraction and the accuracy σ_{NMAD} increases for fainter magnitudes. However the cuts in FWHM and *odds* removed already efficiently the outliers, so we do not apply any further cut. We should also keep in mind that the redshift range of interest for the clusters is $z \sim 0.4$ - 0.5 . In Fig. 3.20, showing the *photo-z* as a function of magnitude (with all the cuts described above), we see that very few galaxies with $i > 23$ are detected within this range. There are also no outliers (in red) in this region.

To sum up, we apply the following cuts: $i > 18$, $\text{odds} > 0.8$, $\text{FWHM} < 0.75''$ ($0.65''$) in r (i) for CL1301.7-1139 (CL1411.1-1148). The comparison between *photo-z* and z_{spec} before and after the cuts is shown in Fig. 3.21. The final median shift, NMAD and outlier fraction are $\text{median}(\Delta z) = 0.003$ (-0.008), $\sigma_{\text{NMAD}} = 0.036$ (0.037), $f_{\text{outliers}} = 2.3\%$ (2.5) for the CL1301.7-1139 (CL1411.1-1148) field.

The consequences of the *odds* cut are not straightforward to understand. We check its influence on the magnitude distributions (Fig. 3.22). Compared to the distribution without the

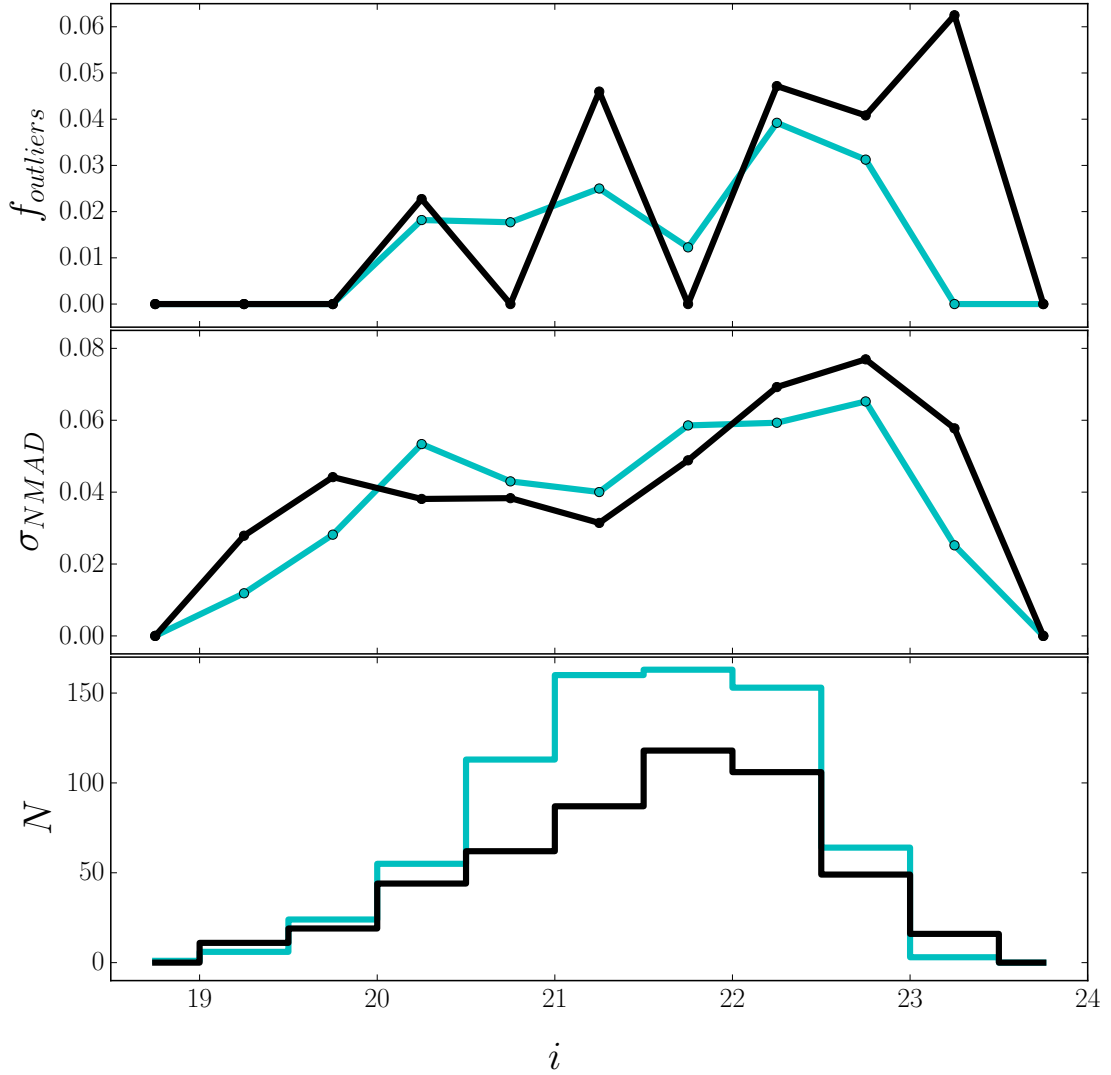


Figure 3.19 – Fraction of outliers (left), σ_{NMAD} (middle), number of galaxies with spectroscopic redshift (right) as a function of i -band magnitude in a 1" radius aperture (in bins of width 0.5). The sample contains only unsaturated ($i > 18$), resolved galaxy, with $\text{odds} > 0.8$.

cuts (Fig. 3.10), we see that the completeness (m_{90}) is strongly affected. In the detection band i , m_{90} decreases from 23.6 (23.3) to 22.6 (22.4) for CL1301.7-1139 (CL1411.1-1148).

3.2.5 *Photo-z* selected large scale structure members

The purpose of the *photo-z* is to identify the LSS around the clusters. To achieve this goal, we need to define for each cluster a *photo-z* interval likely to enclose the structures, while keeping a low foreground and background contamination. We take the $1\sigma_{\text{NMAD}}$ interval ($\delta z = z_{\text{cl}} \pm (1 + z_{\text{cl}})\sigma_{\text{NMAD}}$). This interval corresponds to a velocity much larger than the

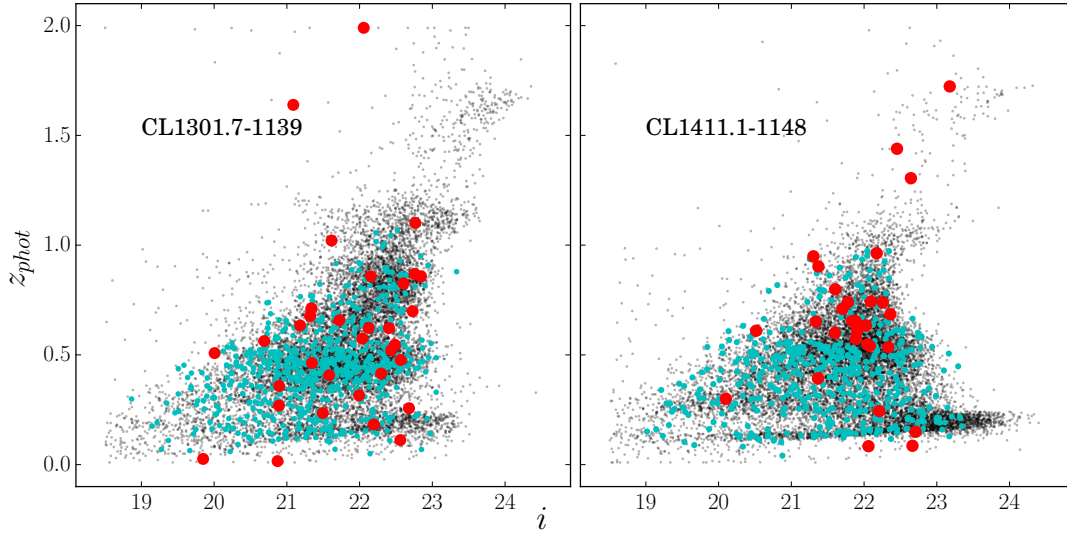


Figure 3.20 – $photo\text{-}z$ versus i -band magnitude. Black: all the galaxies with $photo\text{-}z$ and satisfying the previous cuts ($i > 18$, $odds > 0.8$, FWHM cut), cyan: galaxies with spectroscopic redshifts, red: outliers.

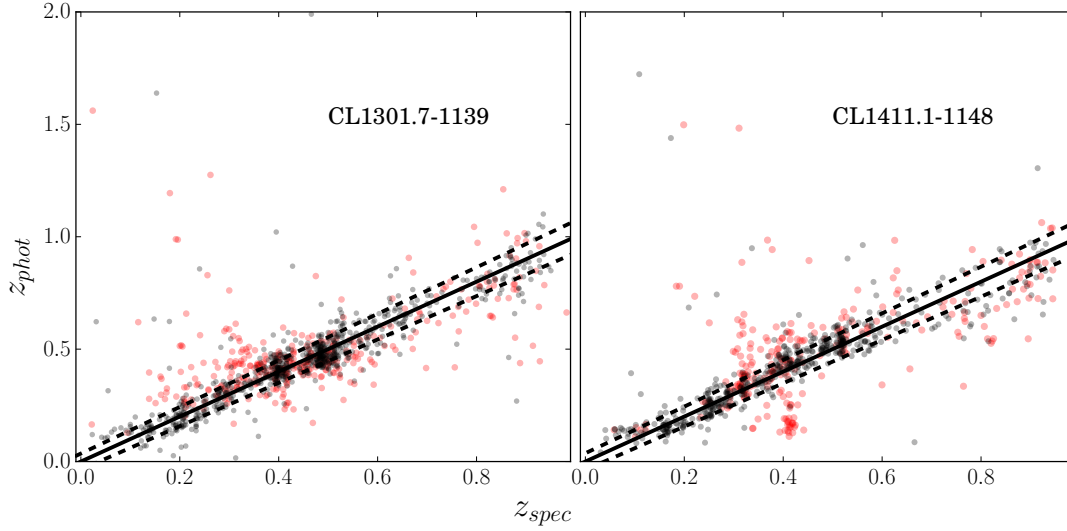


Figure 3.21 – z_{phot} against z_{spec} for both fields. Black: galaxies satisfying all the cuts of the final $photo\text{-}z$ sample, red: galaxies outside the cuts. The solid line shows the 1:1 relation, while the dashed lines correspond to $\pm(1 + z_{\text{spec}}) \cdot \sigma_{\text{NMAD}}$.

clusters velocity dispersions. We need to quantify the fraction of real cluster members that can be expected. It is estimated as $f_{\text{cl}}^{\delta z} = N_{\text{cl}}^{\delta z} / N^{\delta z}$, where $N_{\text{cl}}^{\delta z}$ is the number of spectroscopically confirmed cluster members in the $photo\text{-}z$ interval δz and $N^{\delta z}$ is total amount of galaxy with spectroscopy in the same $photo\text{-}z$ interval. The fraction of pollution is expected to be $f_{\text{pol}} = N_{\text{field}}^{\delta z} / N^{\delta z} = 1 - f_{\text{success}}$, with $N_{\text{field}}^{\delta z}$ the number of galaxies within δz which are not cluster

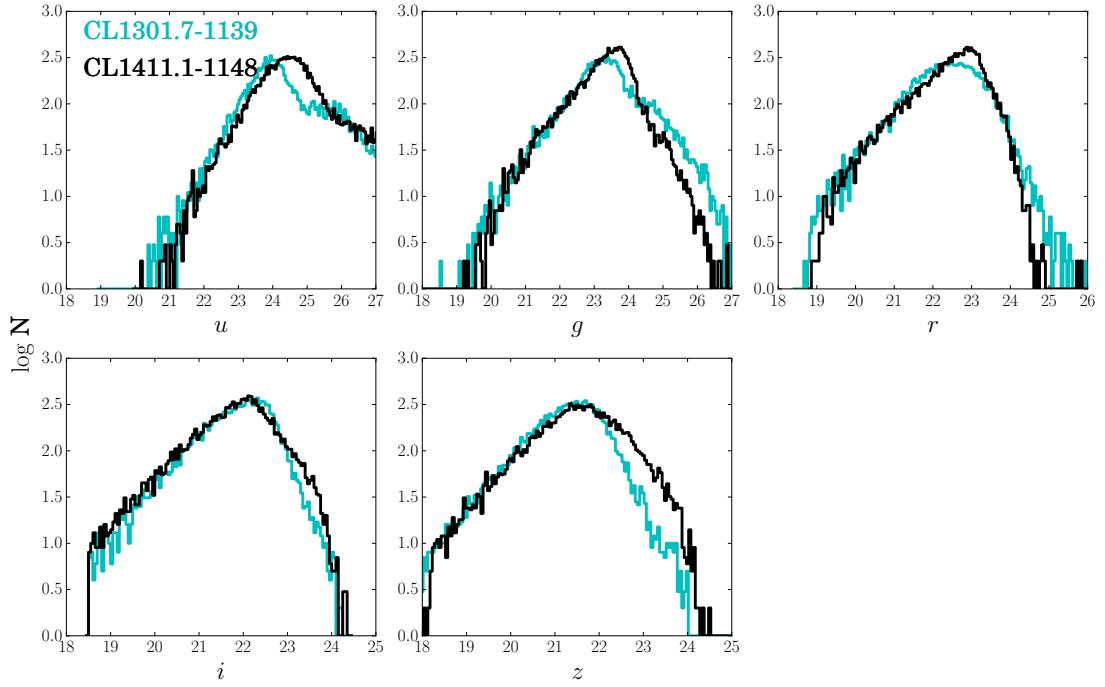


Figure 3.22 – Number counts for each band and field, for the final *photo-z* sample (to be compared with Fig. 3.10).

members and f_{success} the success rate. The fraction of detected/missed cluster members is also an important information. They are computed as $f_{\text{det}} = N_{\text{cl}}^{\delta z} / N_{\text{cl}}$ and $f_{\text{missed}} = N_{\text{cl}}^{\text{not } \delta z} / N_{\text{cl}} = 1 - f_{\text{det}}$, where N_{cl} is the total number of spectroscopically confirmed cluster members (at any z_{phot}). All these numbers are given in Table 3.2 and illustrated in Fig. 3.23. The δz interval is represented by the shaded area, the “missed” galaxies are in green ($N_{\text{cl}}^{\text{not } \delta z}$), the “pollution” is in blue ($N_{\text{field}}^{\delta z}$), the well identified cluster members are in red ($N_{\text{cl}}^{\delta z}$). We can see that our limits are conservative: $\sim 70\text{--}80\%$ of the real cluster members are selected with these limits. For the CL1301.7-1139 field, the success rate is of $\sim 45\%$. The main source of contamination comes from the cluster themselves: for each cluster, δz contains a significant fraction of members of the other cluster. Nevertheless, in each case, the peak of the distribution is still at the cluster redshift, so considering separately CL1301.7-1139a and CL1301.7-1139 is meaningful. For CL1411.1-1148, the success rate is $\sim 36\%$, which can seem low. The contamination essentially comes from a structure at $z=0.49$, which is too close the cluster redshift (0.52) to be efficiently distinguished with the *photo-z*. This is however not necessarily a problem, since two structures which are as close in redshift could be members of same LSS (this hypothesis will be studied in Section 5.5.1).

Chapter 3. Analysis methods

Table 3.2 – Different statistics to evaluate the quality of the cluster member selection.

cluster	δz	$N_{\text{cl}}^{\text{not } \delta z}$	$N_{\text{cl}}^{\delta z}$	$N_{\text{field}}^{\delta z}$	f_{missed}	f_{det}	f_{pol}	f_{success}
CL1301.7-1139a	0.35-0.45	33	82	98	0.29	0.71	0.54	0.46
CL1301.7-1139	0.43-0.54	24	103	124	0.19	0.81	0.55	0.45
CL1411.1-1148	0.46-0.57	12	44	78	0.21	0.79	0.64	0.36

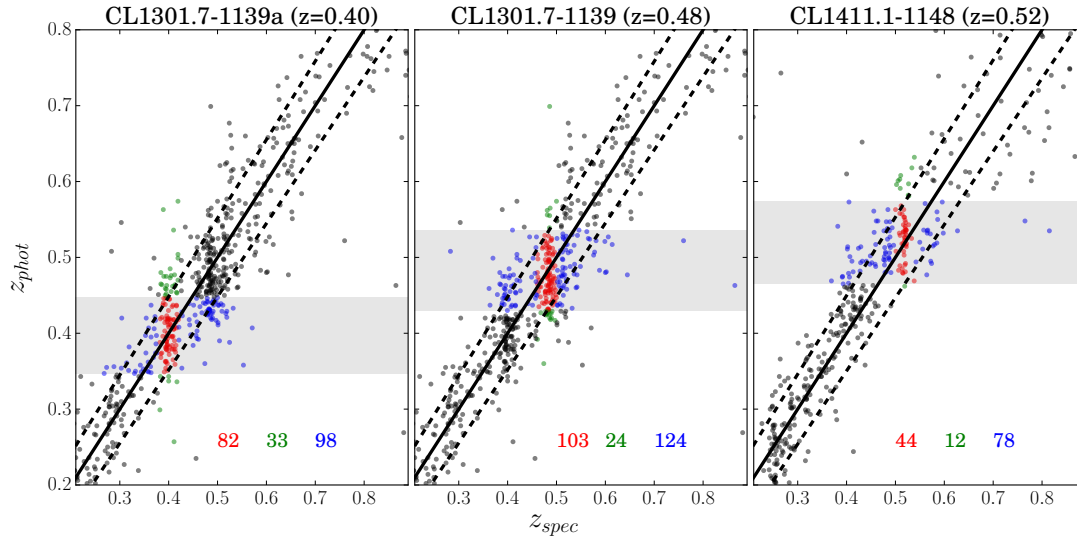


Figure 3.23 – This figure shows the *photo-z* selection of the cluster members. The shaded area are δz , the z_{phot} intervals used for the selection. Red: cluster members in δz , $N_{\text{cl}}^{\delta z}$, blue: field galaxies within δz , $N_{\text{field}}^{\delta z}$, green: cluster members outside of δz , $N_{\text{cl}}^{\text{not } \delta z}$, black: field galaxies outside δz . The solid line shows the 1:1 relation, while the dashed lines correspond to $\pm(1 + z_{\text{spec}}) \cdot \sigma_{\text{NMAD}}$.

3.3 Stellar masses

Stellar mass estimates add a crucial point to our analysis. We want to compare the stellar masses of the substructures around the central cluster and look for correlations with the environment. We choose to use FAST (Kriek et al. 2009), a recent code which is designed to be used in combination with EAZY. The photometry used is the same as the *photo-z* one. At this stage no zeropoint tuning was necessary as the FAST templates are not linked to the EAZY ones. The code works in a similar way than EAZY, except that instead of fitting the photometry using directly galaxy templates, the templates are modeled based on stellar population synthesis (SPS) models, an initial mass function (IMF), a star formation history (SFH), a reddening law and a parameter grid describing the stellar populations.

The SEDs are modeled with an exponentially declining SFH with $\log \tau$ between 8.5 and 10, a solar metallicity, a Chabrier IMF (Chabrier 2003), an age between 5 and 10 Gyr and a maximum extinction of 0.5. For consistency, stellar masses were computed at the galaxy photometric redshifts, even for the galaxies for which a spectroscopic redshift was available. These parameters are tuned to match what can be expected for galaxies at $z \sim 0.4-0.5$.

3.3.1 Stellar mass accuracy

Errors on the stellar mass are not only linked to the quality of the data. The IMF, SFH and reddening law, are subject to non-negligible systematics, which can dominate over the photometric and redshift uncertainties (De Lucia et al. 2014). We did not have a large and accurate stellar mass catalog for our data, so we have only chosen some standard parameters in FAST, without any fine-tuning. In any case, the absolute calibration is not crucial for us, we only want to compare the stellar masses between themselves in a homogeneous way. FAST provides errors (σ_M) on the stellar masses, using Monte-Carlo (MC) simulations to modify the photometry according to the magnitude errors. The *photo-z* errors are also taken into account (68 % confidence interval, based on the posterior distribution $P(z|\text{data}, R)$). We chose 10 MC simulations ($N_{\text{SIM}}=10$). This is high enough to have an estimation of the errors. We show the error σ_M as a function of the stellar mass in Fig. 3.24. As expected, lower stellar mass galaxies have a broader error distribution, as they are in general fainter (thus have larger photometric errors) than higher stellar mass galaxies. The median of σ_M (dashed line) is ~ 0.25 dex (corresponding to a factor $\lesssim 2$).

We also checked directly the influence of the redshifts errors on the stellar masses. Fig. 3.25 shows the difference in stellar mass (in dex) as a function of the difference in redshift. M_*^{phot} (M_*^{spec}) is the stellar mass, expressed in solar masses, when z_{phot} (z_{spec}) is used for the redshift estimation. Only the galaxies with $|\Delta z| < 0.15$ are shown. As can be expected, we can see that in general the error in stellar mass increases with $|\Delta z|$. However, the standard deviation of this error is ~ 0.1 dex, significantly below σ_M . This justifies to compute the stellar masses at the galaxy photometric redshifts, even for the galaxies for which a spectroscopic redshift was available.

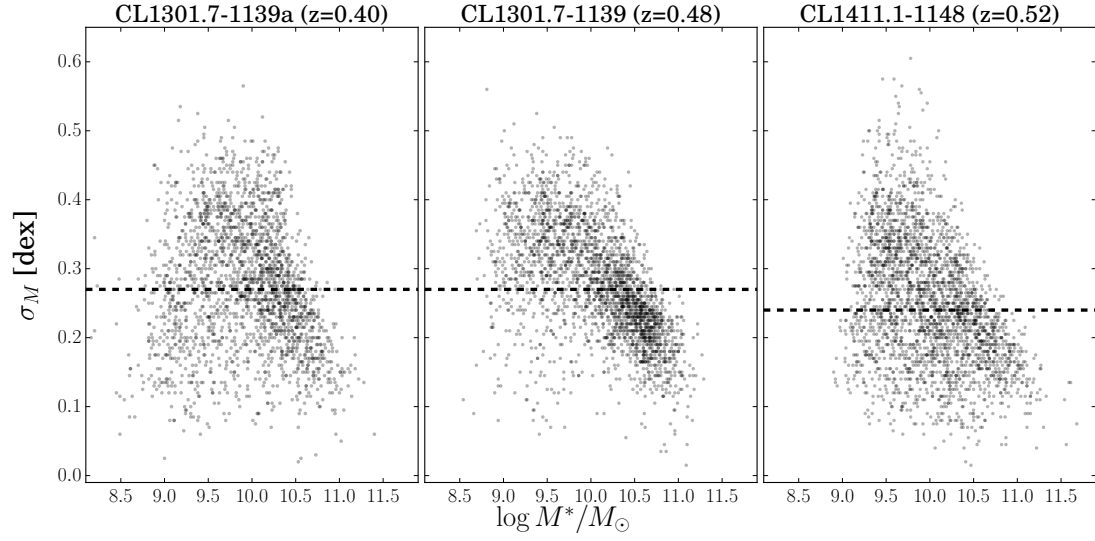


Figure 3.24 – Error in stellar mass as a function of stellar mass. The dashed line is the median of the error.

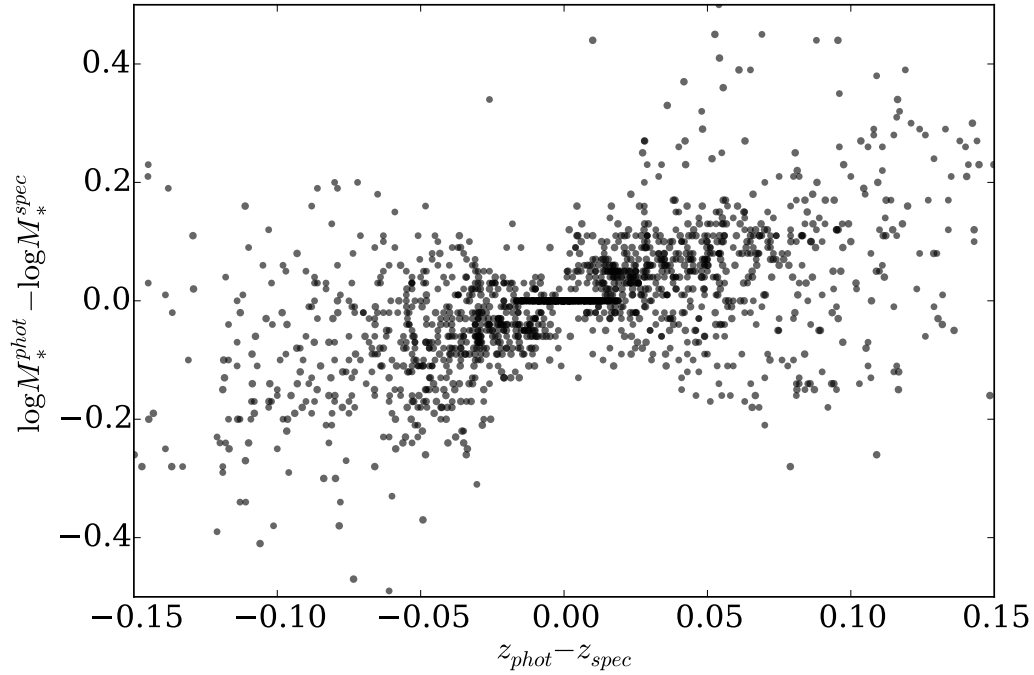


Figure 3.25 – Stellar mass difference (in log) as a function of the difference in redshift. M_*^{phot} (M_*^{spec}) is the stellar mass, expressed in solar masses, when z_{phot} (z_{spec}) is used for the redshift estimation.

3.3.2 Stellar mass completeness

The (apparent) magnitude completeness limit m_{90} corresponds to an increasing stellar mass completeness limit with redshift. At a given redshift, m_{90} can be translated to a luminosity limit L_{90} , but the corresponding stellar mass limit $M_{\star,\text{lim}}$ depends on the stellar mass to light ratio M/L distribution at L_{90} . In principle, $M_{\star,\text{lim}}$ should be the maximum stellar mass detected at m_{90} . Indeed for any lower stellar mass M , a galaxy of stellar mass M with a similar M/L could exist¹⁰, thus having a luminosity below L_{90} and remaining undetected. This estimation of the completeness has however two flaws. First, the maximum stellar mass at m_{90} is by definition strongly dependent on extreme value and outliers. It will fluctuate significantly for even small variations of m_{90} . Second, the highest stellar mass galaxies will not necessarily be seen near m_{90} , because they are in general redder, thus may not be detected in the bluer bands and therefore could have a wrong redshift. For these reasons, we preferred another approach.

One possibility is to use a deeper dataset and to scale the stellar mass and fluxes of galaxies below the detection limit to the detection limit (Marchesini et al. 2009). The stellar mass completeness can be taken as the stellar mass enclosing all (or e.g. 95 %) of the scaled stellar masses. More precisely, here are the different steps:

1. Choose a narrow redshift interval.
2. Choose a magnitude interval $[m_{\text{low}}, m_{\text{high}}]$ in the deep dataset above the magnitude limit of the original dataset, i.e. $m_{\text{low}}, m_{\text{high}} > m_{\text{lim}}$ (in the same filter).
3. For each galaxy of magnitude m_i in the magnitude interval, compute the flux ratio $r_i = 10^{-0.4 \cdot (m_{\text{lim}} - m_i)}$. For a narrow redshift interval, this flux ratio is similar to the luminosity ratio.
4. Scale the stellar masses of the galaxies in the interval by the flux ratio: $M_{\star,i}^{\text{scaled}} = M_{\star,i} \cdot r_i$.
5. The 95 % stellar mass completeness, $M_{\star,95}$, can then be taken as the stellar mass above 95 % of the scaled stellar masses $M_{\star,i}^{\text{scaled}}$.

This empirical method is valid as long as the high end of the M/L distribution of the galaxies selected for the scaling is close to the one at the detection limit.

When a deeper dataset is not available to do this stellar mass up-scaling, as in our case, Quadri et al. (2012) applied the same method, but with a stellar mass down-scaling: they selected the galaxies above the detection limit and scaled them down (in stellar mass and flux) to the detection limit. This is the method we chose. In Fig. 3.26, we show the stellar mass distribution of the LSS samples for each cluster (black). The magnitude interval chosen for the scaling is $21.5 < i < 22$ (the shaded area of Fig. 3.27). The stellar masses of the galaxies

¹⁰This is not strictly true, since low luminosity galaxies tend to have lower M/L than bright galaxies (Marchesini et al. 2009). Nevertheless, there is no abrupt transition between the two regime, so the argument remains valid.

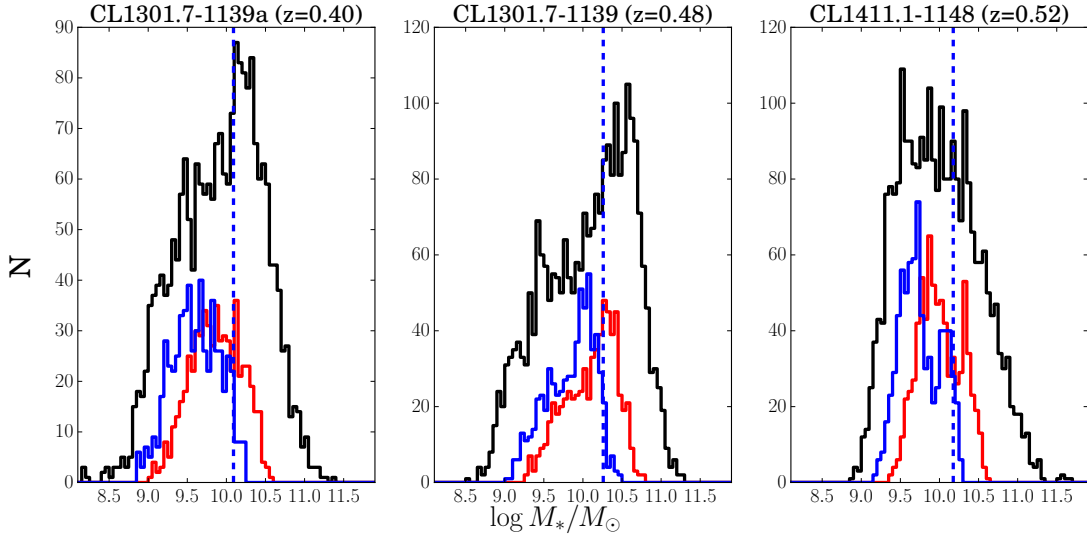


Figure 3.26 – Illustration of the procedure to compute the stellar mass completeness. Black: distribution of the stellar masses at the cluster redshifts, red: galaxies with $22 < i < 23$, blue: scaled stellar masses. The dashed line represents the 95 % completeness stellar mass limit.

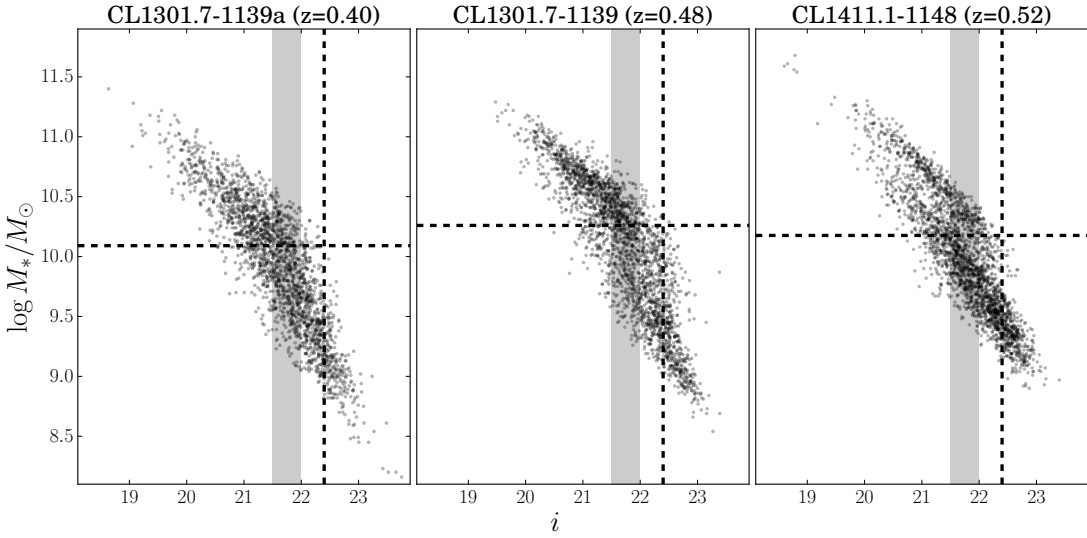


Figure 3.27 – Stellar mass against i -band magnitude for the *photo-z* selected cluster members. The shaded area is the magnitude interval chosen for the scaling, the dashed vertical line is the magnitude completeness limit $m_{\text{lim}} = 22.4$ and the dashed horizontal line is the stellar mass completeness.

within this magnitude interval is the red curve in Fig. 3.26, while the scaled stellar masses are in blue. $m_{\text{lim}} = 22.4$ (dashed vertical line in Fig. 3.27) is taken from the final *photo-z* sample (see Fig. 3.22). This yields the following 95 % stellar mass completeness: 10.1, 10.3 and 10.2 $\log(M_*/M_\odot)$ for CL1301.7-1139a, CL1301.7-1139 and CL1411.1-1148, respectively (horizontal dashed lines in Fig. 3.27 and vertical dashed lines in Fig. 3.26).

3.4 Environment measurement

The notion of environment for galaxies is rather abstract. Galaxy properties depend on many different types of “environments”: the intergalactic medium, the galaxy (close) neighbors, the dark matter halo, the position in the LSS, etc. For our data, the most direct tracer of environment is to use the spatial distribution of galaxies. We want to look for correlations between the number density of galaxies and their properties. We are interested in the influence of groups, filaments and clusters, meaning the density should be sensitive to scales typically ranging from 0.2 to 2 Mpc.

Ideally, we could use the 3D distribution (e.g., in the space α, δ, z) of the galaxies to try to find 3D overdensities in our fields. However, the accuracy of the positions on the sky is orders of magnitude higher than in depth ($\sigma_{\alpha, \delta} \ll \sigma_z$), which will artificially elongate the shape of the overdensities along the line of sight. We choose instead to use a tomographic approach, i.e. to select galaxies within a given redshift interval and then compute the 2D projected density.

There are essentially two kinds of such density measurement: fixed or adaptive apertures densities. The principle of fixed apertures is to choose an aperture size, count the galaxies in this aperture (at any coordinate in the field) and compute the ratio between the number of galaxies and the surface area of the aperture. Adaptive aperture measurements are more numerous (and usually more complicated). One example is the “nearest-neighbor” approach, where the aperture is defined as the distance $r_N(x, y)$ from any point (x, y) of the field to the N^{th} nearest galaxy neighbor. The density $\Sigma_N(x, y)$ is then the ratio between N (fixed) and the surface defined by the adaptive distance: $\Sigma_N(x, y) = \frac{N}{\pi r_N^2(x, y)}$ (hereafter we will not write anymore the (x, y) dependence, to simplify the notation).

Both have their pros and cons. Fixed apertures are in a sense more physical: it is possible to choose an aperture corresponding to e.g. a typical group size at the considered redshift and they will be detected in an optimal way. The problem is that smaller overdensities will be smoothed and tend to disappear. On the other hand, a too small aperture will yield very noisy densities (if you have only a few galaxies within an aperture, the error on the density will be large) and miss large scale variations. One advantages of the nearest neighbor approach is that the (purely statistical) error on the density will be the same everywhere, since the number of galaxies used to compute it is constant. However, similarly to the previous case, if the number of neighbors is too small, the density field looks noisy and if it is too large, the small structures are smoothed out.

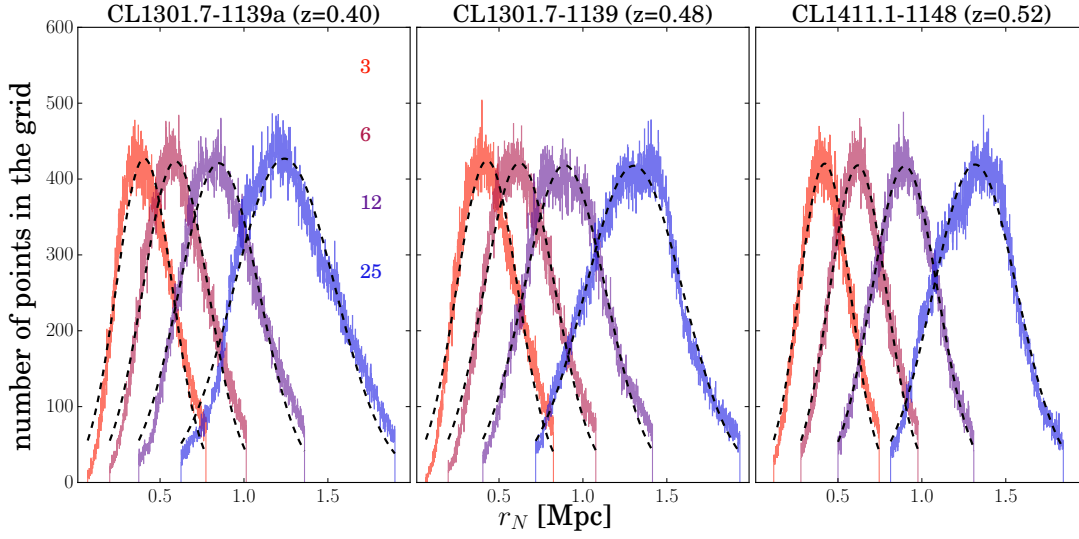


Figure 3.28 – Distribution of the distance to N^{th} nearest neighbor, r_N , computed at each point of a 500x500 grid, for different values of N . The distribution are truncated at 3 MAD around the median. The black dashed lines are Gaussian fits, whose mean and width are reported in Fig. 3.29 as a function of N .

In our case, we are more interested in probing a large range of dynamical scales at once, rather than focusing on a specific density value. This is why we chose the nearest neighbor approach. To select which N is most adapted to our data, we compute the distribution of r_N for different values of N (Fig. 3.28), fit a Gaussian function on each distribution and report the mean and

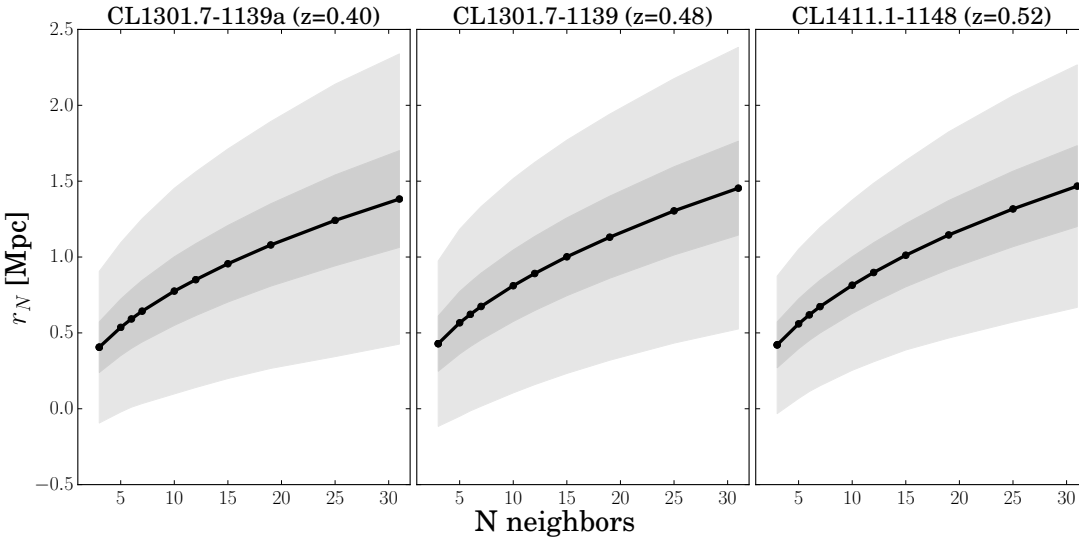


Figure 3.29 – Mean of the r_N distributions of Fig. 3.28, as a function of the the number of neighbors N . The shaded areas correspond to 1 and 3 σ of the Gaussian fit.

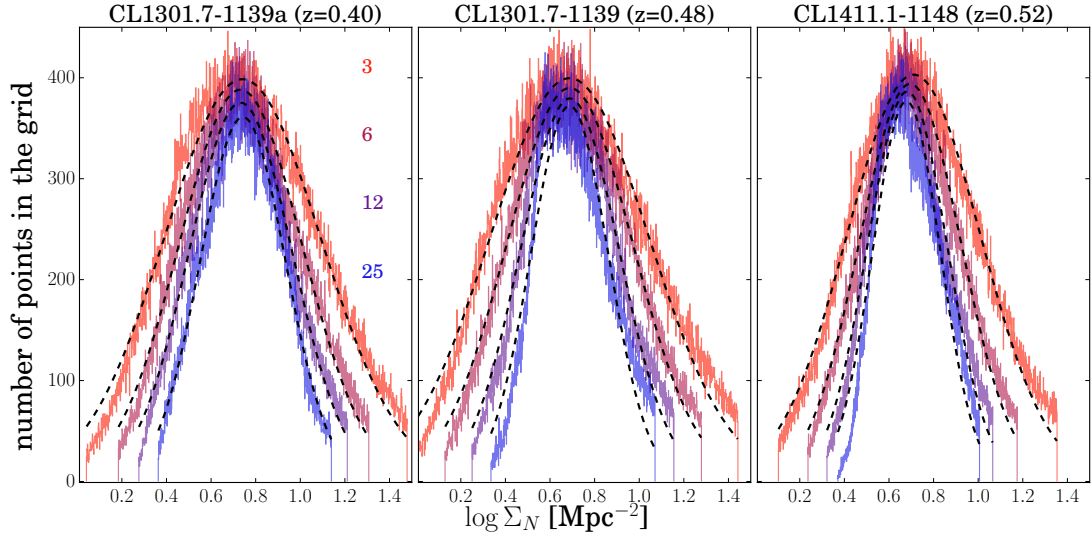


Figure 3.30 – Distribution of the density Σ_N as a function of the number nearest neighbor N . The distributions are truncated at 3 MAD around the median. The black dashed lines are Gaussian fits, whose mean and width are reported in Fig. 3.31 as a function of N . Similar to Fig. 3.28, with Σ_N instead of r_N .

the σ of the Gaussian as a function of N (Fig. 3.29). The average value of r_N and its dispersion increases with N . Given that the virial radii of our clusters are between 0.75 and 1.3 Mpc

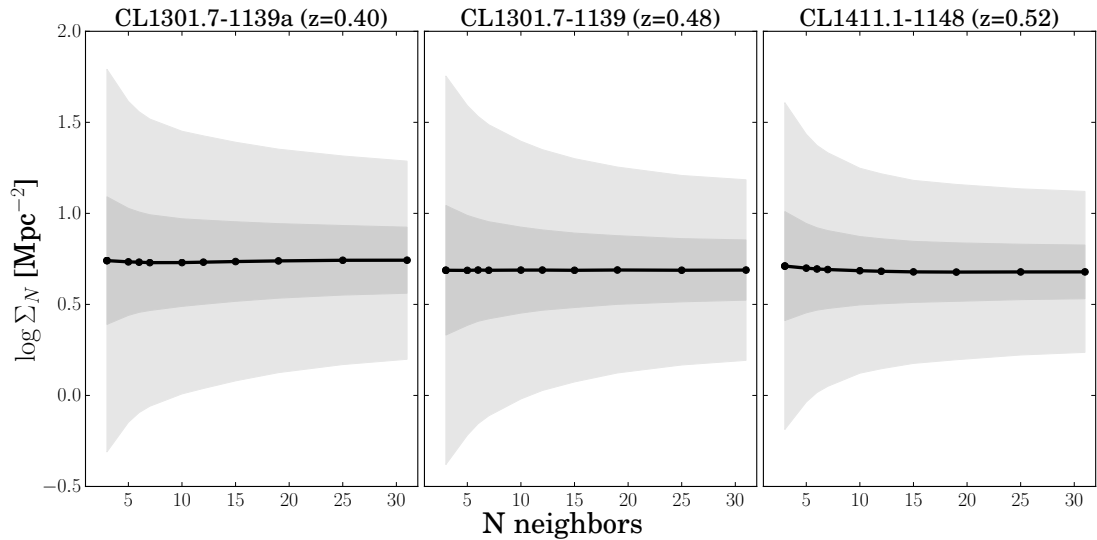


Figure 3.31 – Mean of the Σ_N distributions of Fig. 3.30, as a function of the number of neighbors N . The shaded areas correspond to 1 and 3 σ of the Gaussian fit. Similar to Fig. 3.29, with Σ_N instead of r_N .

(Table 2.1), a value of $N = 10$ seems adapted¹¹. It corresponds to an average scale of about 0.8 Mpc and 90 % of the values are below ~ 1.5 Mpc. It is a bit too high, since this is comparable to the cluster scales, which are supposed to have extreme values in the density field. However, lower values of N will start to be strongly affected by Poisson noise¹², so we chose not to decrease N . In what follows, we will consider Σ_{10} as a *local* density measure.

The average value of the density distribution is only weakly dependent on N (Fig. 3.30 and 3.31). On the other hand, the scatter increases with lower N . This is not surprising, as increasing N is equivalent to smoothing the density field.

¹¹We use the angular diameter distance to compute r_N and R_{200} .

¹²I have actually made the tests, and indeed most of the correlations with density weakened for a lower number of neighbors.

4 Results

In the previous chapter, we have described how to identify galaxies close to the cluster redshift, how to compute their mass and how to measure their density. In this chapter, I will explain how to use these measurements to identify and characterize the large scale structures surrounding the clusters.

4.1 Large scale structures detection

The identification of the large scale structures is achieved by looking for high density regions in the density maps of the galaxies close to the cluster redshift (the samples are defined in Section 3.2.5). Both local (Σ_{10}) and global (Σ_{30}) density measurements are presented (Fig. 4.1, 4.2 and 4.3), to differentiate small and large scale variations in the density field. Each figure corresponds to a cluster, the top (bottom) panel is for Σ_{10} (Σ_{30}). The light black dots are the galaxies in the *photo-z* selected LSS samples. We chose empirical density thresholds (thin black contours) to separate the density field between the field, filaments and groups/clusters. These thresholds are set at 0.95 and 1.4 for $\log \Sigma_{10}$ and 0.8 and 1.1 for $\log \Sigma_{30}$. They correspond to about 1 and 3σ above the mean of the $\log \Sigma_N$ distributions. The blue solid circle is the cluster virial radius (R_{200}) and the dashed one is $5R_{200}$.

A striking feature of the maps is the inhomogeneity of the density fields. At distances from the cluster center larger than $\sim 1 - 2R_{200}$, the circular symmetry is broken and the overdensities tend to grow along preferred directions. The structures reach the edges of the MegaCam FoV. We can speculate they keep extending outside the FoV, possibly out to another cluster. It shows that studying cluster properties as a function of the cluster-centric distance can be heavily biased, mixing galaxy populations residing in very different environments. This is confirmed when we compute the density as a function of the cluster-centric distance (Fig. 4.4). We see that at a given cluster-centric distance, the local density may span a broad range of values.

The maps of the CL1301.7-1139 field have similarities, because there is an overlap in the *photo-z* intervals used to compute the densities around CL1301.7-1139a and CL1301.7-1139 (see

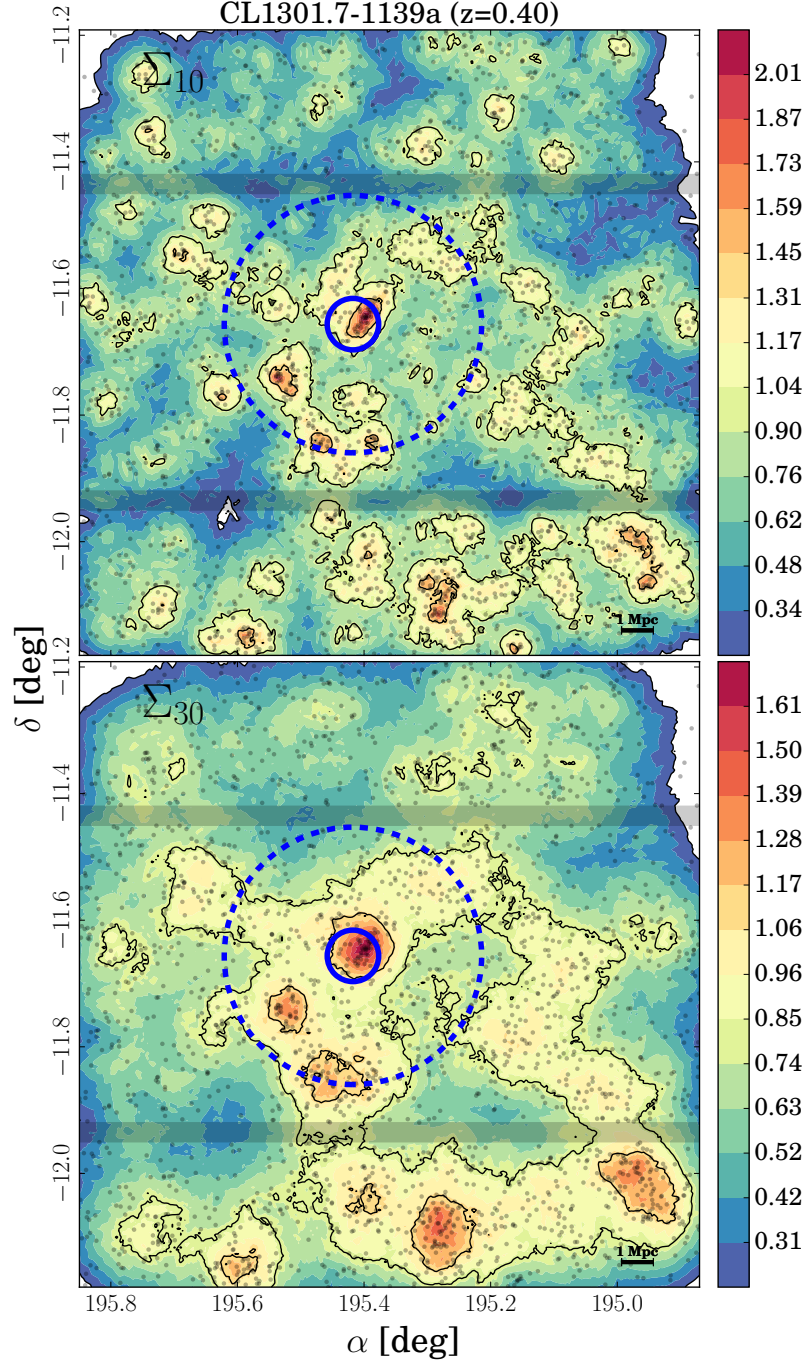


Figure 4.1 – Density maps of the *photo-z* selected large scale structures members around CL1301.7-1139a. The light black dots are the galaxies, while the color code represents $\log \Sigma_N$. The top row is for $N=10$ and the bottom one for $N=30$. The grey horizontal bands show the MegaCam large CCD gaps. In this map, the density is computed also near the gaps and the edge of the FoV (where it is underestimated), to give the reader a better insight of the global density field. The white regions are where $\log \Sigma_N < 0.2$. The thin black contours separate the density field between the field, filaments and groups/clusters. The blue solid circle is the cluster virial radius (R_{200}) and the dashed one is $5R_{200}$. The North is at the top of the figure and the East at the left.

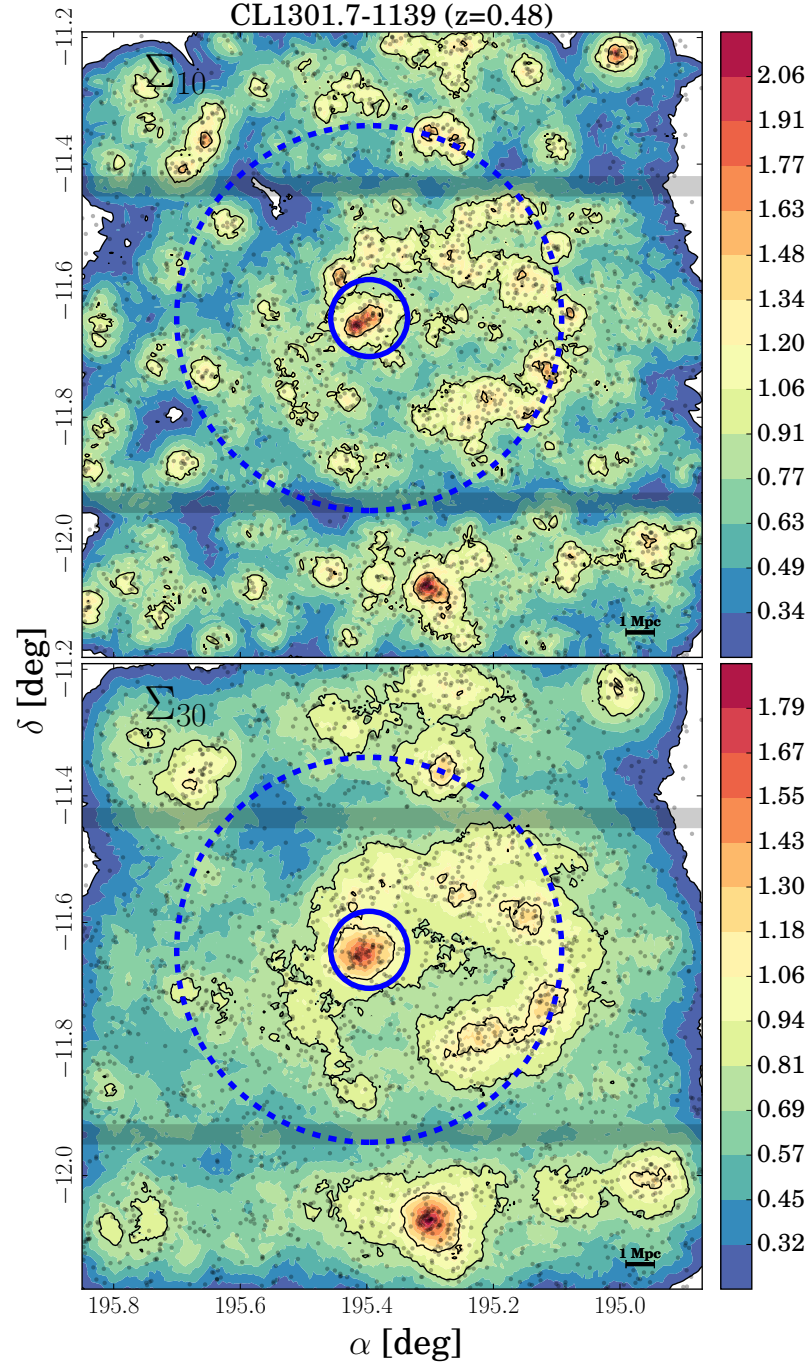


Figure 4.2 – Same as Fig. 4.1, but with CL1301.7-1139 instead of CL1301.7-1139a.

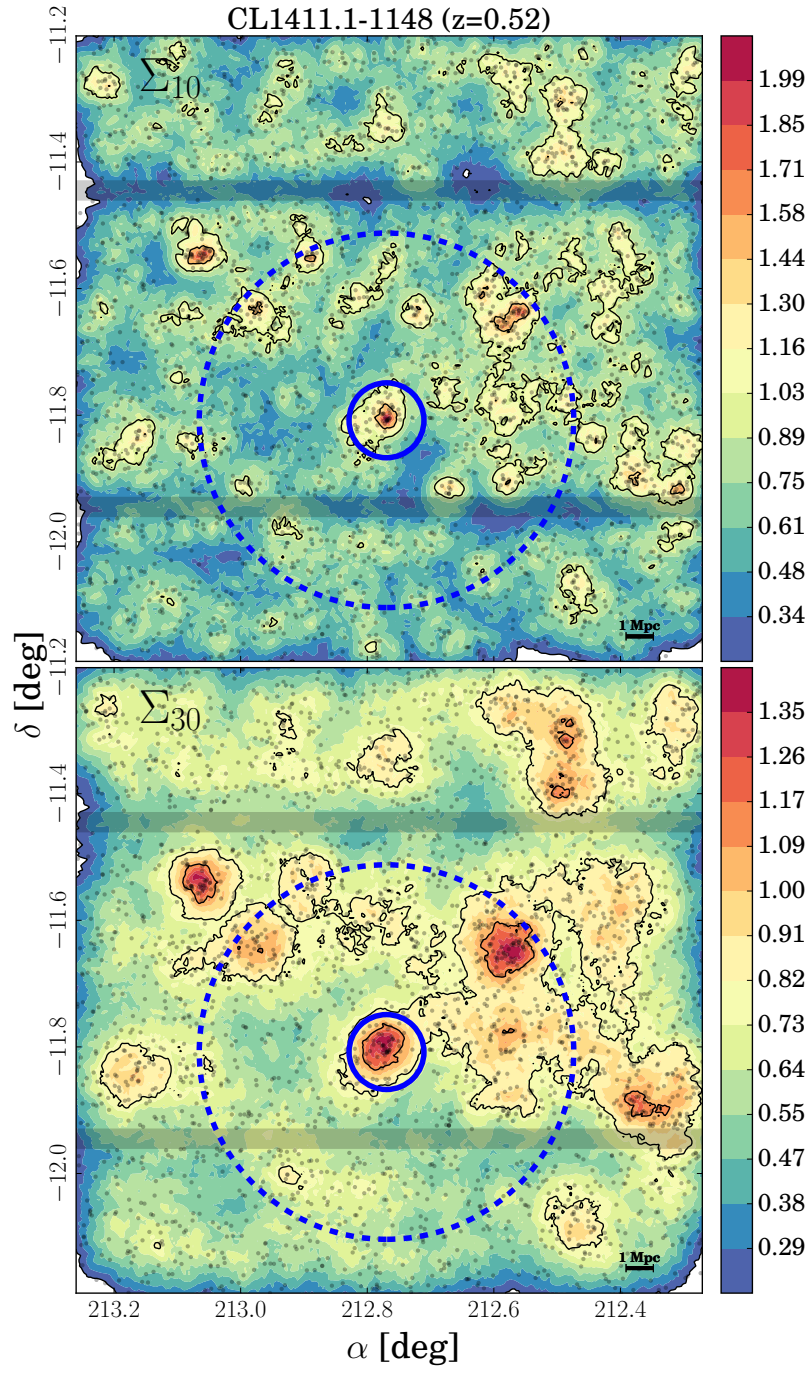


Figure 4.3 – Same as Fig. 4.1, but with CL1411.1-1148 instead of CL1301.7-1139a.

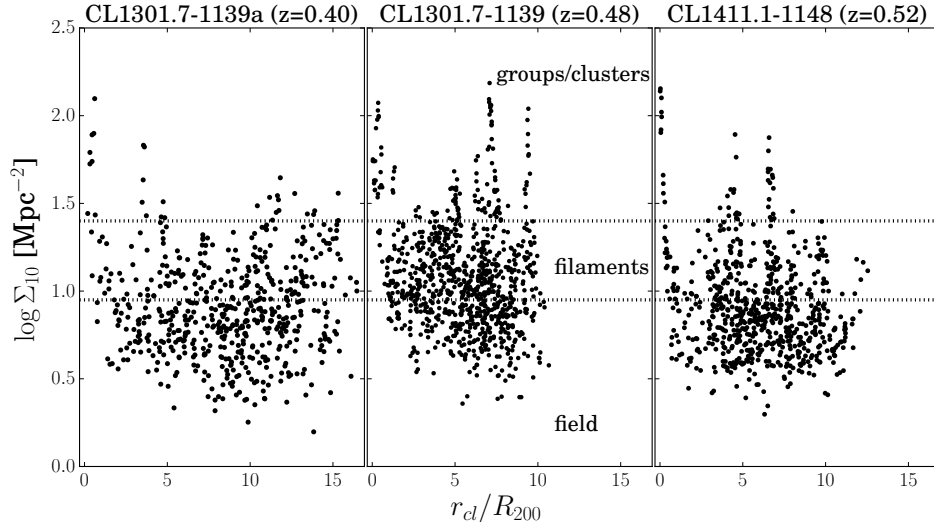


Figure 4.4 – Local density as a function of the cluster-centric distance, for each one of the LSS samples. The dotted lines are the thresholds separating the density field between the field, filaments and groups/clusters.

Fig. 3.23). Nevertheless, the strongest overdensities (especially on the local density maps) are located at different positions, which means that the two clusters can still be analyzed separately. In all the maps, the strongest densities are located on the cluster. It is a proof that the maps are reliable.

In what follows, we describe the most prominent features in each density map.

- CL1301.7-1139a: There is a filament, made of several substructures, extending from the cluster to the strong overdensity in the South¹. This overdensity is also connected to a smaller structure at the South-West, from which another filament points towards the cluster.
- CL1301.7-1139: The cluster is at the center of a spiral structure, possibly extending to the North. The two overdensities in the South are still present, but do not seem to be connected to the cluster with a filament (CL1301.7-1139a). They could be polluted by members of CL1301.7-1139a.
- CL1411.1-1148: A filament extends westward from the cluster and splits between the West and the North (assuming that there is no real discontinuity at the northern Mega-Cam gap). There is also a strong overdensity to the North-East, however there is no obvious filament connecting it to the cluster.

¹The North is at the top of the figure and the East at the left.

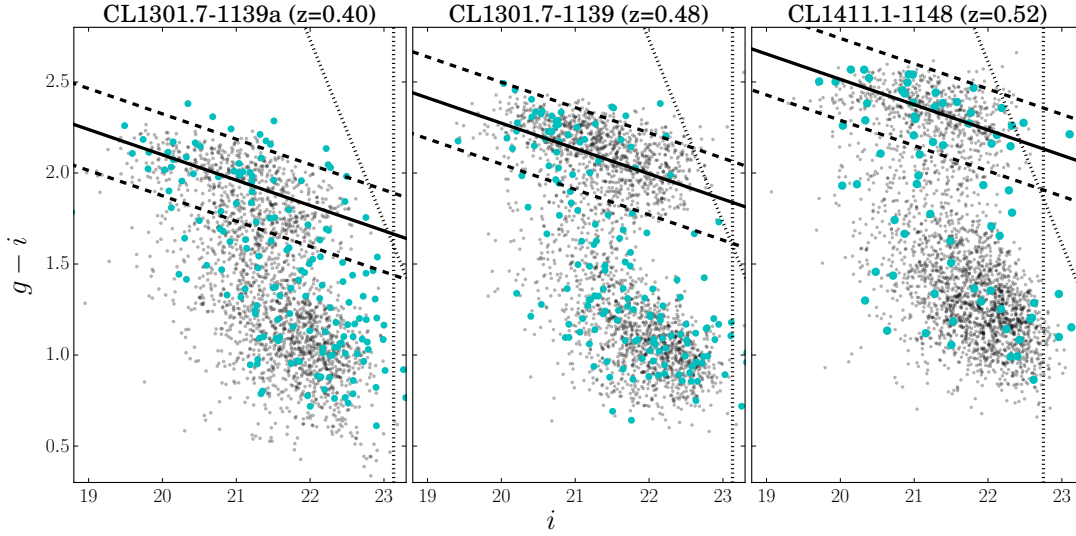


Figure 4.5 – Color-magnitude diagram $g - i$ versus i (1" radius apertures). The solid black line is a fit to the cluster red sequence, with the 3σ scatter delimited by the dashed lines. The dotted lines show the magnitude limits in g and i . The cyan dots are the spectroscopic members (from LDP and FORS2).

4.2 Red sequence

At a fixed redshift, quenched galaxies are usually located in a narrow sequence in a color-magnitude diagram (e.g., De Lucia et al. 2004). Galaxies can be classified depending on whether they belong to this red sequence or not. This criterion is not perfect to distinguish between passive and active galaxies, since e.g. star-forming galaxies can have red optical colors due to dust extinction, but it is still a useful separation that has been largely used in the literature. It is also very simple to apply, since the red sequence can be defined directly with the photometry at hand.

The red sequence of our clusters is computed in the following way: we apply the red sequence definition in $V - I$ versus I from De Lucia et al. (2004) to the FORS2 cluster members. Then the red sequence members are identified in $g - i$ versus i and a linear fit is determined for all the clusters simultaneously. The slope is common to all the clusters, while the elevation depends on each cluster. De Lucia et al. (2004) determined a 3σ width of 0.6 for the red sequence. We convert $V - I$ to $(g - i)_{\text{SDSS}}$ with the relations from Jester et al. (2005) and then from $(g - i)_{\text{SDSS}}$ to $(g - i)_{\text{MegaCam}}$ with the MegaPipe website², yielding a width of 0.45 in $g - i$. The color-magnitude diagram $g - i$ versus i is presented on Fig. 4.5. The black dots are the galaxies in the LSS samples, while the cyan ones are the spectroscopically confirmed members. The solid black line is the red sequence and the dashed lines delimit its width. We see it matches very well both in position and extend the distribution of the red galaxies.

² <http://www2.cadc-ccda.hia-ihp.nrc-cnrc.gc.ca/en/megapipe/docs/filt.html>

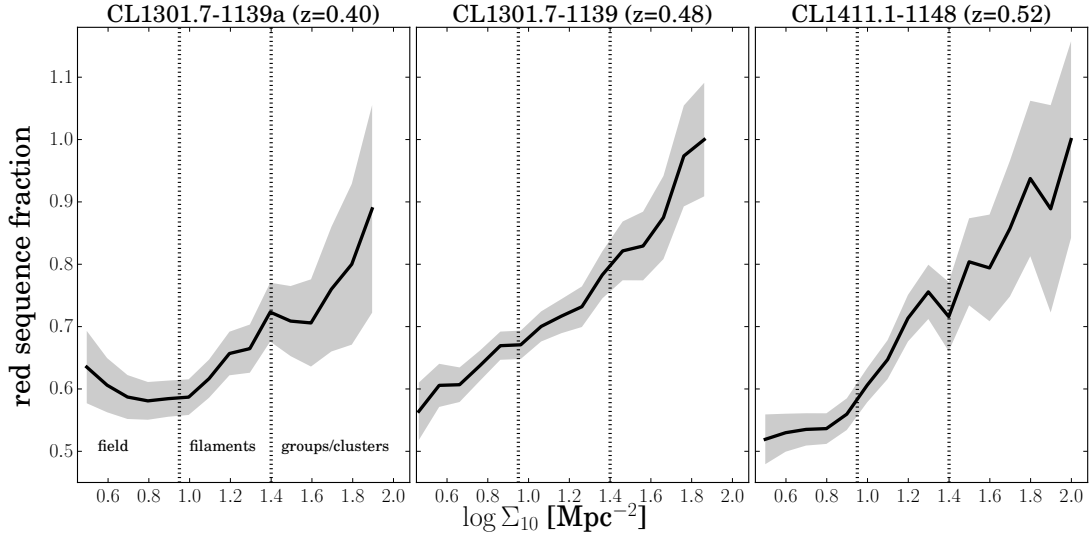


Figure 4.6 – Fraction of galaxies on the red sequence as a function of local density, for galaxies close to the cluster redshift. The bins are defined by steps of 0.1 dex and have a width of 0.4 dex (thus they partially overlap). The dotted lines are the thresholds separating the density field between the field, filaments and groups/clusters.

4.3 Influence of the environment

4.3.1 Red sequence galaxies and their environment

Fig. 4.6 shows the fraction of galaxies on the red sequence as a function of the local density (Σ_{10}). Unlike in the density maps, where the density is computed over a grid, the densities of the galaxies is computed exactly where they are located. Galaxies close from the edge of the FoV and from the MegaCam large gaps are rejected. The dotted lines are the thresholds separating the density field between the field, filaments and groups/clusters. Globally, we see a strong increase of the red sequence fraction with density. This correlation has already been observed by numerous studies (see Section 4.4), and can be interpreted as a sign of environmental quenching at all scales. In the field environment however, the slope of the trend seems less steep.

The errors on the red sequence fraction are computed with a binomial distribution. Defining the probability of a galaxy to be in the red sequence by $p_r = N_r/N$, with N_r the number of galaxies on the red sequence and N the total amount of (*photo-z* selected) galaxies, the errors in a given density range containing n galaxies is $p(1-p)/\sqrt{n}$.

4.3.2 The stellar mass contribution

Stellar mass correlates strongly with galaxy colors (Fig. 4.7). Red galaxies are in general more massive than blue ones. In Fig. 4.8 we show the $g-i$ colors of galaxies as a function of local

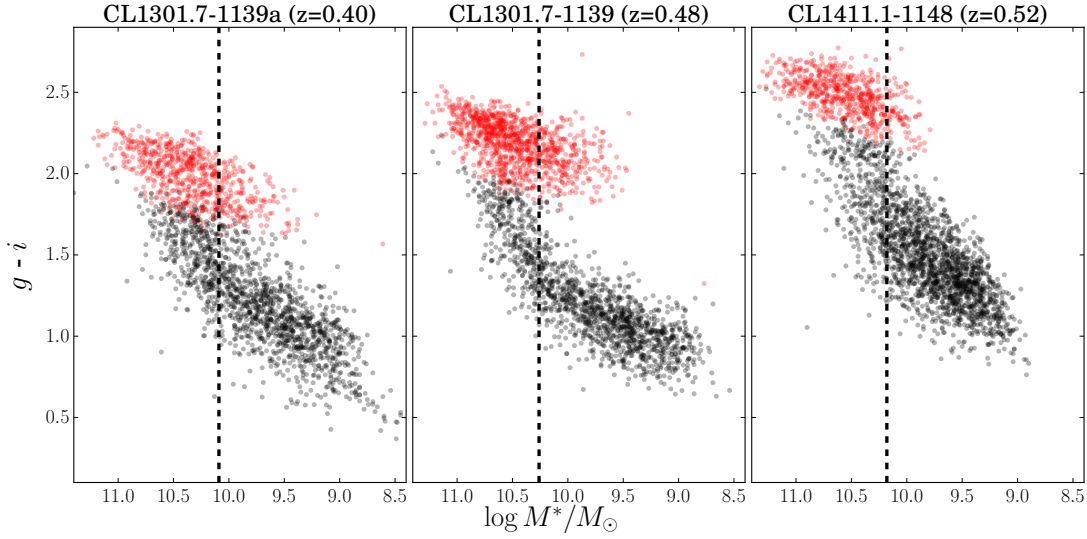


Figure 4.7 – $g-i$ colors as a function of stellar mass, for each LSS sample. The vertical lines are the mass completeness limits. Red dots are the red sequence members.

density, in different stellar mass ranges. To avoid any color bias, these ranges are chosen to be above the stellar mass completeness limit at the redshift of the clusters (see Section 3.3.2), but the density field is still computed from the full LSS sample. As we can see, the influence of the density is visible at all stellar masses. There is a clear lack of blue galaxies at the highest densities.

More precisely, if we compute the fraction of red sequence galaxies as a function of the density for each stellar mass interval of Fig. 4.7, we see (Fig. 4.9) a positive correlation for all the stellar mass ranges considered. There is also evidence that the slope of the relation decreases with stellar mass. This is not surprising, as more massive galaxies are in general already red (Fig. 4.7), thus are less easily further quenched by the environment. The relations are less clear for CL1301.7-1139a. It can be related to the fact that this cluster is less massive than the others, hence environmental effects should be weaker. This explains as well that the maximum density reached is not as high as for the other clusters. It is also possible that this cluster is more polluted by background galaxies, since the observations were designed to reach $z \sim 0.5$.

In Fig. 4.11 and 4.10, we study the relation between color and stellar mass in different environments: field, filaments and groups/clusters. Fig. 4.11 shows the color versus stellar mass relation in each environment. As expected from Fig. 4.7 massive galaxies are redder in general. If we show the fraction of red sequence galaxies as a function of stellar mass in each environment (Fig. 4.10), we see that denser environments tend to have redder galaxies, at any stellar mass. These figures confirm that even at the filament scale, the red fraction of galaxies is higher than in the field. It means that before galaxies reach the cluster (at $\sim R_{200}$), they already suffered significant quenching from pre-processing effects within the filaments.

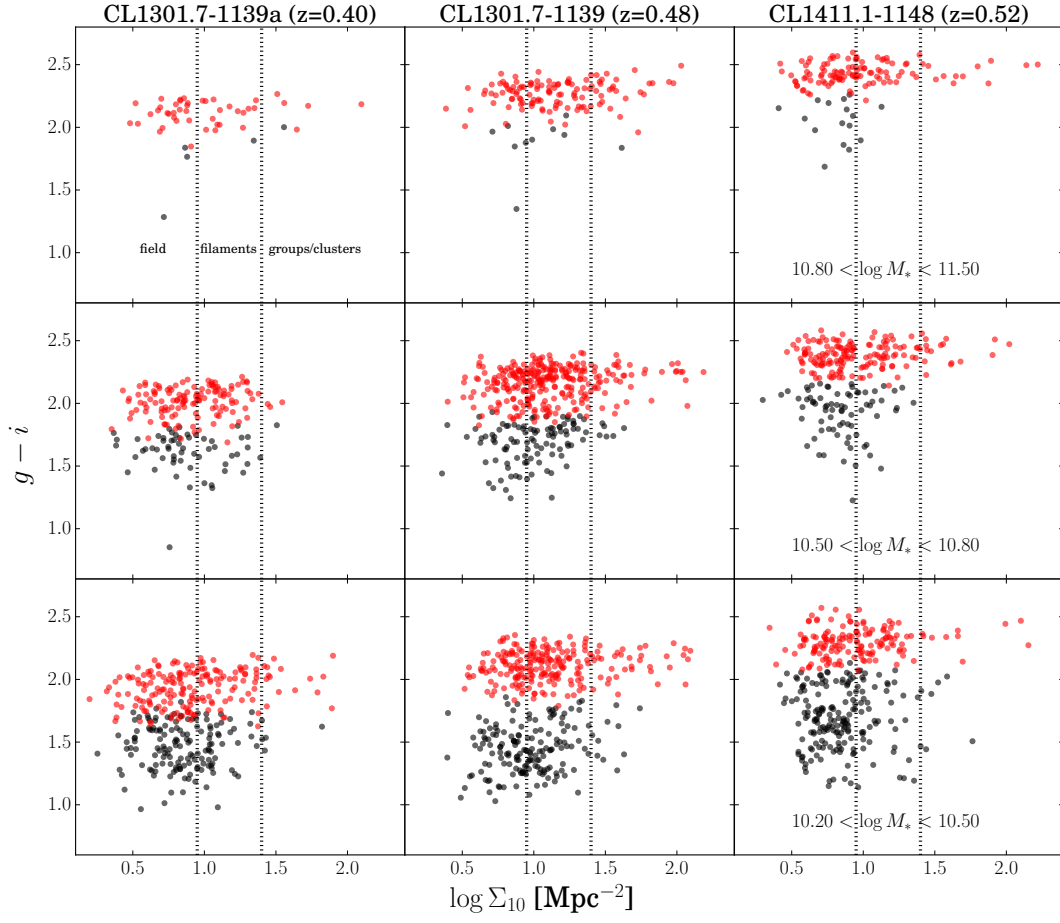


Figure 4.8 – $g-i$ colors as a function of the local density. The panels correspond to different clusters (columns) and stellar mass intervals (rows). The dotted lines are the thresholds separating the density field between the field, filaments and groups/clusters. M_* is expressed in solar mass units. Red dots are the red sequence members.

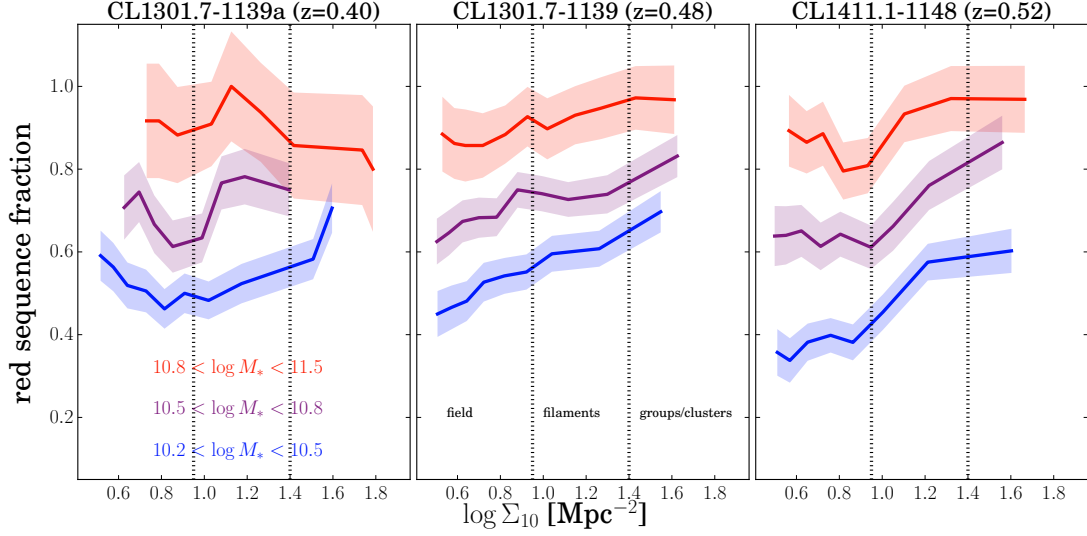


Figure 4.9 – Fraction of galaxies in the red sequence as a function of density, for different stellar mass intervals. The binning in density is adaptive: the lower bound of each bin increases by steps of 0.1 and the upper bound is chosen such as each bin contains $1/5^{th}$ of the objects (in the given stellar mass interval). With this binning, the error bars are constant (since they depend only on the number of objects in the bin). The dotted lines are the thresholds separating the density field between the field, filaments and groups/clusters.

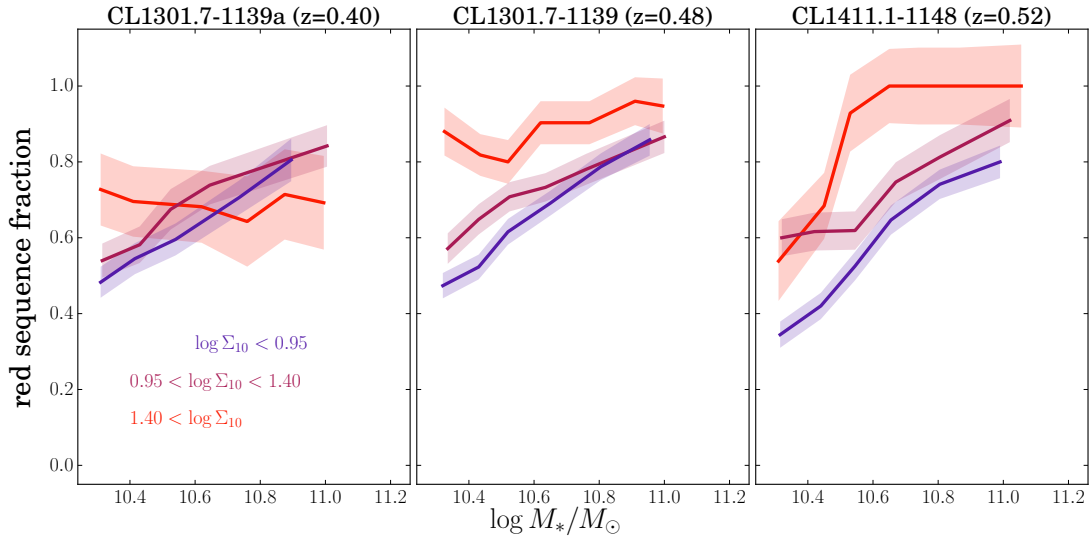


Figure 4.10 – Fraction of galaxies in the red sequence as a function of stellar mass, for different local density intervals (corresponding to the field, filaments and groups/clusters). The binning in stellar mass is adaptive: the lower bound of each bin increases by steps of 0.1 and the upper bound is chosen such as each bin contains $1/5^{th}$ of the objects (in the given density interval).

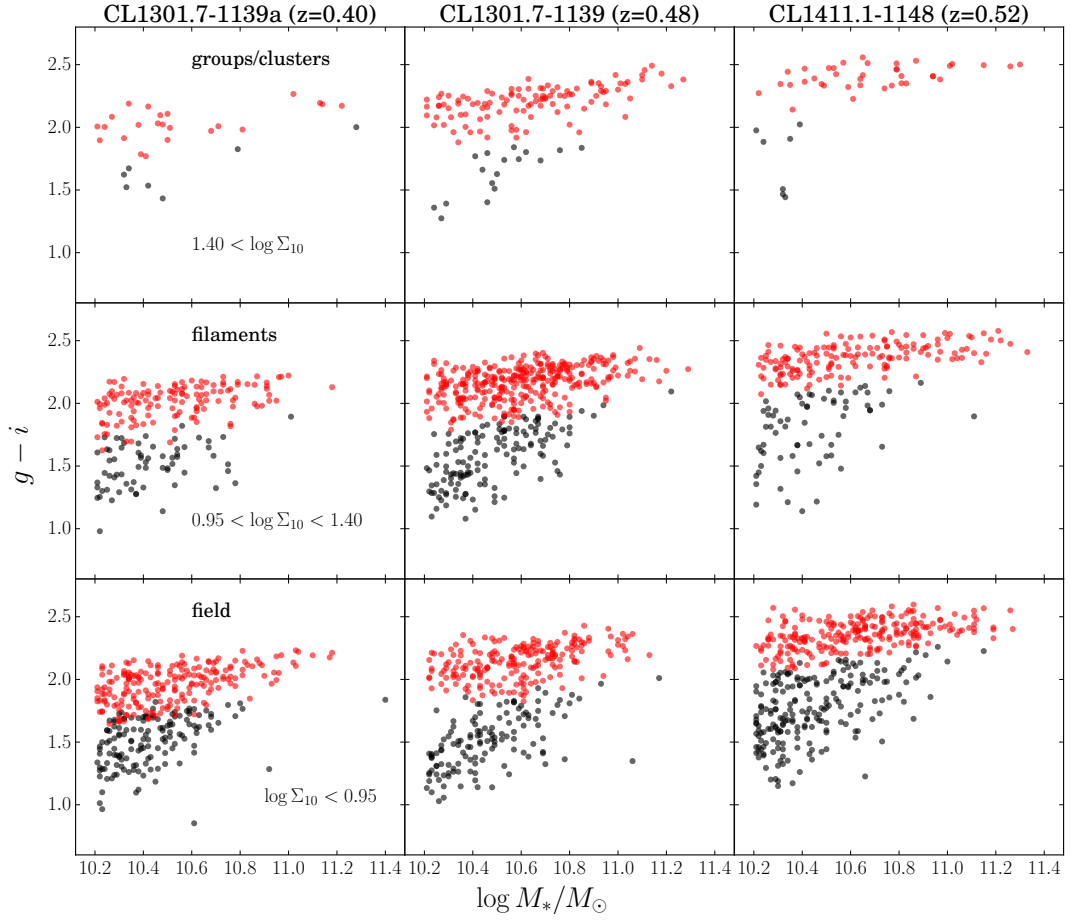


Figure 4.11 – $g-i$ colors as a function of stellar mass. The panels correspond to different clusters (columns) and local density intervals (rows). The density intervals select different environments, namely the field (bottom row), filaments (middle row) and groups/clusters (top row). M_* is expressed in solar mass units.

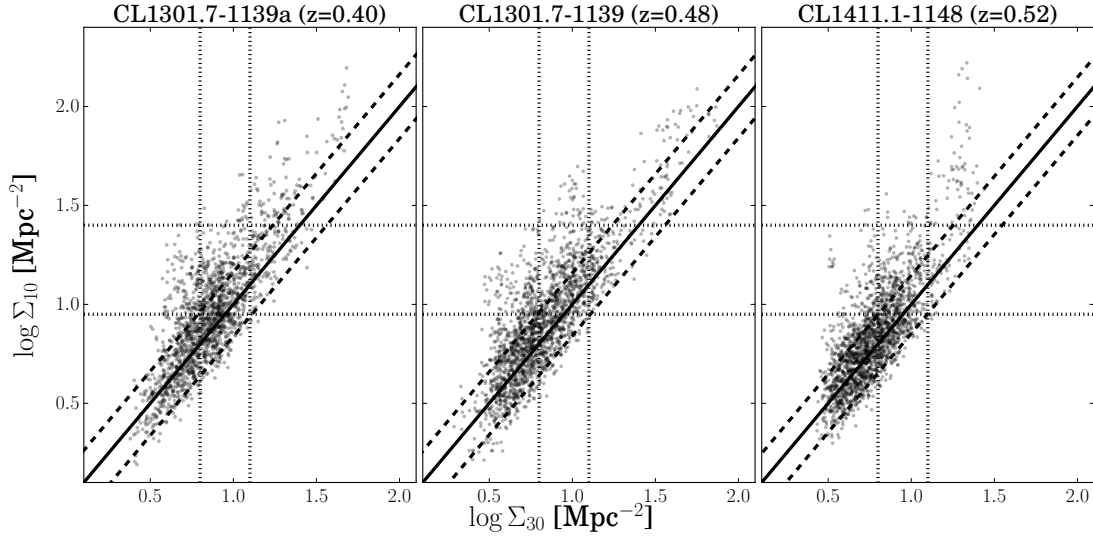


Figure 4.12 – Local versus global density, for each galaxy close to the cluster redshift. The dotted lines show the density thresholds used in Fig. 4.1, 4.2, 4.3 and 4.9. The dotted lines are the thresholds separating the global and local density fields between the field, filaments and groups/clusters.

4.3.3 The dominance of small scales

We want to assess whether small or large scales are more important for galaxy properties. For this, we computed the local (Σ_{10}) and global (Σ_{30}) density and compared the fraction of red sequence galaxies for both measures. Fig. 4.12 shows the global and local density of each galaxy. In general, there is a larger range for the local densities (as we already saw in Fig. 3.30). Even for low global densities, there exists high local densities. This shows that using only the global density misses some relatively high density substructures.

We split the sample by global density. We show galaxy colors (Fig. 4.13) and the fraction of red galaxies (Fig. 4.14) as a function of the local density, for each of the global density ranges. We see that galaxy colors still depend on the local density after this separation. On the other hand, at a fixed local density, the global density matters as well: the fraction of red sequence galaxies increases for higher global densities.

Fig. 4.15 shows the fraction of galaxies on the red sequence as a function of the global environment. Galaxies are separated depending on whether the local density is higher or lower than the global one. At high global densities, we see clearly that if the local density is higher, the fraction of red sequence galaxies is larger. It means that the quenching is dominated by effects on small scales. At small densities, the two curves essentially overlap. This can be interpreted in two ways: *i*) at low densities, environmental effects are weak or almost inexistent, so there is no difference between local and global environment, or *ii*) quenching on large scales dominates for low density environment, thus the density at small scales does not matter.

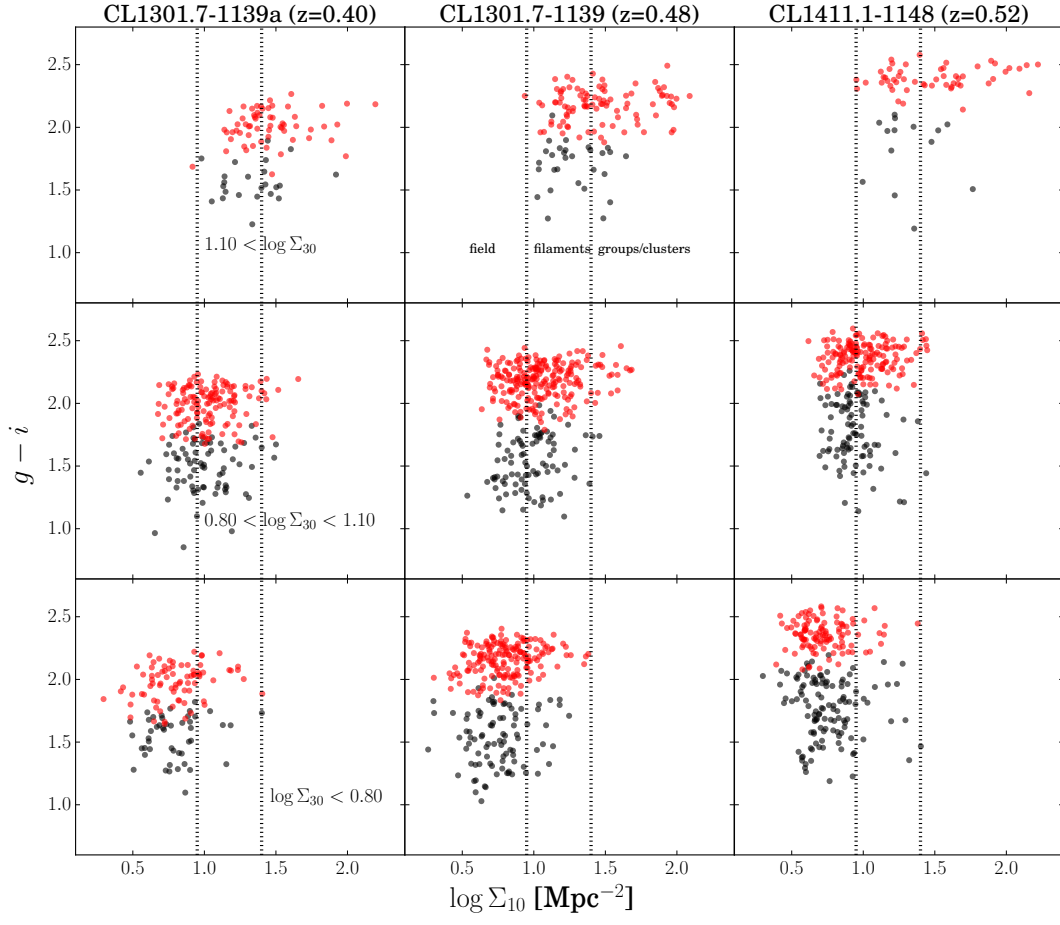


Figure 4.13 – $g-i$ colors as a function of the local density. The panels correspond to different clusters (columns) and global density intervals (rows). The dotted lines are the thresholds separating the local density field between the field, filaments and groups/clusters.

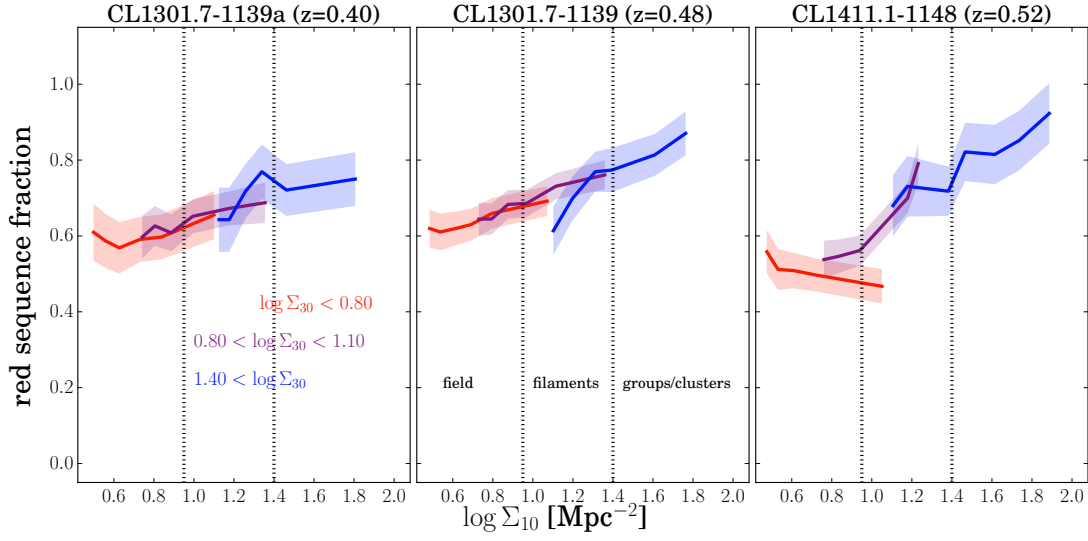


Figure 4.14 – Fraction of galaxies in the red sequence as a function of density, for different density intervals. The binning in density is adaptive: the lower bound of each bin increases by steps of 0.1 and the upper bound is chosen such as each bin contains $1/5^{th}$ of the objects (in the given stellar mass interval). The dotted lines are the thresholds separating the global density field between the field, filaments and groups/clusters.

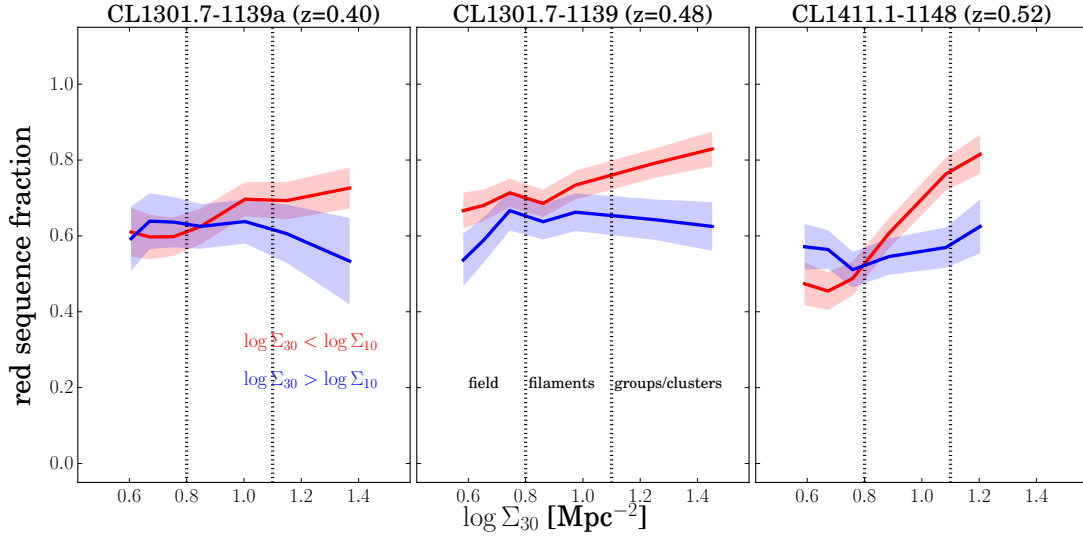


Figure 4.15 – Fraction of red sequence galaxies as a function of the global environment. In red (blue): galaxies whose local density is higher (lower) than the global one.

4.4 Discussion

The results obtained so far can be summarized as follows (they are all based on the *photo-z* selected LSS sample, Section 3.2.5):

- the local and global density of galaxies define a complex network of structures, centered on the clusters (Section 4.1). These structures are not distributed around the cluster in a symmetrical way.
- The fraction of galaxies on the red sequence depends on the local density for the whole density range available (Section 4.3.1).
- This correlation weakens when the sample is split in different stellar mass ranges. It seems that massive galaxies are less sensitive to the environment than lighter galaxies (Section 4.3.2).
- An empirical separation (based on different density thresholds) between field, filaments and groups/clusters shows that even within filaments, the fraction of red sequence galaxies is higher compared to the field (Section 4.3.2).
- The environment of galaxies at small scales affects more strongly galaxies than at large scales (Section 4.3.3).

Many authors have explored correlations between galaxy properties and their number density. Nevertheless, it is not easy to find studies for which our results are directly comparable. Our dataset is characterized by 6 key properties: it is focused on clusters, of medium-mass, at intermediate redshifts, studied mostly with *photo-z*, over a wide-field, the sample is complete in stellar mass down to $\sim 10^{10} M_{\odot}$. At the time of writing, there is no other published study combining all these characteristics. We will still try to compare our results, trying qualitatively to take into account the inhomogeneities between the datasets.

The increase of the fraction of red galaxies with local density, with a flattening of the relation with stellar mass is comparable to Baldry et al. (2006); Haines et al. (2007); Peng et al. (2010); Kovač et al. (2014). These trends seem well established, even if the survey are not exactly in the same redshift range and do not have the same stellar mass completeness.

Multiscale studies comparing local and global densities are more scarce. Blanton and Berlind (2007) and Wilman et al. (2010) find that galaxy colors in groups are influenced by the environment only within 1 Mpc from the cluster center. However, Wilman et al. (2010) find that for a fixed local density, the fraction of red galaxies anticorrelates with the large scale density. It seem to contradict our results since we see a correlation with density both for the local and the global scales. Nevertheless, they use fixed aperture density measures in various annuli, making a direct comparison difficult. In a sense, it is at least compatible with our finding that local densities are more influential than the global ones.

Chapter 4. Results

The main point of this chapter is that pre-processing by the environment occurs at all scales. Clusters are not isolated structures where all the quenching phenomenon take place. We have shown they are connected to large scale structures which are already responsible for at least a partial quenching. While cluster-centric distance matters within $\sim 2R_{200}$, at larger distances the position of galaxies in the large scale structures is more relevant. A full understanding of the mechanisms responsible for galaxy quenching is only possible by studying galaxies over large scales (say $\sim 8-10 R_{200}$).

5 Spectroscopy

Until summer 2014, our data consisted of photometry over 1 deg^2 in *ugriz*, for 3 clusters, from which I have derived *photo-z* and stellar masses. It allowed to create map of the large scale structures around the clusters, with an analysis of the dependence of galaxy $g - i$ colors on stellar mass and density. The next step of the thesis was to use spectroscopy to obtain accurate redshifts to confirm the reality of the *photo-z* detected structures and analyze the SFR in the different environments. I will describe here the observational strategy, the data reduction and results.

5.1 Observational strategy

At the time when the proposal was made (March 27th 2013, ESO phase 92A), we only had a complete *ugriz* dataset for CL1411.1-1148, therefore we requested spectroscopy only for this field.

5.1.1 Choice of the instrument

For the photometry, we chose to use MegaCam because it operates in the optical, has a large FoV and a good spatial resolution (Section 2.2). We designed the spectroscopic observational strategy to somehow match the photometric one. We needed an optical instrument with a large FoV, capable of observing as many galaxies as possible in one telescope pointing and with a spectral resolution allowing redshifts measurements at a resolution corresponding at least to the clusters velocity dispersions. Keeping in mind that observing a galaxy (of a given magnitude) in spectroscopy is more time consuming than in photometry, these requirements can only be satisfied (within reasonable telescope time) on 6 meter-class (and above) telescopes.

The VISIBLE MultiObject Spectrograph (VIMOS; Le Fèvre et al. 2003) on the VLT is one of the instrument matching best our strategy. The detector is composed of four 2048×4096 pixels CCD with a spatial resolution of $0.2''$ per pixel, corresponding to a $4 \times 7' \times 8'$ field of view (with $2'$

gaps between the CCDs). The medium resolution grism with filter GG475 covers 4800-10 000 Å at a resolution $R=580$ (2.5 Å per pixel). At $z \sim 0.4-0.5$, this wavelengths range contains several of the strongest emission lines found in galaxies: [OII] (3727.30 Å), $H\beta$ (4861 Å), the [OIII] doublet (5007, 4959 Å) and $H\alpha$ (6563 Å). In absorption, there is especially Ca H&K (3934, 3968 Å). The spectral resolution corresponds to a redshift resolution (at central wavelength) $\Delta z \sim 0.00032$ or a cluster relative velocity of $\Delta v = c\Delta z/(1 + z_{cl}) \sim 63 \text{ km/s}$. This resolution in velocity is more than ten times lower than the cluster velocity dispersion, therefore perfectly adequate to identify members of the LSS surrounding the clusters.

5.1.2 Field selection

The positioning of the fields was performed on the basis of the density maps created from the distribution of the *photo-z* selected LSS members (Fig. 5.1, similarly to the top panel of Fig. 4.3). Covering the whole MegaCam FoV with VIMOS would have been too expensive. Our pointings were optimized *i*) to center at least one of the VIMOS chips on a strong overdensity *ii*) to cover the total area of the large scale structures as well as possible and *iii*) to avoid that one of the gaps between the quadrants falls on a high density region. We estimated that a minimum of 6 pointings was needed.

5.1.3 Observations

At $r=23.2$ (our limiting magnitude), dark time, seeing 0.8", airmass 1.2, 1" slit width, and with the medium resolution grism, exposures of 2 hours deliver a signal-to-noise ratio of 7.5 per pixel at the central wavelength, hence perfectly adequate for our purpose. Given the 30 minute overheads per observation block (OB), we had to split the observations of each field into 4 OBs of 1 hour. Each 30 min OB was split in 3 sub-exposures, allowing to use nodding for a better sky subtraction.

The data (run ID 092.A-0615) were gathered between March 27th and August 2nd 2014. 20 out of 24 OBs were completed. They all have the best quality rating (*A*, meaning that all our requirements were satisfied), except one with *B* because one mask for quadrant 1 was not correctly loaded and one with *C* because of the close moon (the sky is 2-3 times larger than in other exposures in the same quadrant of another night). Field 4 has 3/4 completed exposures. Field 2 has 1/4, but since this is the *C* rated exposure, we have asked the exposure to be retaken and do not use it in our analysis.

To allow an accurate positioning of the slits in the mask design, we requested VIMOS pre-imaging, with 5 min exposures in *R* band in each of our 6 pointings.

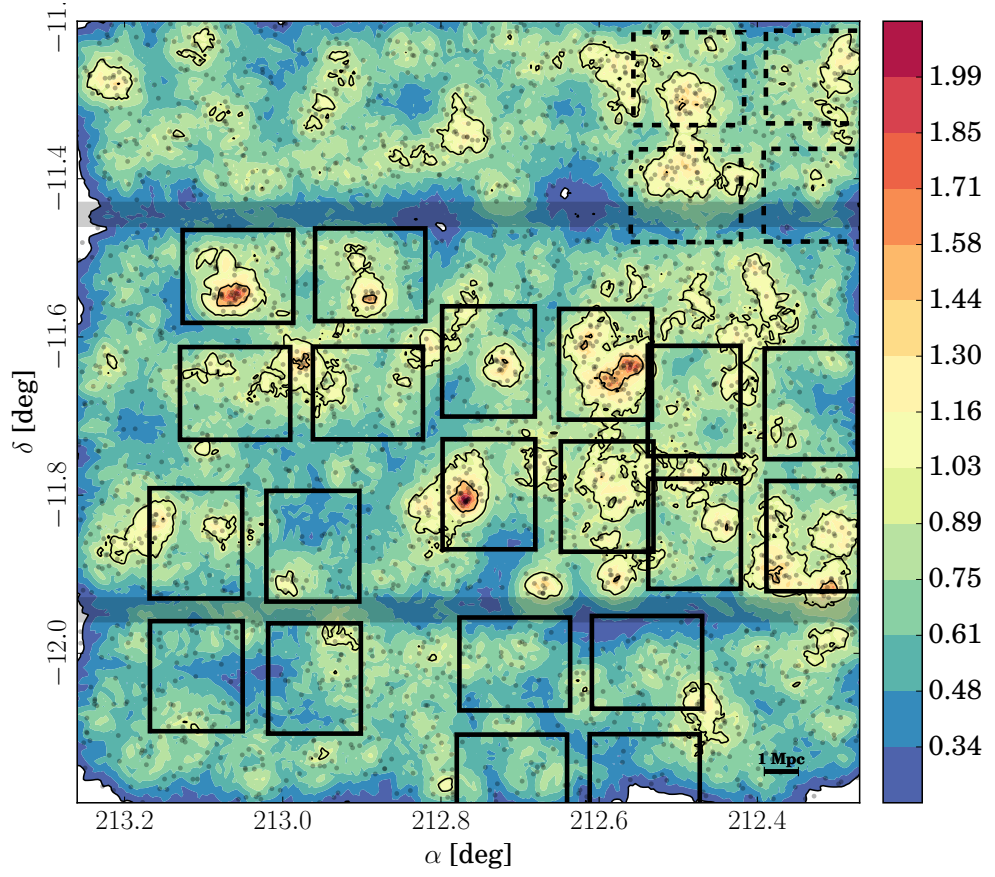


Figure 5.1 – Density map used to choose the pointings (realized in the same way as Fig. 4.3). The light black dots are the *photo-z* selected large scale structures members of CL1411.1-1148, while the color code represents $\log \Sigma_{10}$. The 6 x 4 rectangles correspond to each chip of VIMOS for the 6 telescope pointings. The dashed rectangles are the observations which were not completed.

5.1.4 Target selection and mask design

The parent sample comes from the *photo-z* sample of CL1411.1-1148 selecting the large scale structures (Section 3.2.5). This allows a much higher chance to select members of the large scale structures around the cluster than a naive flux limited selection. The target selection is $r < 23.5$ (in 2 arcsec radius apertures) and *photo-z* within $z_{cl} \pm 0.1$ (in addition to the usual cuts of the final *photo-z* sample, i.e. FWHM in $i < 0.55''$, $i > 18$ and $odds > 0.8$). We chose to use 1 mask per field, even if it meant we could not observe all the candidates. This is better than wasting slits if there was a lack of candidates. This target selection is very conservative. A lower magnitude limit and a narrower redshift range would have yielded a lower fraction of contamination, but we wanted to have enough targets even in the lower density quadrants and to apply the same selection criterion for the whole sample.

We also targeted the LDP cluster candidates (at any z_{phot}), since the accuracy of LDP ($3\sigma \sim 0.02$) is too low to determine unambiguously the cluster membership ($\sigma_{cl} \sim 710$ km/s or $\Delta_{cl} \sim 0.0036$).

Galaxies near the edges of the dispersion axis will have an incomplete spectrum. We selected the targets such as [OII] at $z = 0.5$ is always within the detector surface.

The mask design was achieved with the VIMOS Mask Preparation Software 3.28 (VMMPS, Bottini et al. 2005). The highest priority (“compulsory”) was given to the LDP targets and all the *photo-z* targets received the normal priority (“selected”). Three reference stars (“reference”) were given per quadrant. For a good sky subtraction, we requested a minimum slit length of 5 arcsec on both sides of the targets. The slits are assigned automatically by the software, which aims to maximize the number of targets (with a priority for the “compulsory” objects). The slit length is increased when there is enough space between the targets. Altogether, we were able to assign 412 slits for the 4x5 quadrants.

5.2 Reduction

The extraction of the spectra is performed with Reflex 2.6 (Freudling et al. 2013), the ESO framework designed to reduce the data. The reduction is standard, with all the parameters set to their default value. The one-dimensional spectra obtained with Reflex are stacked per OB, meaning the dithered sub-exposures are combined together, but the OBs corresponding to the same field still have to be stacked. This is done with the `scombine` task of IRAF (Tody 1993), with a median stacking to remove remaining cosmic rays (the extended ones are not always detected by Reflex).

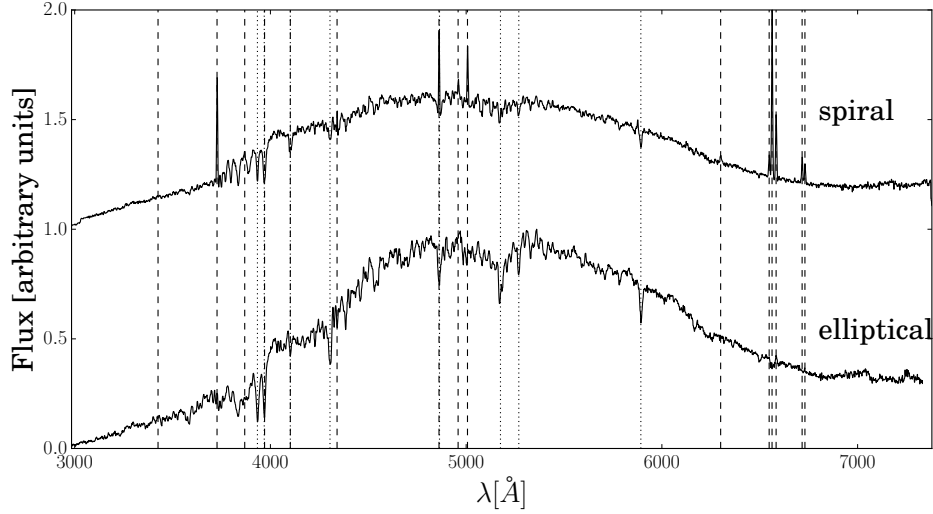


Figure 5.2 – Galaxy templates used to extract redshifts with RVSAO. Dashed (dotted) lines are emission (absorption) lines. For clarity, the spiral template is offset by 1 on the y-axis.

5.3 Extraction of physical measurements

5.3.1 Redshifts

Redshifts are computed with the XCSAO task of the IRAF RVSAO package 2.0 (Kurtz and Mink 1998). The method cross-correlates the Fourier transforms of the spectrum and of template spectra, and computes the redshift corresponding to the highest peak in the cross-correlation function. For our case, we simply used an elliptical template without emission lines and a spiral template with emission lines. Their spectra are presented in Fig. 5.2. Due to the FWHM cut in the target selection, there are very few stars, so we do not use any star template to limit degeneracies. All the redshifts were double-checked by eye and we removed all the spurious/inconclusive cases. Fig. 5.3 shows an example of galaxy spectra with emission lines (top), without emission lines (middle) and with a SNR too low to assign a redshift. The redshift error is estimated as the FWHM of the peak in the cross-correlation function. Fig. 5.4 shows the distribution of the redshift errors.

Out of the 432 slits positioned in the masks, we obtained a secure redshift for 376 targets. Most of the wrong redshifts are for faint objects. We could also assign redshifts for 16 galaxies observed by chance (i.e., galaxies close enough from the targets to fall in the same slit).

5.3.2 Star formation rate

We use [OII] as a proxy for star formation rates, with the calibration of Kennicutt (1998):

$$SFR = 1.42 \cdot 10^{-42} L_{[OII]} , \quad (5.1)$$

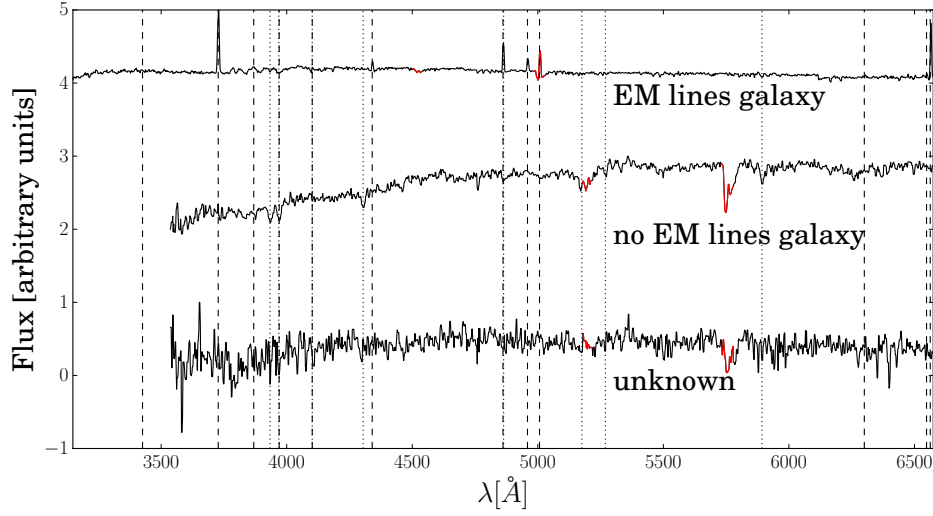


Figure 5.3 – Example of VIMOS spectra of galaxies with emission lines (top), without EM lines (middle) or inconclusive. The spectra are deredshifted. The red segments of the spectra highlight the O_2 atmospheric absorption lines. For clarity, the spectra are offset from each other by 1 on the y-axis.

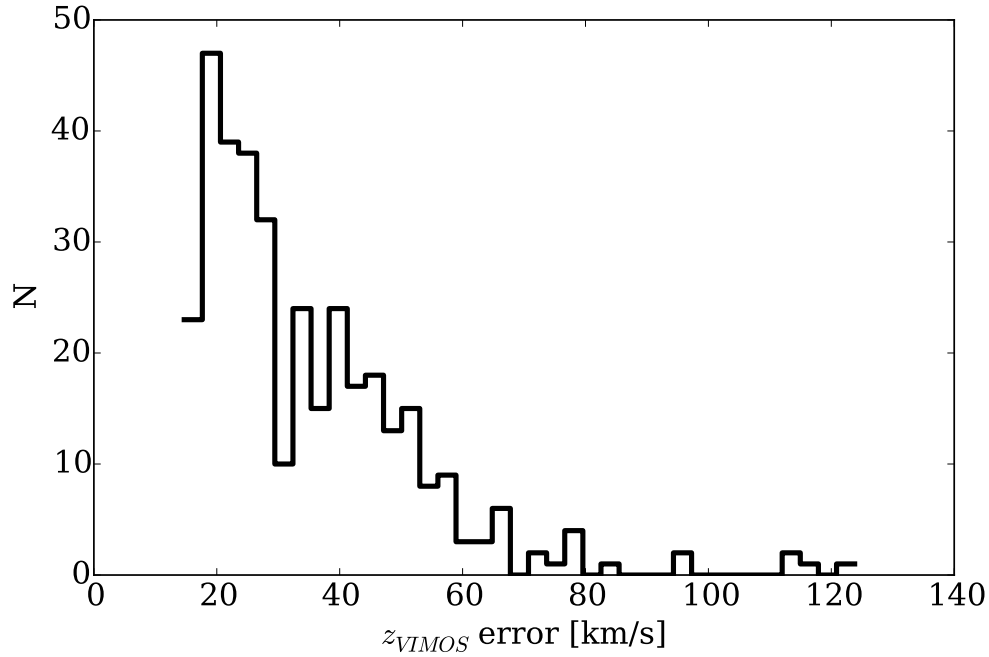


Figure 5.4 – Errors on the VIMOS redshifts estimation, estimated from the width of highest peak in the cross-correlation function between the Fourier transforms of the template galaxy and the spectrum.

with $L_{[\text{OII}]}$ the integrated luminosity of the [OII] line. It is computed as $L_{[\text{OII}]} = 4\pi D_L(z)^2 f_{[\text{OII}]} / (1+z)$, where $D_L(z)$ is the luminosity distance at redshift z and $f_{[\text{OII}]}$ is the integrated flux of the [OII] line above the continuum:

$$f_{[\text{OII}]} = \int_{\Delta\lambda} (f_\lambda - f_0) d\lambda. \quad (5.2)$$

f_λ is the flux of the spectrum per unit wavelength and f_0 is the value of the continuum. For the integration range, we chose $\Delta\lambda = (3727 \pm 10 \text{ \AA}) \cdot (1+z)$, which encompasses well the [OII] line for the galaxies in our sample. The continuum is determined with a method inspired from Goto et al. (2003). It is simply estimated as the average value of the flux in the (rest-frame) window 3653-3713 Å.

We do not apply any extinction correction. It means our SFR are likely underestimated. However, the absolute value of the SFR is not crucial for us, we only want to make relative comparisons within the sample.

The absolute flux calibration of the VIMOS spectra is not perfect. It does not influence the redshift accuracy, but is an issue for the measure of $f_{[\text{OII}]}$. Nevertheless, it is possible to use the broad band photometry to recalibrate the spectra. We integrated the spectrum (of a given galaxy) in the r -band to obtain f_r^{VIMOS} , the VIMOS flux in r . We computed the ratio $f_r^{\text{MegaCam}} / f_r^{\text{VIMOS}}$, where f_r^{MegaCam} is the flux measured in the MegaCam images. The recalibrated flux in [OII] is then:

$$f'_{[\text{OII}]} = f_{[\text{OII}]} \frac{f_r^{\text{MegaCam}}}{f_r^{\text{VIMOS}}}. \quad (5.3)$$

The aperture used for the extraction of the one-dimensional spectra is of 2.4" in average. With the slit width of 1", it means the surface of the measurement is of $\sim 2.4 \text{ arcsec}^2$. The aperture used to measure f_r^{MegaCam} should be similar. We chose 1.5" in diameter, which covers a slightly smaller surface than the spectroscopic integration, to avoiding extending too much along the slit width.

[OII] is the strongest emission line which is in the VIMOS wavelength range at $z \sim 0.5$. $H\alpha$ is a more direct diagnostic for SFR, however at $z \sim 0.5$ it falls in the red part of the VIMOS range, where the sky lines are important and harms the measure.

5.3.3 Equivalent width measurement

Equivalent widths (EWs) are defined as follows:

$$W_\lambda = \int_{\Delta\lambda} (1 - f_\lambda / f_0) d\lambda, \quad (5.4)$$

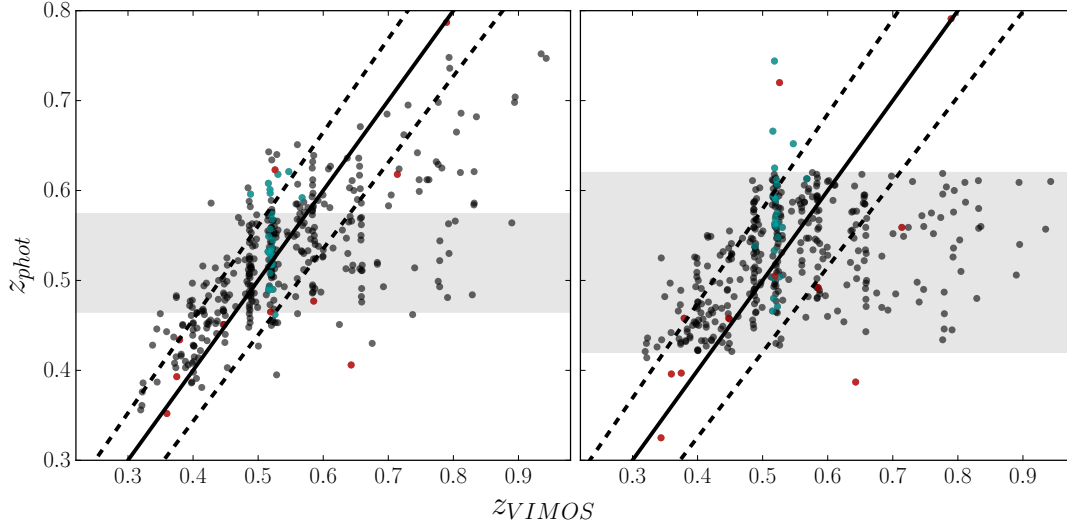


Figure 5.5 – Photometric versus spectroscopic redshift. Left: last version of the *photo-z*, the shaded area is the *photo-z* interval used for the selection of the LSS. Right: *photo-z* at the time of the target selection, the shaded area is *photo-z* interval used for the target selection. Blue: galaxies with an LDP redshift at $z_{cl} \pm 0.02$. Red: galaxies which are by chance in a slit (they were not in the target selection). The solid line shows the 1:1 relation, while the dashed lines correspond to $\pm(1 + z_{spec}) \cdot \sigma_{NMAD}$.

where $\Delta\lambda$ is the width of the line centered on λ , f_λ is the flux of the line over $\Delta\lambda$ and f_0 is the continuum value within $\Delta\lambda$. For emission lines, W_λ is negative.

The measurements are performed with the IRAF `sp1ot` task. The continuum and integration ranges are the same as for the SFR determination from [OII] (Section 5.3.2). The EWs can be used as a criterion for the detection of the [OII] line. For the FORS2 spectra of EDisCS, Poggianti et al. (2006) find that the detection limit is $W_{[OII]} = -3 \text{ \AA}$. The VIMOS spectral resolution is slightly worse (2.5 \AA per pixel instead of 1.6 for FORS2) and in general the SNR of our observations is lower. The same methodology as in Poggianti et al. (2006) yields limit of $W_{[OII]} = -5 \text{ \AA}$.

The measurements of $W_{[OII]}$ and SFR were also realized for the FORS2 cluster members, following exactly the same procedure as for VIMOS.

5.4 Efficiency of the *photo-z* selection

Fig. 5.5 shows the *photo-z* against the VIMOS redshifts, with the last version of the *photo-z* (left, without any cut) and the ones at the time of the mask design (right). For the VIMOS redshifts, the accuracy of the *photo-z* has been improved from $\sigma_z = 0.053$ to 0.041 and the outlier fraction from 5.1 to 3.1% . This accuracy for the last version of the *photo-z* is compatible with the one computed from the FORS2 and LDP sample ($\sigma_z = 0.037$). There is a surprisingly large number

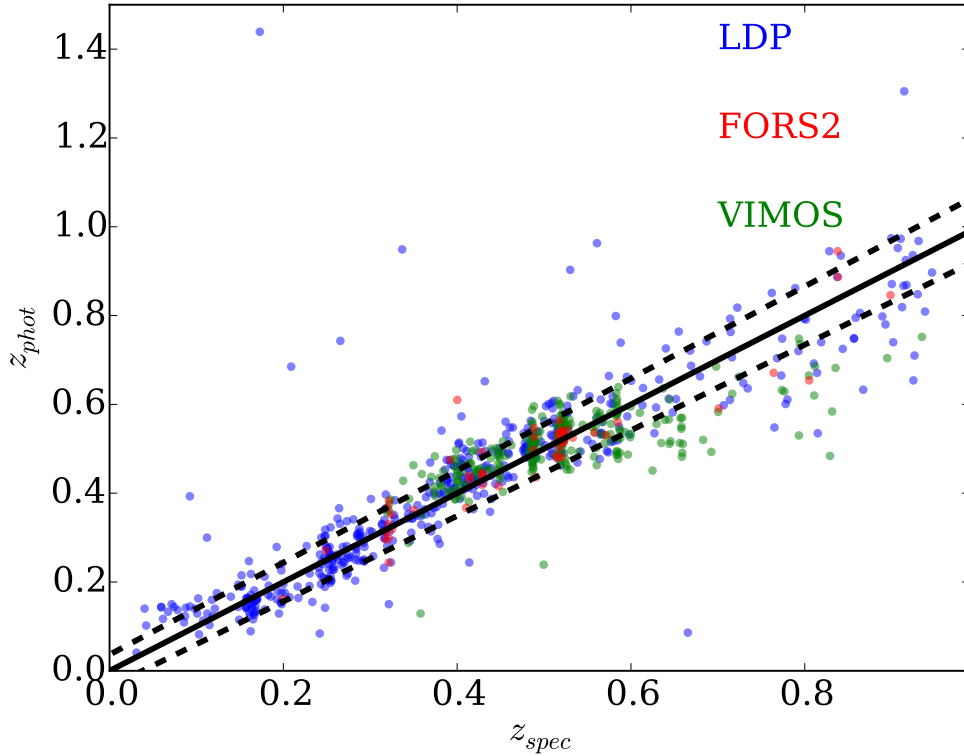


Figure 5.6 – Photometric versus spectroscopic redshift, for FORS2, LDP and VIMOS samples. The solid line shows the 1:1 relation, while the dashed lines correspond to $\pm(1+z_{spec}) \cdot \sigma_{NMAD}$.

of outliers at $z > 0.6$. It could be due to the lack of galaxies at these redshifts in the LDP+FOR2 sample used to calibrate the *photo-z* (see Fig. 3.21).

For the whole FORS2, LDP and VIMOS spectroscopic sample (Fig. 5.6, this time with all the cuts from Section 3.2.4), the median of Δz is -0.007, $\sigma_z = 0.036$ and $f_{\text{outliers}} = 2.2\%$, which is very similar to the statistics without VIMOS (see Section 3.2.4).

The spectroscopic redshift distribution (from all instruments) is shown on Fig. 5.7 (top). We see that a significant fraction of the VIMOS targets are located around $z \sim 0.49$. While this redshift is not exactly the redshift we were looking for (0.52), it is possible that all the galaxies near 0.49 form a structure which belongs to the same superstructure as CL1411.1-1148 (more details in Section 5.5.1).

In the definition of Milvang-Jensen et al. (2008), galaxies are considered as cluster members if their redshift lies within $z_{\text{cl}} \pm 3\nu_{\text{cl}}$. As the LSS around the cluster are not necessarily exactly at the same redshift as the cluster (there is no reason for them to be extending only on the plane of the sky), we consider that galaxies are members of the same structure as CL1411.1-1148 if they are within $4\nu_{\text{cl}}$ of the cluster redshift. This range is represented by the black horizontal

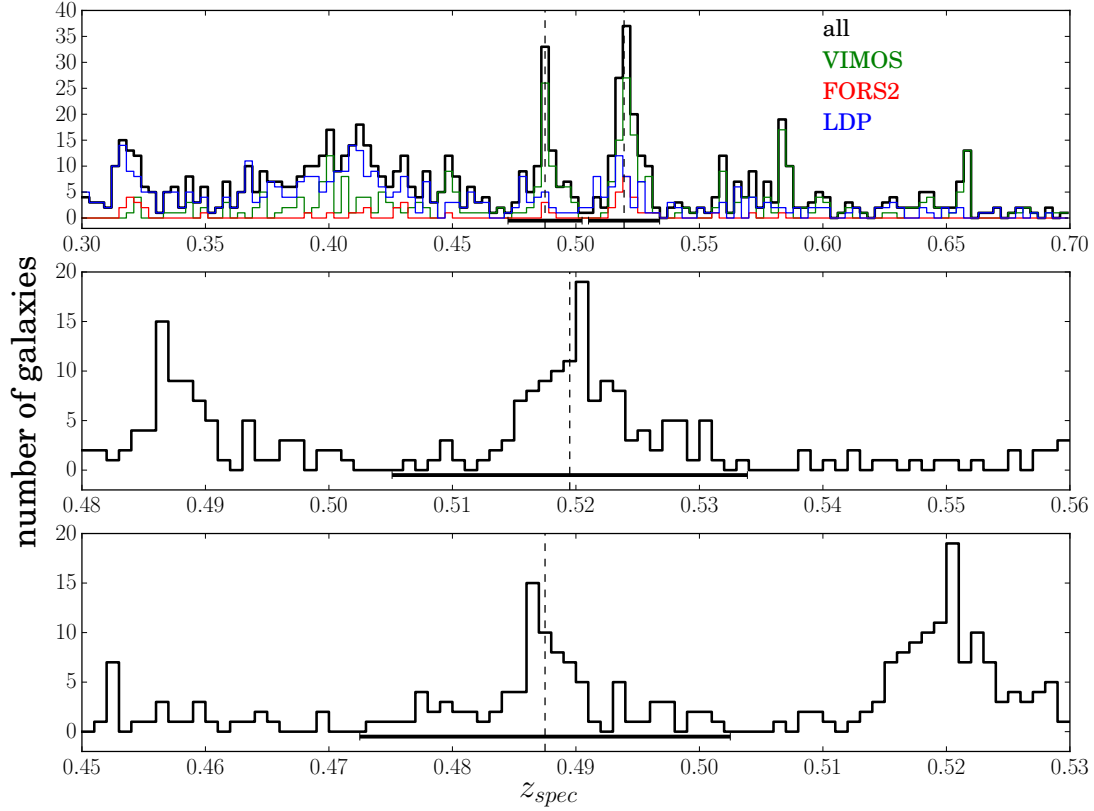


Figure 5.7 – Spectroscopic redshifts distributions. Top: in black, all the redshifts from any instrument for $0.3 < z < 0.7$, FORS2 redshifts in red, LDP in blue, VIMOS in green. Middle: zoom on the $0.48 < z < 0.56$ region, with the black bar showing the CL1411.1-1148 cluster membership area ($0.5195 \pm 4\nu_{cl}$). Bottom: zoom on the $0.45 < z < 0.53$ region, with the black bar showing the CL1411.1-1148a membership area (0.4875 ± 0.015). The dashed lines are the cluster redshifts: 0.5185 for CL1411.1-1148 and 0.4875 for CL1411.1-1148a (see text).

line in the middle panel of Fig. 5.7. For the structure at $z = 0.49$, the redshift distribution (bottom panel of Fig. 5.7) peaks at $z=0.4875$. This is what we will consider as the central redshift of the structure. The conservative redshift interval encompassing the peak of the distribution is 0.015 (or ~ 3000 km/s). From now on, we will call this structure CL1411.1-1148a.

From the 392 galaxies with secure redshift, 81 are within the range of CL1411.1-1148 and 59 within CL1411.1-1148a. It corresponds to a success rate of 21 % for CL1411.1-1148 (15 % for CL1411.1-1148a), lower than what was expected from the success rate defined in Table 3.2 (36 %). This is due to the fact that the mask were created with an older version of the *photo-z* (less accurate) and that we had to use a larger *photo-z* interval than the one used to create the Table 3.2. This is still almost 3 times better than the success rate of LDP (7.6 %, 57 CL1411.1-1148 members out of 751 redshifts), which used a purely flux-limited target selection. Moreover, some of the quadrant fell on relatively low density regions, where it was expected to have a lower success rate. If we compute the success rate only for the regions with a density

above the filament threshold ($\log \Sigma_{10} > 0.95$), it increases to 39 % (34 CL1411.1-1148 members out of 88 galaxies) for CL1411.1-1148 and 24 % for CL1411.1-1148a.

The distinction between CL1411.1-1148 and CL1411.1-1148a is essentially impossible with photometry in only 5 broad band filters. Ilbert et al. (2013) have 30 bands and reach an accuracy of *photo-z* of ~ 0.015 (at $z=0.5$), therefore even such a large amount of filters is barely enough to separate two structures at $z=0.49$ and 0.52 . The detection of a secondary structures at $z=0.4875$, likely connected to CL1411.1-1148, should in fact be considered as a success. In this case, the success rate for the whole sample is $21+15=36$ %, and raises to $39+24=63$ % in the high density regions ($\log \Sigma_{10} > 0.95$). Our *photo-z* based target selection is a great success.

5.5 Results

5.5.1 Confirmation of the *photo-z* selected large scale structures

The density of the slits is too low to permit a direct confirmation of the structures seen in the density maps (see e.g. Fig. 5.1). Nevertheless, it is possible to recompute “clean” maps using all the information we gained from the spectroscopy. From the *photo-z* sample selecting the LSS (Section 3.2.5), we remove all the galaxies with z_{spec} outside the cluster redshift range and add all the ones which are cluster members (i.e. within $z_{\text{cl}} \pm 4\nu_{\text{cl}}$). The resulting density map is shown on Fig. 5.8. It is computed in the same way as in Fig. 5.1. We chose the local density estimation, since it is more sensitive to small variations in the density field. The red (blue) symbols are the CL1411.1-1148 (CL1411.1-1148a) members. The general aspect of the map is very similar to the one of figure Fig. 4.3 (top panel). The most noticeable features highlighted by the spectroscopy are the following (the numbers are reported in Fig. 5.1):

1. top right black circle: after the cluster, this is the highest concentration of galaxies within the cluster redshift range. In projected distance, it is at less than $5 R_{200}$ from CL1411.1-1148. It is likely a group falling on the cluster.
2. top middle black circle: this high concentration clump makes an ideal group candidate as well.
3. top left black circle: this is also a possible group, but a member of CL1411.1-1148a. The comoving distance between CL1411.1-1148 and CL1411.1-1148a is 107 Mpc. In the local Universe, it corresponds to the distance between the Milky Way and the Coma cluster (102 Mpc), which does not belong to the same supercluster as the Milky Way. However, this is smaller than the size of the Laniakea Supercluster (Tully et al. 2014), whose major axis extends of over 160 Mpc. It means that CL1411.1-1148a is likely too large and far away from CL1411.1-1148 to be simply a small group being accreted on the cluster, but we cannot rule out the hypothesis that it is a low mass cluster belonging to the same superstructure as the main cluster.
4. black line: this arcs follows a concentration of galaxies with redshifts mixed between

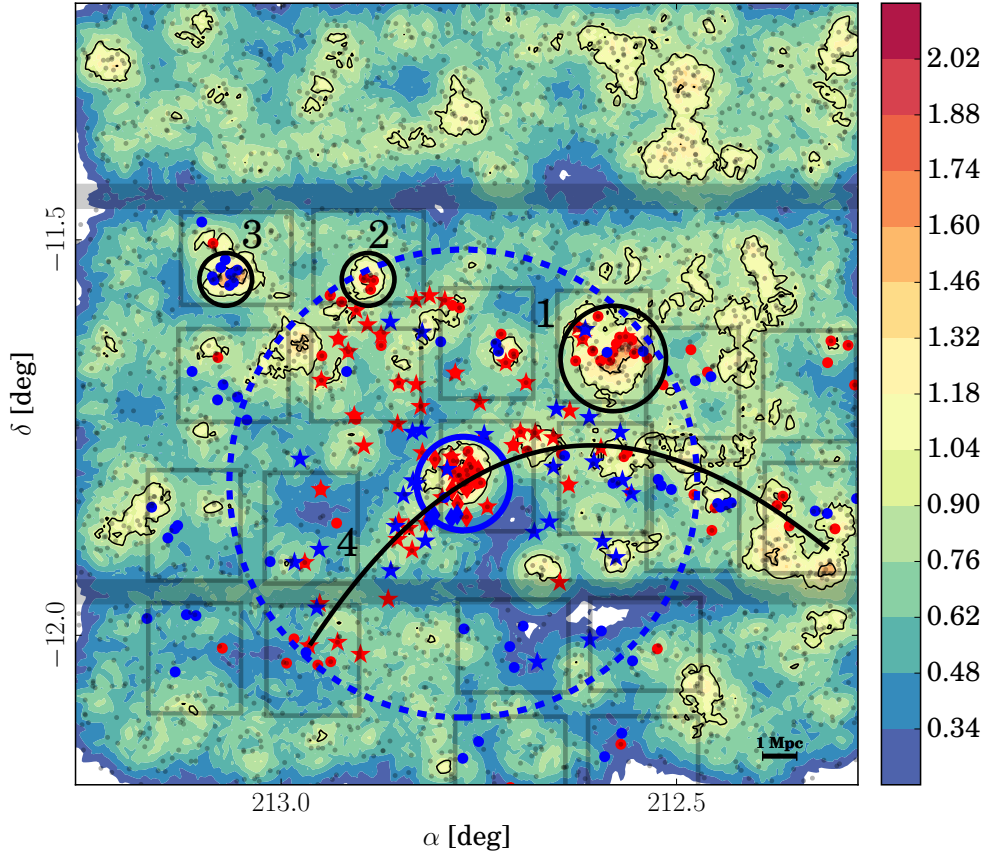


Figure 5.8 – Similar to Fig. 5.1 (and the top panel of Fig. 4.3). The color codes the density $\log \Sigma_{10}$ in Mpc^{-2} . The parent distribution (black dots) is the *photo-z* selected LSS members, without the spectroscopic non-members. The red (blue) symbols are the CL1411.1-1148 (CL1411.1-1148a) members (defined in Fig. 5.7). Stars are from LDP redshifts, (large) dots from VIMOS and diamonds from FORS2. The black line and circles highlight regions of interest (see Section 5.5.1). The blue circle is the cluster R_{200} and the dashed one is $5R_{200}$. The 5×4 light dark rectangles correspond to each chip of VIMOS for the 5 telescope pointings. The thin black contours separate the density field between the field, filaments and groups/clusters. The thick black line and circles highlight regions of interest (see Section 5.5.1).

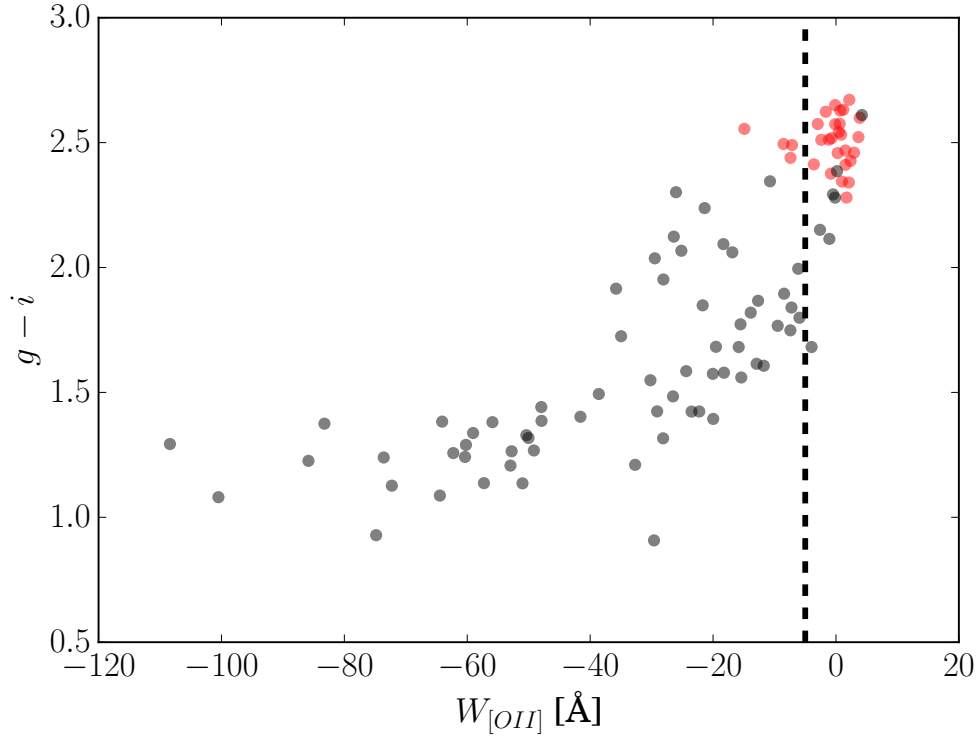


Figure 5.9 – $g - i$ color as a function of the [OII] equivalent width, for the CL1411.1-1148 members with FORS2 or VIMOS spectroscopy. Red sequence members are in red. The dashed line is at $W_{[\text{OII}]} = -5 \text{ \AA}$, above which [OII] is considered undetected.

CL1411.1-1148 and CL1411.1-1148a. We could speculate it does not represent just a filament, but a wall whose plane extends mostly along the line-of-sight. It also seems to be bended by the attraction of the top right group.

5.5.2 Fraction of [OII] detected galaxies

In the previous chapter, we considered that galaxies are quenched if they belong to the cluster red sequence. As already mentioned (Section 4.2), this is statistically true, although dusty star-forming galaxies may lie on the red sequence. The spectroscopy allows a more sensitive criterion. We will consider that quenched galaxies are the ones which do not have a detected [OII] emission line, i.e. $W_{[\text{OII}]} > -5$ (see Section 5.3.3). Again, this is not a perfect criterion, as it may be undetected because the SNR of the spectrum is too low and extreme intrinsic extinction can shutdown the [OII] line, but it is still more sensitive than the red sequence criterion.

We compare the two criteria in Fig. 5.9, showing $g - i$ color as a function of $W_{[\text{OII}]}$. The dashed

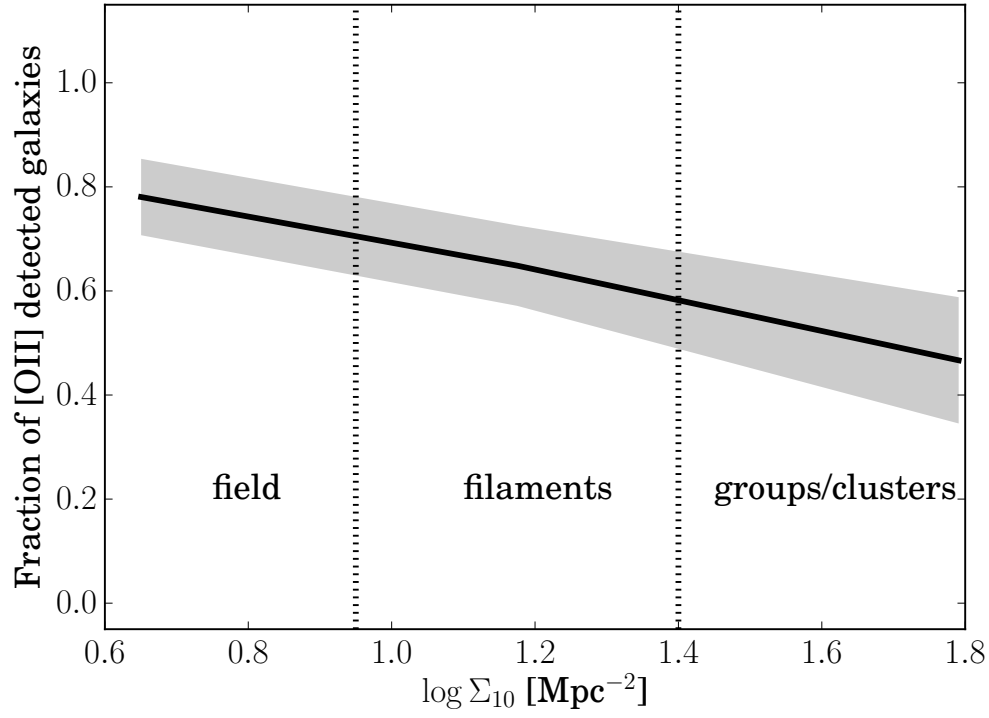


Figure 5.10 – Fraction of [OII] detected galaxies as a function of the local density Σ_{10} . The dotted vertical lines are the bins edges ($\log \Sigma_{10} = 0.95, 1.4 [\text{Mpc}^{-2}]$), separating the density field between field galaxies, filaments and groups/clusters.

line is the detection limit of [OII]. The red sequence members are in red. We see that the two criteria are in good agreement. Out of the 33 red sequence members, only 4 have a detected [OII] and out of the 94 non members, 7 are below the [OII] detection limit. Stated otherwise, 12 % of the red sequence members are in fact star-forming, while 7 % of the non-members have undetected star formation.

This implies that the results relying on the red sequence membership should remain true for the spectroscopic sample with the [OII] criterion instead. This is indeed confirmed by Fig. 5.10 and 5.11. On Fig. 5.10, we show the fraction of [OII] detected galaxies as a function of the local density. The sample is split in 3 density bins, with the same edges as the ones used to separate between field, filaments and cluster in Section 4.1. Similarly to Fig. 4.6, we see that the fraction of [OII] detected galaxies decreases as the density increases. This is a confirmation that significant quenching processes are already present in the filament environment. If we split the sample depending on whether the local density is lower or higher than the global one (Fig. 5.11), we observe that [OII] is more likely to be detected if the local density is lower than the global one. This is similar to Fig. 4.15, excepted that the statement holds for the whole density range (although the error bars partially overlap), while for Fig. 4.15 it concerned only the high densities. It confirms that the quenching of galaxies is more strongly influenced by the local environment than the global one.

5.5.3 Star formation rates in the large scale structures

Fig. 5.12 shows the SFR of the CL1411.1-1148 members as a function of the local density. The SFR of the galaxies with undetected [OII] line is set to 0 (even if in reality they have low, undetected SFR). The dotted vertical lines are the bins edges, separating the density field between field galaxies, filaments and groups/clusters. The solid line is the median SFR of star-forming galaxies (i.e., with detected [OII]) and the grey envelope encompasses the 25th and 75th percentiles.

We see that in the groups/cluster environment, there are no galaxies with $\text{SFR} > 2M_{\odot}/\text{yr}$, while in the lower density environments, a significant fraction of galaxies are forming stars above this threshold. It means that not only the fraction of star-forming galaxies is lower in the groups/cluster environment (see Fig. 5.10), but also that the SFR itself is decreased in this environment. It is confirmed by the decrease of the median SFR (in blue) in the groups/cluster environment. Even if in this environment the number of spectra is low, the difference in the distributions of the SFR is statistically significant, as a Kolmogorov-Smirnov test yields a p -value of 0.13 that the SFR distributions of the groups/cluster environment and the filament environment have the same parent distribution¹.

On Fig. 5.13, we show the position of the FORS2 and VIMOS cluster members, with a color code for their SFR. The black circles are the groups identified in Fig. 5.8. We see that these

¹ The likelihood that the SFR of the filament and field environments are drawn from the same distribution is high, as the p -value in this case is 0.60.

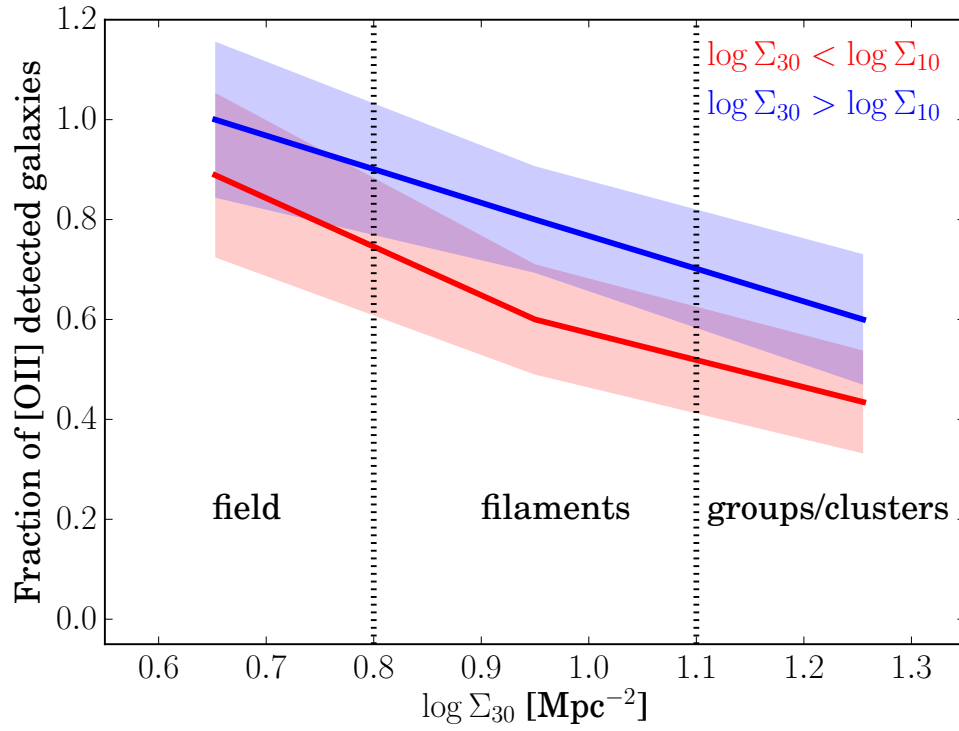


Figure 5.11 – Fraction of [OII] detected galaxies as a function of the global density Σ_{30} . The dotted vertical lines are the bins edges ($\log \Sigma_{30} = 0.8, 1.1 [\text{Mpc}^{-2}]$), separating the density field between field galaxies, filaments and groups/clusters.

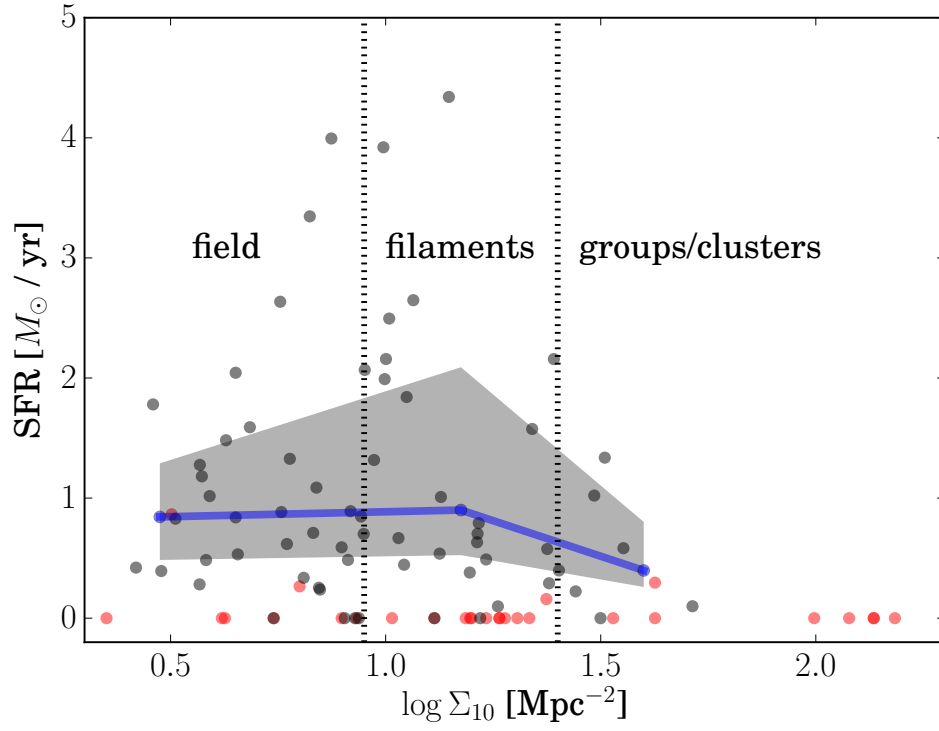


Figure 5.12 – SFR a function of the local density. Red dots are the red sequence members, black dots are the red sequence non-members. The solid line is the median SFR of the star-forming galaxies ($W_{\text{OII}} < -5 \text{ \AA}$) and the grey envelopes encompass the 25th and 75th percentiles. The dotted vertical lines are the bins edges ($\log \Sigma_{10} = 0.95, 1.4 \text{ [Mpc}^{-2}]$), separating the density field between field galaxies, filaments and groups/clusters.

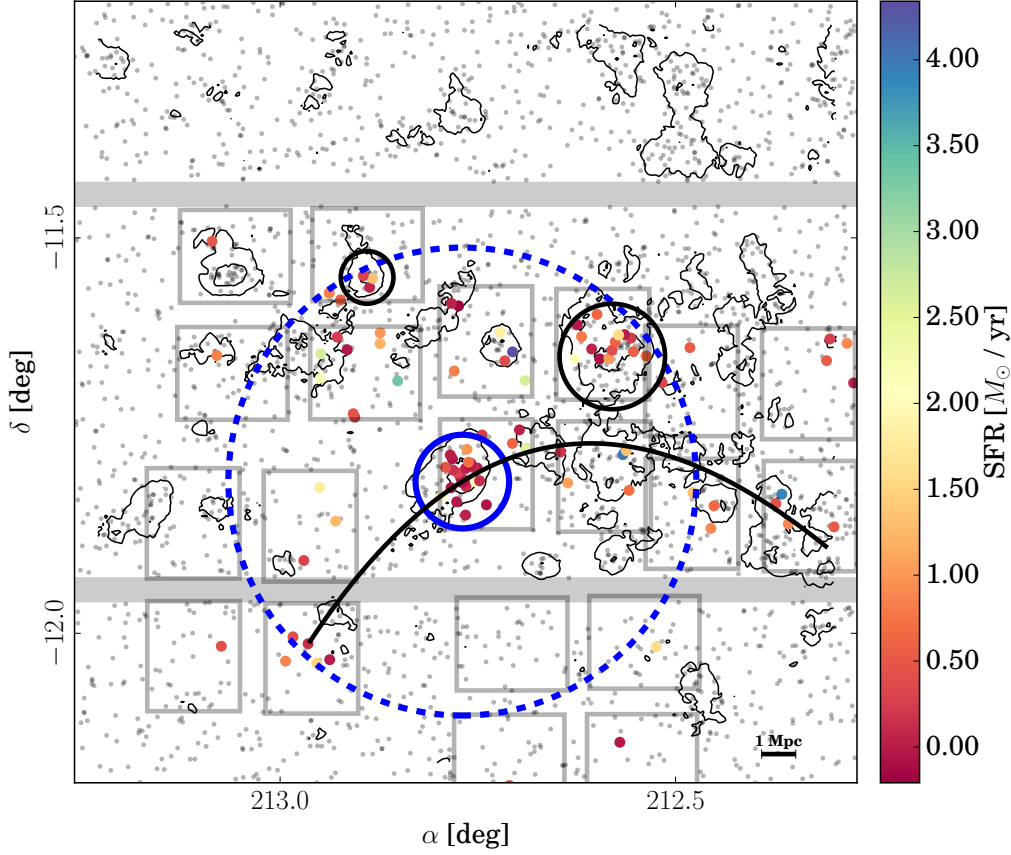


Figure 5.13 – Position of the FORS2 and VIMOS cluster members, with a color code for their SFR. The light black dots are the *photo-z* selected large scale structures members. The thin black lines are the density thresholds ($\log \Sigma_{10} = 0.95, 1.4 \text{ [Mpc}^{-2}]$) separating the density field between field galaxies, filaments and groups/clusters. The thick black line and circles highlight regions of interest (see Section 5.5.1). The blue circles show 1 and 5 R_{200} , the black circles are the groups identified in Fig. 5.8 and the grey bands are the MegaCam large CCD gaps.

groups (and CL1411.1-1148 itself) have a low fraction of star-forming galaxies. It increases their likelihood to be bound structures, in which strong quenching mechanisms already happened. In the “filament” (solid black curve), the fraction of SF galaxies is higher than in the highest density structures, although the limited sampling makes it difficult to know whether it contains substructures of quenched galaxies.

5.6 Summary and discussion

This chapter essentially confirms the photometry based results, with a few new aspects:

- Section 5.4: the accuracy of the *photo-z* calibrated on FORS2 and LDP is confirmed by the VIMOS data ($\text{median}(\Delta z) < 0.01$, $\sigma_z \lesssim 0.04$, $f_{\text{outliers}} \sim 2\%$). We detected a secondary

structure at $z = 0.49$ that we call CL1411.1-1148a. If we take into account this structure, the global success rate for the selection of galaxies close to the cluster redshift is 36 % and reaches 63 % in the highest density regions. Showing the great efficiency of our *photo-z* based target selection.

- Section 5.5.1: Adding the full spectroscopic information in the density maps does not imply dramatic changes in the shape of the maps. 2 groups at the cluster redshift emerge from the spectroscopy, plus another one at 0.49. We identify a possible filament or wall, passing through CL1411.1-1148.
- Section 5.5.2: The fraction of [OII] detected galaxies is lower in denser environments. The local density has a larger influence on this fraction than the global one. These results are compatible with the conclusions drawn in the previous chapter, based on the red sequence membership.
- Section 5.5.3: The fraction of quenched galaxies in the structures highlighted in Section 5.5.1 is high, increasing their likelihood to be gravitationally bound groups in which quenching mechanisms happened.

Our SFR distribution as a function of the local density (Fig. 5.12) is qualitatively similar to the one of Poggianti et al. (2008) and Vulcani et al. (2010), which are based on the EDisCS clusters up to $\sim 2R_{200}$, and Wolf et al. (2009), which studies the A901/2 cluster complex at $z \sim 0.17$. They also see a decrease of the mean SFR in the highest densities. These results may seem in contradiction with Peng et al. (2010) and Wijesinghe et al. (2012), who do not see any correlation between SFR and density. Nevertheless their study are not focused on clusters, so their sample is mostly composed of field galaxies. Another difference arising from these two set of studies is that the first ones use photometric samples to define the density fields, while the second ones are only based on spectroscopy. The latter could therefore undersample the highest density regions compared to the deeper photometric studies, implying an underestimation of the highest densities and a disappearance of the correlation with the SFR.

Even if our statistics is limited, one could argue that our results are compatible with both results. In the field and filament environment, there is no correlation between SFR and density. These density ranges correspond to the wide field studies of (e.g., Peng et al. 2010; Wijesinghe et al. 2012), who observe the same lack of correlation. On the other hand, we see a decrease of SFR with density in the high density regime, which is the dominant environment in Poggianti et al. (2008), Wolf et al. (2009) and Vulcani et al. (2010), who also notice this decrease.

6 Conclusions

The exact influence of the environment on galaxy evolution is an open question. The contributions of the different physical interactions transforming the properties of galaxies, as well as the time and location at which they operate dominantly are still unknown. Existing studies at intermediate redshift, an epoch when these phenomena are expected to be very active, around galaxy clusters are limited, mostly because they are focused on too massive clusters, which are evolved systems which are not representative of the typical clusters. EDisCS is the only rich dataset targeting clusters which are likely progenitors of the clusters observed today, however the observations were so far concentrated on the clusters core. In this thesis a few of the EDisCS clusters were selected and observed over a wide field, with the aim to follow the fate of galaxies along the different structures feeding the central cluster.

Our observational strategy is described in details in Chapter 2. Deep optical imaging (down to $r = 23$) in the u , g , r , i and z filters with the 3.6 meters of diameter Canada-France-Hawaii Telescope was gathered by the MegaCam instrument (1 deg² field of view, almost 380 megapixels). The filter set was chosen for an optimal computation of photometric redshifts, to be able to map the LSS around the clusters. The datasets are complete for 2 fields, containing 3 clusters (CL1301.7-1139a, CL1301.7-1139, CL1411.1-1148) with velocity dispersions $v_{cl} \sim 500$ -700 km/s at redshifts $z \sim 0.40$ -0.52. The redshift range and masses of the clusters, combined to wide field of MegaCam (the FoV corresponds to a projected radius of 8 to 13 R_{200}) makes this study unique.

The characterization of the images (noise properties, depth, completeness) and physical measurements extracted from the data are described in Chapter 3. Photometric redshifts were computed with the EAZY code, with a very competitive accuracy ($\sigma_{NMAD} \lesssim 0.04$) compared to other surveys using a comparable filter set, and stellar masses were derived with FAST (the 90 % completeness limit is $M_* \sim 2 \cdot 10^{10} M_{\odot}$). The projected number density of galaxies in circular apertures (Σ_N) were considered as a proxy to measure the density in the LSS. A global density measure, based on the 30 nearest neighbors of each galaxy, served to identify the field ($\log \Sigma_{30} < 0.8$ [Mpc⁻²]), filaments ($0.8 < \log \Sigma_{30} < 1.1$ [Mpc⁻²]) and groups/clusters (1.1 [Mpc⁻²] $< \log \Sigma_{30}$). A local measure, based this time on the 10 nearest neighbors, was

employed to be more sensitive to small scale interactions and highlight substructures within the structures defined by the global density field.

The physical analysis of the photometry is detailed in Chapter 4. Maps of the local (Σ_{10}) and global density (Σ_{30}) of galaxies with *photo-z* close to the cluster redshift (z_{phot} within $z_{\text{cl}} \pm z_{\text{cl}}(1 + z_{\text{cl}})\sigma_{\text{NMAD}}$) in each field are presented, showing clearly a lack of circular symmetry around each cluster. In each map, several groups candidates (identified as strong overdensities) were detected, as well as filamentary structures connecting them. We studied the fraction of quiescent galaxies (using the red sequence membership as a proxy) in the different environments, showing that it decreases with growing density already within filaments. Even if the stellar mass seems to play a major role to predict whether a galaxy is star forming or not, the density is still influential. For less massive galaxies, the correlation between the fraction of red sequence galaxies and density increases. In filaments and groups/clusters, the fraction of red sequence galaxies is higher if the local density is higher than the global one, implying that the local environment of galaxies is more influential than the global one.

Our spectroscopic campaign, whose goal is to provide high accuracy redshifts to confirm the existence of the structures identified in photometry and measure the properties of galaxies such as SFR and metallicity, is presented in Chapter 5. We obtained medium resolution optical spectra with the VLT/VIMOS instrument for the CL1411.1-1148 field. The 392 redshifts derived (with errors in majority below 100 km/s) form a distribution with two strong peaks. The main one lies as expected at the cluster redshift ($z \sim 0.52$) and the secondary one, named CL1411.1-1148a, is centered at $z \sim 0.49$. We considered that galaxies are members of the CL1411.1-1148 (CL1411.1-1148a) structure if z_{spec} is within $4 \nu_{\text{cl}}$ of z_{cl} (0.49 ± 0.015). This criterion was chosen to separate unambiguously the two structures in redshift space. Note that they are impossible to disentangle with photometric redshifts alone. The majority ($\sim 70\%$) of the structures detected with the *photo-z* were confirmed (excluding the regions at $z \sim 0.49$): the photometric identification is trustworthy. Although our spectroscopic sample is of good size, the sampling was not sufficient to derive robust estimates of the velocity dispersions of the infalling groups.

In the spectroscopic analysis of the properties of galaxies, we found that the fraction of galaxies with a detected [OII] emission line (a tracer of the SFR) is smaller with increasing density, also already at the filament level. These results essentially confirmed the photometric ones. We also found that the star formation rate, determined from [OII], is in average weaker in groups and clusters than in lower density environments.

This thesis should be seen as a pioneer work highlighting the effects of the Cosmic Web on galaxy evolution. For the first time, large scale structure around medium mass galaxies clusters were analyzed systematically up to large cluster-centric distances. The crucial importance to use the full spatial distribution of galaxies to understand their evolution has been demonstrated, as opposed to a simple cluster-centric or purely density-based analysis. We showed that the local environment of galaxies plays a stronger role on galaxy properties than the global

one, meaning in particular that cluster-galaxy interactions are not dominant in galaxy evolution. Conversely, we observed that galaxies in different global environments have distinct behaviors. The population of galaxies in filaments is not the same as in clusters or the field.

More broadly, the results of this thesis imply that galaxies within filaments do not evolve passively until reaching the cluster. They interact each other and form groups, which trigger deep modifications of their properties. It means that a full understanding of the influence of the environment on galaxy evolution is only possible with a detailed analysis of the evolution of galaxies within filaments.

Finally, the detection of filaments using galaxies as tracers can complement other methods to identify the LSS, such as weak lensing (e.g., Jauzac et al. 2012). Altogether, it will allow to constrain more accurately the models of structure formation and how baryonic matter populates the dark matter haloes.

6.1 Future work

The possibilities to complement and strengthen this study are manifold. We present here a few of them, some are already ongoing, while others rely on existing instruments and methods and will be started soon.

During the last two months, we received the u -band observations of CL1018.8-1211, completing the photometric dataset for this cluster. We can therefore perform the same photometric analysis as for the CL1301.7-1139 and CL1411.1-1148 fields, to put our results on a firm and even more general basis, free of cosmic variance. In the period, the missing VIMOS field (see Fig. 5.1) has also been observed and hundreds of medium resolution spectra were obtained with Magellan/IMACS for the CL1301.7-1139 field. It will largely boost the statistics of the spectroscopic results. K_s -band observations with CFHT/WIRCam were also collected. They will improve the stellar mass estimations and serve to disentangle dust reddened star forming galaxies from red metal-rich galaxies, since redder bands are less sensitive to the dust extinction.

The *photo-z* could be enhanced in two ways. The obvious one is to observe the clusters in more bands, to help the SED fitting from EAZY. The other one is purely technical: the seeing-matching for the aperture matched photometry degrades significantly the quality of the photometry. A possible improvement would be to model the total magnitude of each galaxy in each band, taking into account the local PSF. However, it requires an important computing power and it is unclear whether the improvement of the accuracy would be significant.

New observations have been accepted with a narrow band centered on $H\alpha$ with the OSIRIS instrument. It will allow an analysis of SFR properties of a much larger sample than with spectroscopy alone. As a by-product, it will also yield redshifts for the $H\alpha$ emitters with an accuracy approximately 10 times better than with *photo-z* and 10 times worse than with the

medium resolution spectroscopy.

The spectroscopy has not yet been fully exploited. We focused on the [OII] line, but other lines and indices are measurable, e.g. the strength of the 4000 Å spectral break and H_δ (age indicators for the stellar populations of galaxies). We could estimate as well the dust content of the galaxies, their metallicity and spectral type. More spectroscopy is also underway with Gemini/GMOS, with an observational strategy strengthened by the experience gained with this thesis. It will also allow a 3D view of the LSS (instead of projected), providing a detailed description of the LSS (velocity dispersion of the substructures, better determination of shape of the filaments, etc.).

Comparisons with cosmological simulations would increase our understanding of the observed structures. We could test how projection effects may bias the density maps. We could also estimate the likelihood to observe our detected LSS, i.e. if their shape, size and number are typical in simulations.

A morphology based analysis will also add a new dimension to the analysis. The resolution of ground-based images at these redshifts severely limits the accuracy of the classification. We numerically increased the resolution of the images, up to a quality close to the Hubble Space Telescope, with the help of the new deconvolution algorithm FIREDEC (Cantale et al. 2015, in prep). We only need to identify the morphology of the deconvolved galaxies.

6.2 Outlook

The upcoming surveys (LSST, BigBOSS, DES, etc.) will allow to extend the results of this thesis over unprecedented scales. As an example, the medium class space satellite Euclid, planned to be launched in 2020, will observe billions of galaxies in the optical and the near-infrared over the whole sky, with tens of millions of spectroscopic redshifts. The mapping of the LSS will be exquisite. Hundreds of clusters will be detected at intermediate redshift, as well as the filaments connecting them. The Square Kilometer Array, an array of thousands of radio telescope that will extend over thousands of kilometers in Africa and Australia, will also detect the LSS, using as a tracer the neutral hydrogen. The synergy of all those surveys will undoubtedly further unveil the mysteries concerning the influence of the environment on the stellar populations, morphology and gas content of galaxies.

Bibliography

- S. Arnouts, S. Cristiani, L. Moscardini, S. Matarrese, F. Lucchin, A. Fontana, and E. Giallongo. Measuring and modelling the redshift evolution of clustering: the Hubble Deep Field North. *MNRAS*, 310:540–556, December 1999. doi: 10.1046/j.1365-8711.1999.02978.x.
- Y. M. Bahé and I. G. McCarthy. Star formation quenching in simulated group and cluster galaxies: when, how, and why? *MNRAS*, 447:969–992, February 2015. doi: 10.1093/mnras/stu2293.
- I. K. Baldry, M. L. Balogh, R. G. Bower, K. Glazebrook, R. C. Nichol, S. P. Bamford, and T. Budavari. Galaxy bimodality versus stellar mass and environment. *MNRAS*, 373:469–483, December 2006. doi: 10.1111/j.1365-2966.2006.11081.x.
- N. Benítez. Bayesian Photometric Redshift Estimation. *ApJ*, 536:571–583, June 2000. doi: 10.1086/308947.
- E. Bertin and S. Arnouts. SExtractor: Software for source extraction. *A&AS*, 117:393–404, June 1996.
- E. Bertin, Y. Mellier, M. Radovich, G. Missonnier, P. Didelon, and B. Morin. The TERAPIX Pipeline. In D. A. Bohlender, D. Durand, and T. H. Handley, editors, *Astronomical Data Analysis Software and Systems XI*, volume 281 of *Astronomical Society of the Pacific Conference Series*, page 228, 2002.
- M. R. Blanton and A. A. Berlind. What Aspects of Galaxy Environment Matter? *ApJ*, 664: 791–803, August 2007. doi: 10.1086/512478.
- M. Bolzonella, J.-M. Miralles, and R. Pelló. Photometric redshifts based on standard SED fitting procedures. *A&A*, 363:476–492, November 2000.
- D. Bottini, B. Garilli, D. Maccagni, L. Tresse, V. Le Brun, O. Le Fèvre, J. P. Picat, R. Scaramella, M. Scodeggio, G. Vettolani, A. Zanichelli, C. Adami, M. Arnaboldi, S. Arnouts, S. Bardelli, M. Bolzonella, A. Cappi, S. Charlot, P. Ciliegi, T. Contini, S. Foucaud, P. Franzetti, L. Guzzo, O. Ilbert, A. Iovino, H. J. McCracken, B. Marano, C. Marinoni, G. Mathez, A. Mazure, B. Meneux, R. Merighi, S. Paltani, A. Pollo, L. Pozzetti, M. Radovich, G. Zamorani, and E. Zucca. The Very Large Telescope Visible Multi-Object Spectrograph Mask Preparation Software. *PASP*, 117:996–1103, September 2005. doi: 10.1086/432150.

Bibliography

- O. Boulade, X. Charlot, P. Abbon, S. Aune, P. Borgeaud, P.-H. Carton, M. Carty, J. Da Costa, H. Deschamps, D. Desforge, D. Eppell , P. Gallais, L. Gosset, R. Granelli, M. Gros, J. de Kat, D. Loiseau, J.-. Ritou, J. Y. Rouss , P. Starzynski, N. Vignal, and L. G. Vigroux. MegaCam: the new Canada-France-Hawaii Telescope wide-field imaging camera. In M. Iye and A. F. M. Moorwood, editors, *Instrument Design and Performance for Optical/Infrared Ground-based Telescopes*, volume 4841 of *Society of Photo-Optical Instrumentation Engineers (SPIE) Conference Series*, pages 72–81, March 2003. doi: 10.1117/12.459890.
- G. B. Brammer, P. G. van Dokkum, and P. Coppi. EAZY: A Fast, Public Photometric Redshift Code. *ApJ*, 686:1503–1513, October 2008. doi: 10.1086/591786.
- J. A. Cardelli, G. C. Clayton, and J. S. Mathis. The relationship between infrared, optical, and ultraviolet extinction. *ApJ*, 345:245–256, October 1989. doi: 10.1086/167900.
- M. Carrasco Kind and R. J. Brunner. TPZ: photometric redshift PDFs and ancillary information by using prediction trees and random forests. *MNRAS*, 432:1483–1501, June 2013. doi: 10.1093/mnras/stt574.
- G. Chabrier. Galactic Stellar and Substellar Initial Mass Function. *PASP*, 115:763–795, July 2003. doi: 10.1086/376392.
- S. M. Chung, P. R. Eisenhardt, A. H. Gonzalez, S. A. Stanford, M. Brodwin, D. Stern, and T. Jarrett. A WISE View of Star Formation in Local Galaxy Clusters. *ApJ*, 743:34, December 2011. doi: 10.1088/0004-637X/743/1/34.
- A. A. Collister and O. Lahav. ANNz: Estimating Photometric Redshifts Using Artificial Neural Networks. *PASP*, 116:345–351, April 2004. doi: 10.1086/383254.
- G. De Lucia, B. M. Poggianti, A. Arag n-Salamanca, D. Clowe, C. Halliday, P. Jablonka, B. Milvang-Jensen, R. Pell , S. Poirier, G. Rudnick, R. Saglia, L. Simard, and S. D. M. White. The Buildup of the Red Sequence in Galaxy Clusters since $z \sim 0.8$. *ApJL*, 610:L77–L80, August 2004. doi: 10.1086/423373.
- G. De Lucia, A. Muzzin, and S. Weinmann. What Regulates Galaxy Evolution? Open questions in our understanding of galaxy formation and evolution. *New Astronomy Reviews*, 62:1–14, October 2014. doi: 10.1016/j.newar.2014.08.001.
- V. Desai, J. J. Dalcanton, A. Arag n-Salamanca, P. Jablonka, B. Poggianti, S. M. Gogarten, L. Simard, B. Milvang-Jensen, G. Rudnick, D. Zaritsky, D. Clowe, C. Halliday, R. Pell , R. Saglia, and S. White. The Morphological Content of 10 EDisCS Clusters at $0.5 < z < 0.8$. *ApJ*, 660: 1151–1164, May 2007. doi: 10.1086/513310.
- A. Dressler. Galaxy morphology in rich clusters - Implications for the formation and evolution of galaxies. *ApJ*, 236:351–365, March 1980. doi: 10.1086/157753.
- H. Ebeling, E. Barrett, D. Donovan, C.-J. Ma, A. C. Edge, and L. van Speybroeck. A Complete Sample of 12 Very X-Ray Luminous Galaxy Clusters at $z > 0.5$. *ApJL*, 661:L33–L36, May 2007. doi: 10.1086/518603.

- R. A. Finn, D. Zaritsky, D. W. McCarthy, Jr., B. Poggianti, G. Rudnick, C. Halliday, B. Milvang-Jensen, R. Pelló, and L. Simard. $H\alpha$ -derived Star Formation Rates for Three $z\sim 0.75$ EDisCS Galaxy Clusters. *ApJ*, 630:206–227, September 2005. doi: 10.1086/431642.
- R. A. Finn, V. Desai, G. Rudnick, B. Poggianti, E. F. Bell, J. Hinz, P. Jablonka, B. Milvang-Jensen, J. Moustakas, K. Rines, and D. Zaritsky. Dust-obscured Star Formation in Intermediate Redshift Galaxy Clusters. *ApJ*, 720:87–98, September 2010. doi: 10.1088/0004-637X/720/1/87.
- W. Freudling, M. Romaniello, D. M. Bramich, P. Ballester, V. Forchi, C. E. García-Dabó, S. Moehler, and M. J. Neeser. Automated data reduction workflows for astronomy. The ESO Reflex environment. *A&A*, 559:A96, November 2013. doi: 10.1051/0004-6361/201322494.
- M. Fukugita, K. Shimasaku, and T. Ichikawa. Galaxy Colors in Various Photometric Band Systems. *PASP*, 107:945, October 1995. doi: 10.1086/133643.
- M. Girardi and M. Mezzetti. Evolution of the Internal Dynamics of Galaxy Clusters. *ApJ*, 548: 79–96, February 2001. doi: 10.1086/318665.
- P. L. Gómez, R. C. Nichol, C. J. Miller, M. L. Balogh, T. Goto, A. I. Zabludoff, A. K. Romer, M. Bernardi, R. Sheth, A. M. Hopkins, F. J. Castander, A. J. Connolly, D. P. Schneider, J. Brinkmann, D. Q. Lamb, M. SubbaRao, and D. G. York. Galaxy Star Formation as a Function of Environment in the Early Data Release of the Sloan Digital Sky Survey. *ApJ*, 584: 210–227, February 2003. doi: 10.1086/345593.
- A. H. Gonzalez, D. Zaritsky, J. J. Dalcanton, and A. Nelson. The Las Campanas Distant Cluster Survey: The Catalog. *ApJS*, 137:117–138, November 2001. doi: 10.1086/322541.
- T. Goto, R. C. Nichol, S. Okamura, M. Sekiguchi, C. J. Miller, M. Bernardi, A. Hopkins, C. Tremonti, A. Connolly, F. J. Castander, J. Brinkmann, M. Fukugita, M. Harvanek, Z. Ivezic, S. J. Kleinman, J. Krzesinski, D. Long, J. Loveday, E. H. Neilsen, P. R. Newman, A. Nitta, S. A. Snedden, and M. Subbarao. $H\delta$ -Strong Galaxies in the Sloan Digital Sky Survey: I. The Catalog. *PASJ*, 55:771–787, June 2003. doi: 10.1093/pasj/55.4.771.
- J. E. Gunn and J. R. Gott, III. On the Infall of Matter Into Clusters of Galaxies and Some Effects on Their Evolution. *ApJ*, 176:1, August 1972. doi: 10.1086/151605.
- C. P. Haines, A. Gargiulo, F. La Barbera, A. Mercurio, P. Merluzzi, and G. Busarello. The different physical mechanisms that drive the star formation histories of giant and dwarf galaxies. *MNRAS*, 381:7–32, October 2007. doi: 10.1111/j.1365-2966.2007.12189.x.
- C. Halliday, B. Milvang-Jensen, S. Poirier, B. M. Poggianti, P. Jablonka, A. Aragón-Salamanca, R. P. Saglia, G. De Lucia, R. Pelló, L. Simard, D. I. Clowe, G. Rudnick, J. J. Dalcanton, S. D. M. White, and D. Zaritsky. Spectroscopy of clusters in the ESO Distant Cluster Survey (EDisCS). Redshifts, velocity dispersions and substructure for 5 clusters. *A&A*, 427:397–413, November 2004. doi: 10.1051/0004-6361:20041304.

Bibliography

- H. Hildebrandt, T. Erben, K. Kuijken, L. van Waerbeke, C. Heymans, J. Coupon, J. Benjamin, C. Bonnett, L. Fu, H. Hoekstra, T. D. Kitching, Y. Mellier, L. Miller, M. Velander, M. J. Hudson, B. T. P. Rowe, T. Schrabback, E. Semboloni, and N. Benítez. CFHTLenS: improving the quality of photometric redshifts with precision photometry. *MNRAS*, 421:2355–2367, April 2012. doi: 10.1111/j.1365-2966.2012.20468.x.
- D. W. Hogg, M. R. Blanton, J. Brinchmann, D. J. Eisenstein, D. J. Schlegel, J. E. Gunn, T. A. McKay, H.-W. Rix, N. A. Bahcall, J. Brinkmann, and A. Meiksin. The Dependence on Environment of the Color-Magnitude Relation of Galaxies. *ApJL*, 601:L29–L32, January 2004. doi: 10.1086/381749.
- O. Ilbert, S. Arnouts, H. J. McCracken, M. Bolzonella, E. Bertin, O. Le Fèvre, Y. Mellier, G. Zamorani, R. Pellò, A. Iovino, L. Tresse, V. Le Brun, D. Bottini, B. Garilli, D. Maccagni, J. P. Picat, R. Scaramella, M. Scodeggio, G. Vettolani, A. Zanichelli, C. Adami, S. Bardelli, A. Cappi, S. Charlot, P. Ciliegi, T. Contini, O. Cucciati, S. Foucaud, P. Franzetti, I. Gavignaud, L. Guzzo, B. Marano, C. Marinoni, A. Mazure, B. Meneux, R. Merighi, S. Paltani, A. Pollo, L. Pozzetti, M. Radovich, E. Zucca, M. Bondi, A. Bongiorno, G. Busarello, S. de La Torre, L. Gregorini, F. Lamareille, G. Mathez, P. Merluzzi, V. Ripepi, D. Rizzo, and D. Vergani. Accurate photometric redshifts for the CFHT legacy survey calibrated using the VIMOS VLT deep survey. *A&A*, 457:841–856, October 2006. doi: 10.1051/0004-6361:20065138.
- O. Ilbert, H. J. McCracken, O. Le Fèvre, P. Capak, J. Dunlop, A. Karim, M. A. Renzini, K. Caputi, S. Boissier, S. Arnouts, H. Aussel, J. Comparat, Q. Guo, P. Hudelot, J. Kartaltepe, J. P. Kneib, J. K. Krogager, E. Le Floch, S. Lilly, Y. Mellier, B. Milvang-Jensen, T. Moutard, M. Onodera, J. Richard, M. Salvato, D. B. Sanders, N. Scoville, J. D. Silverman, Y. Taniguchi, L. Tasca, R. Thomas, S. Toft, L. Tresse, D. Vergani, M. Wolk, and A. Zirm. Mass assembly in quiescent and star-forming galaxies since $z \sim 4$ from UltraVISTA. *A&A*, 556:A55, August 2013. doi: 10.1051/0004-6361/201321100.
- M. Jauzac, E. Jullo, J.-P. Kneib, H. Ebeling, A. Leauthaud, C.-J. Ma, M. Limousin, R. Massey, and J. Richard. A weak lensing mass reconstruction of the large-scale filament feeding the massive galaxy cluster MACS J0717.5+3745. *MNRAS*, 426:3369–3384, November 2012. doi: 10.1111/j.1365-2966.2012.21966.x.
- S. Jester, D. P. Schneider, G. T. Richards, R. F. Green, M. Schmidt, P. B. Hall, M. A. Strauss, D. E. Vanden Berk, C. Stoughton, J. E. Gunn, J. Brinkmann, S. M. Kent, J. A. Smith, D. L. Tucker, and B. Yanny. The Sloan Digital Sky Survey View of the Palomar-Green Bright Quasar Survey. *AJ*, 130:873–895, September 2005. doi: 10.1086/432466.
- H. L. Johnson and W. W. Morgan. Fundamental stellar photometry for standards of spectral type on the revised system of the Yerkes spectral atlas. *ApJ*, 117:313, May 1953. doi: 10.1086/145697.
- G. Kauffmann, S. D. M. White, T. M. Heckman, B. Ménard, J. Brinchmann, S. Charlot, C. Tremonti, and J. Brinkmann. The environmental dependence of the relations between

- stellar mass, structure, star formation and nuclear activity in galaxies. *MNRAS*, 353:713–731, September 2004. doi: 10.1111/j.1365-2966.2004.08117.x.
- R. C. Kennicutt, Jr. Star Formation in Galaxies Along the Hubble Sequence. *ARAA*, 36:189–232, 1998. doi: 10.1146/annurev.astro.36.1.189.
- C. Knobel, S. J. Lilly, A. Iovino, K. Kovač, T. J. Bschorr, V. Presotto, P. A. Oesch, P. Kampczyk, C. M. Carollo, T. Contini, J.-P. Kneib, O. Le Fevre, V. Mainieri, A. Renzini, M. Scodeggio, G. Zamorani, S. Bardelli, M. Bolzonella, A. Bongiorno, K. Caputi, O. Cucciati, S. de la Torre, L. de Ravel, P. Franzetti, B. Garilli, F. Lamareille, J.-F. Le Borgne, V. Le Brun, C. Maier, M. Mignoli, R. Pello, Y. Peng, E. Perez Montero, J. Silverman, M. Tanaka, L. Tasca, L. Tresse, D. Vergani, E. Zucca, L. Barnes, R. Bordoloi, A. Cappi, A. Cimatti, G. Coppa, A. M. Koekemoer, C. López-Sanjuan, H. J. McCracken, M. Moresco, P. Nair, L. Pozzetti, and N. Welikala. The zCOSMOS 20k Group Catalog. *ApJ*, 753:121, July 2012. doi: 10.1088/0004-637X/753/2/121.
- T. Kodama, I. Smail, F. Nakata, S. Okamura, and R. G. Bower. The Transformation of Galaxies within the Large-Scale Structure around a $z=0.41$ Cluster. *ApJL*, 562:L9–L13, November 2001. doi: 10.1086/338100.
- T. Kodama, M. L. Balogh, I. Smail, R. G. Bower, and F. Nakata. A panoramic $H\alpha$ imaging survey of the $z=0.4$ cluster Cl0024.0+1652 with Subaru. *MNRAS*, 354:1103–1119, November 2004. doi: 10.1111/j.1365-2966.2004.08271.x.
- K. Kovač, S. J. Lilly, C. Knobel, T. J. Bschorr, Y. Peng, C. M. Carollo, T. Contini, J.-P. Kneib, O. Le Févre, V. Mainieri, A. Renzini, M. Scodeggio, G. Zamorani, S. Bardelli, M. Bolzonella, A. Bongiorno, K. Caputi, O. Cucciati, S. de la Torre, L. de Ravel, P. Franzetti, B. Garilli, A. Iovino, P. Kampczyk, F. Lamareille, J.-F. Le Borgne, V. Le Brun, C. Maier, M. Mignoli, P. Oesch, R. Pello, E. P. Montero, V. Presotto, J. Silverman, M. Tanaka, L. Tasca, L. Tresse, D. Vergani, E. Zucca, H. Aussel, A. M. Koekemoer, E. Le Floch, M. Moresco, and L. Pozzetti. zCOSMOS 20k: satellite galaxies are the main drivers of environmental effects in the galaxy population at least to $z \sim 0.7$. *MNRAS*, 438:717–738, February 2014. doi: 10.1093/mnras/stt2241.
- Y. Koyama, T. Kodama, K. Shimasaku, S. Okamura, M. Tanaka, H. M. Lee, M. Im, H. Matsuhara, T. Takagi, T. Wada, and S. Oyabu. Mapping dusty star formation in and around a cluster at $z = 0.81$ by wide-field imaging with AKARI. *MNRAS*, 391:1758–1770, December 2008. doi: 10.1111/j.1365-2966.2008.13931.x.
- M. Kriek, P. G. van Dokkum, I. Labbé, M. Franx, G. D. Illingworth, D. Marchesini, and R. F. Quadri. An Ultra-Deep Near-Infrared Spectrum of a Compact Quiescent Galaxy at $z = 2.2$. *ApJ*, 700:221–231, July 2009. doi: 10.1088/0004-637X/700/1/221.
- M. J. Kurtz and D. J. Mink. RVSAO 2.0: Digital Redshifts and Radial Velocities. *PASP*, 110: 934–977, August 1998. doi: 10.1086/316207.
- I. Labbé, M. Franx, G. Rudnick, N. M. F. Schreiber, H.-W. Rix, A. Moorwood, P. G. van Dokkum, P. van der Werf, H. Röttgering, L. van Starckenburg, A. van der Wel, K. Kuijken, and E. Daddi.

Bibliography

- Ultradeep Near-Infrared ISAAC Observations of the Hubble Deep Field South: Observations, Reduction, Multicolor Catalog, and Photometric Redshifts. *AJ*, 125:1107–1123, March 2003. doi: 10.1086/346140.
- O. Le Fèvre, M. Saisse, D. Mancini, S. Brau-Nogue, O. Caputi, L. Castinel, S. D’Odorico, B. Garilli, M. Kissler-Patig, C. Lucuix, G. Mancini, A. Pauget, G. Sciarretta, M. Scodeggio, L. Tresse, and G. Vettolani. Commissioning and performances of the VLT-VIMOS instrument. In M. Iye and A. F. M. Moorwood, editors, *Instrument Design and Performance for Optical/Infrared Ground-based Telescopes*, volume 4841 of *Society of Photo-Optical Instrumentation Engineers (SPIE) Conference Series*, pages 1670–1681, March 2003. doi: 10.1117/12.460959.
- I. Lewis, M. Balogh, R. De Propris, W. Couch, R. Bower, A. Offer, J. Bland-Hawthorn, I. K. Baldry, C. Baugh, T. Bridges, R. Cannon, S. Cole, M. Colless, C. Collins, N. Cross, G. Dalton, S. P. Driver, G. Efstathiou, R. S. Ellis, C. S. Frenk, K. Glazebrook, E. Hawkins, C. Jackson, O. Lahav, S. Lumsden, S. Maddox, D. Madgwick, P. Norberg, J. A. Peacock, W. Percival, B. A. Peterson, W. Sutherland, and K. Taylor. The 2dF Galaxy Redshift Survey: the environmental dependence of galaxy star formation rates near clusters. *MNRAS*, 334:673–683, August 2002. doi: 10.1046/j.1365-8711.2002.05558.x.
- L. M. Lubin, R. R. Gal, B. C. Lemaux, D. D. Kocevski, and G. K. Squires. The Observations of Redshift Evolution in Large-Scale Environments (ORELSE) Survey. I. The Survey Design and First Results on CL 0023+0423 at $z = 0.84$ and RX J1821.6+6827 at $z = 0.82$. *AJ*, 137:4867–4883, June 2009. doi: 10.1088/0004-6256/137/6/4867.
- D. Marchesini, P. G. van Dokkum, N. M. Förster Schreiber, M. Franx, I. Labbé, and S. Wuyts. The Evolution of the Stellar Mass Function of Galaxies from $z = 4.0$ and the First Comprehensive Analysis of its Uncertainties: Evidence for Mass-Dependent Evolution. *ApJ*, 701:1765–1796, August 2009. doi: 10.1088/0004-637X/701/2/1765.
- S. L. McGee, M. L. Balogh, R. G. Bower, A. S. Font, and I. G. McCarthy. The accretion of galaxies into groups and clusters. *MNRAS*, 400:937–950, December 2009. doi: 10.1111/j.1365-2966.2009.15507.x.
- B. Milvang-Jensen, S. Noll, C. Halliday, B. M. Poggianti, P. Jablonka, A. Aragón-Salamanca, R. P. Saglia, N. Nowak, A. von der Linden, G. De Lucia, R. Pelló, J. Moustakas, S. Poirier, S. P. Bamford, D. I. Clowe, J. J. Dalcanton, G. H. Rudnick, L. Simard, S. D. M. White, and D. Zaritsky. Spectroscopy of clusters in the ESO distant cluster survey (EDisCS). II.. Redshifts, velocity dispersions, and substructure for clusters in the last 15 fields. *A&A*, 482:419–449, May 2008. doi: 10.1051/0004-6361:20079148.
- B. Moore, N. Katz, G. Lake, A. Dressler, and A. Oemler. Galaxy harassment and the evolution of clusters of galaxies. *Nature*, 379:613–616, February 1996. doi: 10.1038/379613a0.
- S. M. Moran, R. S. Ellis, T. Treu, G. P. Smith, R. M. Rich, and I. Smail. A Wide-Field Survey of Two $z \sim 0.5$ Galaxy Clusters: Identifying the Physical Processes Responsible for the Observed

- Transformation of Spirals into S0s. *ApJ*, 671:1503–1522, December 2007. doi: 10.1086/522303.
- A. Muzzin, G. Wilson, H. K. C. Yee, D. Gilbank, H. Hoekstra, R. Demarco, M. Balogh, P. van Dokkum, M. Franx, E. Ellingson, A. Hicks, J. Nantais, A. Noble, M. Lacy, C. Lidman, A. Rettura, J. Surace, and T. Webb. The Gemini Cluster Astrophysics Spectroscopic Survey (GCLASS): The Role of Environment and Self-regulation in Galaxy Evolution at $z \sim 1$. *ApJ*, 746:188, February 2012. doi: 10.1088/0004-637X/746/2/188.
- A. Oemler, Jr., A. Dressler, M. G. Gladders, J. R. Rigby, L. Bai, D. Kelson, E. Villanueva, J. Fritz, G. Rieke, B. M. Poggianti, and B. Vulcani. The IMACS Cluster Building Survey. I. Description of the Survey and Analysis Methods. *ApJ*, 770:61, June 2013. doi: 10.1088/0004-637X/770/1/61.
- J. B. Oke. Absolute Spectral Energy Distributions for White Dwarfs. *ApJS*, 27:21, February 1974. doi: 10.1086/190287.
- S. G. Patel, D. D. Kelson, B. P. Holden, G. D. Illingworth, M. Franx, A. van der Wel, and H. Ford. A Wide-Field Study of the $z \sim 0.8$ Cluster RX J0152.7-1357: The Role of Environment in the Formation of the Red Sequence. *ApJ*, 694:1349–1363, April 2009. doi: 10.1088/0004-637X/694/2/1349.
- R. Pelló, G. Rudnick, G. De Lucia, L. Simard, D. I. Clowe, P. Jablonka, B. Milvang-Jensen, R. P. Saglia, S. D. M. White, A. Aragón-Salamanca, C. Halliday, B. Poggianti, P. Best, J. Dalcanton, M. Dantel-Fort, B. Fort, A. von der Linden, Y. Mellier, H. Rottgering, and D. Zaritsky. Photometric redshifts and cluster tomography in the ESO Distant Cluster Survey. *A&A*, 508: 1173–1191, December 2009. doi: 10.1051/0004-6361/200810644.
- Y.-j. Peng, S. J. Lilly, K. Kovač, M. Bolzonella, L. Pozzetti, A. Renzini, G. Zamorani, O. Ilbert, C. Knobel, A. Iovino, C. Maier, O. Cucciati, L. Tasca, C. M. Carollo, J. Silverman, P. Kampczyk, L. de Ravel, D. Sanders, N. Scoville, T. Contini, V. Mainieri, M. Scodeggio, J.-P. Kneib, O. Le Fèvre, S. Bardelli, A. Bongiorno, K. Caputi, G. Coppia, S. de la Torre, P. Franzetti, B. Garilli, F. Lamareille, J.-F. Le Borgne, V. Le Brun, M. Mignoli, E. Perez Montero, R. Pello, E. Ricciardelli, M. Tanaka, L. Tresse, D. Vergani, N. Welikala, E. Zucca, P. Oesch, U. Abbas, L. Barnes, R. Bordoloi, D. Bottini, A. Cappi, P. Cassata, A. Cimatti, M. Fumana, G. Hasinger, A. Koekoer, A. Leauthaud, D. Maccagni, C. Marinoni, H. McCracken, P. Memeo, B. Meneux, P. Nair, C. Porciani, V. Presotto, and R. Scaramella. Mass and Environment as Drivers of Galaxy Evolution in SDSS and zCOSMOS and the Origin of the Schechter Function. *ApJ*, 721:193–221, September 2010. doi: 10.1088/0004-637X/721/1/193.
- Planck Collaboration, P. A. R. Ade, N. Aghanim, C. Armitage-Caplan, M. Arnaud, M. Ashdown, F. Atrio-Barandela, J. Aumont, C. Baccigalupi, A. J. Banday, and et al. Planck 2013 results. XVI. Cosmological parameters. *ArXiv e-prints*, March 2013.
- B. M. Poggianti, A. von der Linden, G. De Lucia, V. Desai, L. Simard, C. Halliday, A. Aragón-Salamanca, R. Bower, J. Varela, P. Best, D. I. Clowe, J. Dalcanton, P. Jablonka, B. Milvang-

Bibliography

- Jensen, R. Pello, G. Rudnick, R. Saglia, S. D. M. White, and D. Zaritsky. The Evolution of the Star Formation Activity in Galaxies and Its Dependence on Environment. *ApJ*, 642:188–215, May 2006. doi: 10.1086/500666.
- B. M. Poggianti, V. Desai, R. Finn, S. Bamford, G. De Lucia, J. Varela, A. Aragón-Salamanca, C. Halliday, S. Noll, R. Saglia, D. Zaritsky, P. Best, D. Clowe, B. Milvang-Jensen, P. Jablonka, R. Pelló, G. Rudnick, L. Simard, A. von der Linden, and S. White. The Relation between Star Formation, Morphology, and Local Density in High-Redshift Clusters and Groups. *ApJ*, 684: 888–904, September 2008. doi: 10.1086/589936.
- M. Postman, D. Coe, N. Benítez, L. Bradley, T. Broadhurst, M. Donahue, H. Ford, O. Graur, G. Graves, S. Jouvel, A. Koekemoer, D. Lemze, E. Medezinski, A. Molino, L. Moustakas, S. Ogaz, A. Riess, S. Rodney, P. Rosati, K. Umetsu, W. Zheng, A. Zitrin, M. Bartelmann, R. Bouwens, N. Czakon, S. Golwala, O. Host, L. Infante, S. Jha, Y. Jimenez-Teja, D. Kelson, O. Lahav, R. Lazkoz, D. Maoz, C. McCully, P. Melchior, M. Meneghetti, J. Merten, J. Moustakas, M. Nonino, B. Patel, E. Regös, J. Sayers, S. Seitz, and A. Van der Wel. The Cluster Lensing and Supernova Survey with Hubble: An Overview. *ApJS*, 199:25, April 2012. doi: 10.1088/0067-0049/199/2/25.
- R. F. Quadri, R. J. Williams, M. Franx, and H. Hildebrandt. Tracing the Star-formation-Density Relation to $z \sim 2$. *ApJ*, 744:88, January 2012. doi: 10.1088/0004-637X/744/2/88.
- F. Renaud, F. Bornaud, and P.-A. Duc. A parsec-resolution simulation of the Antennae galaxies: formation of star clusters during the merger. *MNRAS*, 446:2038–2054, January 2015. doi: 10.1093/mnras/stu2208.
- P. Rosati, I. Balestra, C. Grillo, A. Mercurio, M. Nonino, A. Biviano, M. Girardi, E. Vanzella, and CLASH-VLT Team. CLASH-VLT: A VIMOS Large Programme to Map the Dark Matter Mass Distribution in Galaxy Clusters and Probe Distant Lensed Galaxies. *The Messenger*, 158: 48–53, December 2014.
- P. Santini. How do galaxies accrete their mass? Quiescent and star-forming massive galaxies at high redshift. *Journal of Physics Conference Series*, 280(1):012007, February 2011. doi: 10.1088/1742-6596/280/1/012007.
- D. J. Schlegel, D. P. Finkbeiner, and M. Davis. Maps of Dust Infrared Emission for Use in Estimation of Reddening and Cosmic Microwave Background Radiation Foregrounds. *ApJ*, 500:525–553, June 1998. doi: 10.1086/305772.
- M. Tanaka, A. Finoguenov, T. Kodama, Y. Koyama, B. Maughan, and F. Nakata. The spectroscopically confirmed huge cosmic structure at $z = 0.55$. *A&A*, 505:L9–L12, October 2009. doi: 10.1051/0004-6361/200912929.
- D. Tody. IRAF in the Nineties. In R. J. Hanisch, R. J. V. Brissenden, and J. Barnes, editors, *Astronomical Data Analysis Software and Systems II*, volume 52 of *Astronomical Society of the Pacific Conference Series*, page 173, January 1993.

- A. Tokovinin and V. Kornilov. Accurate seeing measurements with MASS and DIMM. *MNRAS*, 381:1179–1189, November 2007. doi: 10.1111/j.1365-2966.2007.12307.x.
- R. B. Tully, H. Courtois, Y. Hoffman, and D. Pomarède. The Laniakea supercluster of galaxies. *Nature*, 513:71–73, September 2014. doi: 10.1038/nature13674.
- A. van der Wel. The Dependence of Galaxy Morphology and Structure on Environment and Stellar Mass. *ApJL*, 675:L13–L16, March 2008. doi: 10.1086/529432.
- B. Vollmer, M. Soida, K. Otmianowska-Mazur, J. D. P. Kenney, J. H. van Gorkom, and R. Beck. A dynamical model for the heavily ram pressure stripped Virgo spiral galaxy NGC 4522. *A&A*, 453:883–893, July 2006. doi: 10.1051/0004-6361:20064954.
- A. von der Linden, P. N. Best, G. Kauffmann, and S. D. M. White. How special are brightest group and cluster galaxies? *MNRAS*, 379:867–893, August 2007. doi: 10.1111/j.1365-2966.2007.11940.x.
- B. Vulcani, B. M. Poggianti, R. A. Finn, G. Rudnick, V. Desai, and S. Bamford. Comparing the Relation Between Star Formation and Galaxy Mass in Different Environments. *ApJL*, 710: L1–L6, February 2010. doi: 10.1088/2041-8205/710/1/L1.
- C. R. Wagner, M. Brodwin, G. F. Snyder, A. H. Gonzalez, S. A. Stanford, S. Alberts, A. Pope, D. Stern, G. R. Zeimann, R.-R. Chary, A. Dey, P. R. M. Eisenhardt, C. L. Mancone, and J. Moustakas. Star Formation in High-redshift Cluster Ellipticals. *ApJ*, 800:107, February 2015. doi: 10.1088/0004-637X/800/2/107.
- R. H. Wechsler, J. S. Bullock, J. R. Primack, A. V. Kravtsov, and A. Dekel. Concentrations of Dark Halos from Their Assembly Histories. *ApJ*, 568:52–70, March 2002. doi: 10.1086/338765.
- K. E. Whitaker, P. G. van Dokkum, G. Brammer, and M. Franx. The Star Formation Mass Sequence Out to $z = 2.5$. *ApJL*, 754:L29, August 2012. doi: 10.1088/2041-8205/754/2/L29.
- S. D. M. White, D. I. Clowe, L. Simard, G. Rudnick, G. De Lucia, A. Aragón-Salamanca, R. Bender, P. Best, M. Bremer, S. Charlot, J. Dalcanton, M. Dantel, V. Desai, B. Fort, C. Halliday, P. Jablonka, G. Kauffmann, Y. Mellier, B. Milvang-Jensen, R. Pelló, B. Poggianti, S. Poirier, H. Rottgering, R. Saglia, P. Schneider, and D. Zaritsky. EDisCS - the ESO distant cluster survey. Sample definition and optical photometry. *A&A*, 444:365–379, December 2005. doi: 10.1051/0004-6361:20042068.
- D. B. Wijesinghe, A. M. Hopkins, S. Brough, E. N. Taylor, P. Norberg, A. Bauer, M. J. I. Brown, E. Cameron, C. J. Conselice, S. Croom, S. Driver, M. W. Grootes, D. H. Jones, L. Kelvin, J. Loveday, K. A. Pimbblet, C. C. Popescu, M. Prescott, R. Sharp, I. Baldry, E. M. Sadler, J. Liske, A. S. G. Robotham, S. Bamford, J. Bland-Hawthorn, M. Gunawardhana, M. Meyer, H. Parkinson, M. J. Drinkwater, J. Peacock, and R. Tuffs. Galaxy And Mass Assembly (GAMA): galaxy environments and star formation rate variations. *MNRAS*, 423:3679–3691, July 2012. doi: 10.1111/j.1365-2966.2012.21164.x.

Bibliography

- D. J. Wilman, S. Zibetti, and T. Budavári. A multiscale approach to environment and its influence on the colour distribution of galaxies. *MNRAS*, 406:1701–1720, August 2010. doi: 10.1111/j.1365-2966.2010.16845.x.
- C. Wolf, A. Aragón-Salamanca, M. Balogh, M. Barden, E. F. Bell, M. E. Gray, C. Y. Peng, D. Bacon, F. D. Barazza, A. Böhm, J. A. R. Caldwell, A. Gallazzi, B. Häußler, C. Heymans, K. Jahnke, S. Jogee, E. van Kampen, K. Lane, D. H. McIntosh, K. Meisenheimer, C. Papovich, S. F. Sánchez, A. Taylor, L. Wisotzki, and X. Zheng. The STAGES view of red spirals and dusty red galaxies: mass-dependent quenching of star formation in cluster infall. *MNRAS*, 393: 1302–1323, March 2009. doi: 10.1111/j.1365-2966.2008.14204.x.

Acronyms

ACS	Advanced Camera for Surveys
ADU	analog-to-digital units
AGN	active galactic nucleus
BCG	brightest cluster galaxy
BPZ	Bayesian Photometric Redshifts
CCD	charge-coupled device
CFHT	Canada-France-Hawaii Telescope
CLASH	Cluster Lensing And Supernova survey with Hubble
CW	Cosmic Web
ETG	early-type galaxy
EDisCS	ESO Distant Cluster Survey
ESA	European Space Agency
ESO	European Southern Observatory
EAZY	Easy and accurate z_{phot} from Yale
EW	equivalent width
FORS2	FOcal Reducer and low dispersion Spectrograph 2
FoV	field of view
FWHM	Full Width at Half Maximum
GMOS	Gemini Multi-Object Spectrograph
Gyr	10^9 years
HST	Hubble Space Telescope

Chapter 6. Acronyms

ICBS	IMACS Cluster Building Survey
IMACS	Inamori-Magellan Areal Camera & Spectrograph
IMF	initial mass function
IR	infrared
IRAF	image reduction and analysis facility
Jy	Jansky
LCDCS	Las Campanas Distant Cluster Survey
LDP	low dispersion prism
LSS	large scale structures
MACS	Massive Cluster Survey
MAD	median absolute deviation
NMAD	normalized median absolute deviation
MC	Monte-Carlo
Mpc	megaparsec
NTT	New Technology Telescope
NIR	near-infrared
NUV	near ultra-violet
OB	observation block
photo-z	photometric redshifts
PSF	point spread function
SED	spectral energy distribution
SDSS	Sloan Digital Sky Survey
SF	star formation
SFH	star formation history
SFR	star formation rate
SNR	signal-to-noise ratio
SOFI	Son OF Infrared Spectrometer And Array Camera

SPS	stellar population synthesis
TPZ	Trees for Photo-Z
VIMOS	VIisible MultiObject Spectrograph
VLT	Very Large Telescope
VMMPS	VIMOS Mask Preparation Software
yr	year
z	redshift

François Rérat
Av. Charles-Dickens 10
1006 Lausanne
Cell phone : +41 76 4799493
E-mail : francois.rerat@epfl.ch

Date of Birth : 18.11.87
Nationality : Swiss and French

Curriculum Vitae

Education

- 2011 – 2015 **PhD of Science in Astrophysics**
Swiss Federal Institute of Technology Lausanne (Ecole Polytechnique
Fédérale de Lausanne , EPFL), Laboratoire d'Astrophysique (LASTRO)
Analysis of the properties of galaxies surrounding galaxy clusters.
Won several competitions to obtain observations with some of the most powerful
telescopes in the world (Very Large Telescope, Canada-France-Hawaii Telescope).
Very broad range of data analysis techniques in photometry and spectroscopy.
Discovery of a new exoplanet while working in the La Silla Observatory in Chile.
- 2009 - 2011 **Master of Science in Physics**
EPFL, Average : 5.27 / 6
Master thesis : creation of a software to predict the distance and luminosity distributions
of the galaxies in the Universe (5.5 / 6).
- 2006 - 2009 **Bachelor of Science in Physics**
EPFL
- 2003 - 2006 **Maturity: option physics and applied mathematics**
Gymnase français, Bienne
Average over the last year : 5.56 / 6
Excellence award

Languages

- French : Native language
- English : Fluent (C1)
TOEFL (iBT, 106 / 120)
- German : Average knowledge (B1)

Student Societies Experiences

- 2009 - 2014 Dossier-K, Lausanne
Acting in several plays, treasurer
- 2008 - 2009 AIESEC, Lausanne
Coaching students looking for internships in foreign countries.

Computer skills

C++, Python, Matlab, Latex, MS office

Other Activities and Hobbies

Squash, badminton, skiing , music, piano, theater, travel